Radboud Repository

Radboud University Nijmegen

PDF hosted at the Radboud Repository of the Radboud University Nijmegen

The following full text is a publisher's version.

For additional information about this publication click this link.
http://hdl.handle.net/2066/113969

Please be advised that this information was generated on 2017-12-06 and may be subject to change.

3836

CRYSTAL GROWTH AND CHARACTERIZATION OF BISMUTH GERMANATE (BGO)

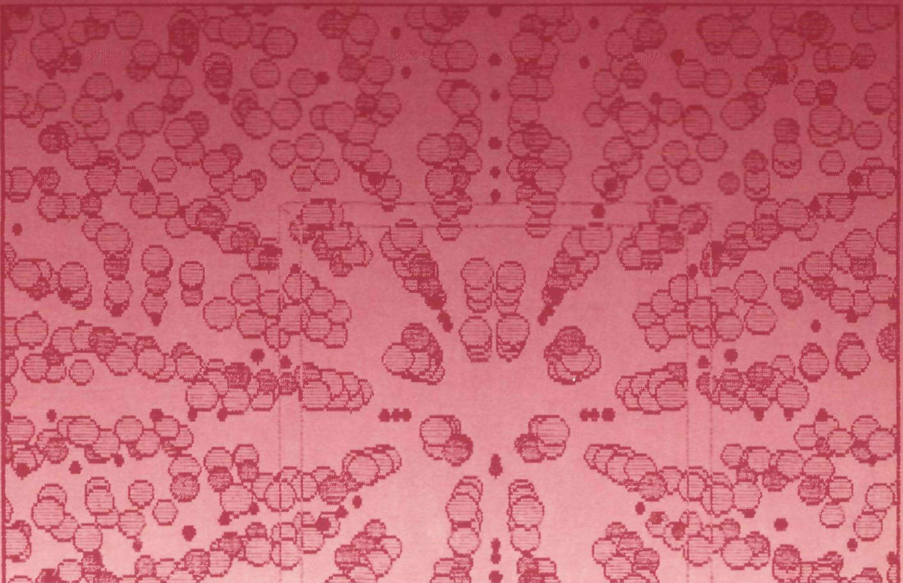

F.M. SMET

CRYSTAL GROWTH AND CHARACTERIZATION OF BISMUTH GERMANATE (BGO)

ISBN 90-9002981-8

CRYSTAL GROWTH AND CHARACTERIZATION OF BISMUTH GERMANATE (BGO)

een wetenschappelijke proeve op het gebied van
de natuurwetenschappen

PROEFSCHRIFT
ter verkrijging van de graad van doctor
aan de Katholieke Universiteit van Nijmegen,
volgens besluit van het college van decanen
in het openbaar te verdedigen
op woensdag 13 september 1989,
des namiddags om 1.30 uur precies

door

Franciscus Maria Smet

geboren op 1 augustus 1950 te Vlissingen

1989
DRUK: SSN NIJMEGEN

Promotores : Prof. Dr. P. Bennema
Prof. Dr. R.T. Van de Walle

Co-referent : Dr. W.J.P. van Enckevort

aan mijn moeder

Graag wil ik op deze plaats iedereen bedanken die aan de totstandkoming van dit proefschrift heeft bijgedragen.

De medewerkers van de afdeling Vaste Stof Chemie ben ik dankbaar voor hun inspirerende samenwerking. Zij vormden mijn wetenschappelijke thuisbasis.

Op de afdeling Experimentele Hoge Energie Fysica kreeg het technologische gedeelte van het onderzoek gestalte.
Ik ben alle medewerkers erkentelijk voor hun steun en interesse in de afgelopen jaren. In het bijzonder de leden van de BGO-groep wiens enthousiasme of pessimisme bij de geboorte van ieder nieuw kristal ik niet had willen missen en wiens technische assistentie onmisbaar was.

Tenslotte wil ik speciaal diegenen bedanken die in mijn directe werkomgeving met hun kamaraadschap en morele steun dit werk mede hebben mogelijk gemaakt.

The investigations in this thesis were made possible by the financial support of the "Stichting voor de Technische Wetenschappen (STW)".

Contents

1. Introduction 9

2. High temperature in-situ microscopy

2.1 In-situ microscopy of the growth of Bismuth Germanate crystals from high temperature melts 15

2.2 In-situ microscopic investigations of crystal growth processes in the system Bi_2O_3-GeO_2 27

3. The growth of large single crystals

3.1 On the distribution of point defects in large sized Bridgman grown Bismuth Germanate crystals 53

3.2 A characterization study of large sized Czochralski grown Bismuth Germanate crystals 65

4. Optical characterization of dislocations

4.1 Optical characterization of crystal dislocations: The case of Bismuth Germanate 78

4.2 Dislocation etching of rough crystal faces 101

5. Crystallographic structure and crystal habit: The morphological theory applied to BGO

5.1 Crystal morphology of BGO ($Bi_4Ge_3O_{12}$) 110

Samenvatting 135

Curriculum vitae 139

CHAPTER 1

INTRODUCTION

Crystals have fascinated mankind since early days. Among the many shapes that nature produces, the mineral crystals with their geometrical perfection surely are unique in expressing the ordered nature of matter. For centuries this has given them a high symbolic and aesthetical value.

Originating from mineralogy, the development of crystallography has led us via the law of constant angles (Steno, 1669), the law of rational indices (Haüy, 1800), the mathematical formulation of crystal symmetry and the discovery of X-ray diffraction (Laue, 1912) [1] to the concepts of spiral growth and roughening temperature (BCF, 1951 [2]) which are the basis of modern crystal growth science.

Today crystal growth is the subject of research in a number of diverse fields, among which are industrial crystallization, semiconductor physics, opto-electronics, bio-mineralization and process industry [3].

Industrial crystallization comprizes the production of many daily used crystalline species such as salt, soda and fertilizers, but also organic chemicals, by large scale bulk crystallization processes. In these processes nucleation behaviour and crystal habit in relation to the various process parameters are the main points of interest.

In the semiconductor and opto-electronic industries a number of special techniques is in use for the growth of large, highly perfect single crystals, mostly at high temperature. Here the crystal growth processes have to allow for the very specific electronic and optical properties which are required in the production of devices [4]. The Czochralski technique and the Bridgman technique are most widely used in this area.

A separate field in the semiconductor manifacturing is the growth of thin monocrystalline layers by chemical vapor deposition (CVD). These crystal growth processes occur at high temperature and are coupled to chemical reactions.

In biomineralization and in scaling, the crystal habit and its modification by impurities is important.

The most important quantity which can be distinguished in a crystal growth proces is the roughness condition of the interface between crystal and motherphase.

If the interface is rough then growth proceeds by a 'normal' growth mechanism, and is determined mainly by heat transport or transport of matter.

At an (atomically) flat interface a layered growth mechanism is operative. In such a growth process, from the liquid or gasphase, the following steps can usually be discerned: 1) diffusion of a growth unit from the motherphase to the crystal surface; 2) adsorption of the growth unit on the crystal surface; 3) surface diffusion to a step or a kink position; 4) insertion into the kink.

Each of these steps is dependent of a large number of factors which comprise both (fixed) physical properties of the crystal as well as variable conditions such as temperature gradient and concentration. In solution growth, for instance, the first step could involve the hydrodynamics of the motherphase or the desolvation of the growth units.

Steps two, three and four determine the surface kinetics. They do depend -in a discrete manner- on the crystallographical orientation of the growing surface. In principle the layer thickness and the energies of steps on the surface are different for each orientation *hkl*.

The formation of new layers is mostly governed by a spiral growth mechanism. The spirals (and other step sources) are directly related to lattice defects in the crystal such as dislocations. Their distribution over the surface determines the precise local arrangement of the steps. They can be present in various amounts.

Finally, the advancement of the steps on the surface can be hindered or blocked by a preferentially adsorbed impurity. Even at very low concentration in the motherphase this possibility cannot be excluded.

In the presence of a driving force these factors lead to a specific growth rate at each part of the crystal surface. In the resulting morphology the contributions of the different factors are often visible. For this reason morphological studies are the main starting point in the investigation of crystal growth processes.

Differences in the growth mechanism at the surface cause (local) variations in the physical properties of the crystal being grown. From detailled studies with optical or other characterization methods the growth history of a crystal can be reconstructed and the relevant growth factors identified.

This thesis describes an investigation of the growth of bismuth germanium oxide ($Bi_4Ge_3O_{12}$, BGO) crystals. The attention was focussed on the growth process from the melt at

1055 °C. Of prime interest were the growth and the properties of large single crystals in view of their application as a scintillator medium in high energy physics research [5]. This application demands highly perfect and optical transparent crystals.

The main goal of the investigation was to acquire a deeper insight in the fundamental growth processes in the case of BGO. Obviously such knowledge is a prerequisite for the improvement of the Bridgman and Czochralski growth techniques and the optimalization of its parameters.

To this end several studies were undertaken, dedicated to the fundamental growth behaviour, the specific growth conditions during Bridgman growth, and the characterization of large BGO crystals. Some important results are reported in the next chapters.

The examination of the growth at high temperature in a very corrosive melt was feasable through the development of a special observation technique, viz. high temperature in situ microscopy. Chapter 2 describes the direct observation of the nucleation and growth behaviour of BGO with this elegant method. In addition a systematic study on crystal growth phenomena in the whole composition range of the GeO_2-Bi_2O_3 phase diagram is presented.

In chapter 3 the growth of large single crystals is discussed. Morphological experiments (including sphere growth experiments) and characterization of the crystals by U.V. topography, laser light scattering and the Schlieren method indicate that in Bridgman growth the solid-liquid interface is constituted by {112} and $\{\bar{1}\bar{1}\bar{2}\}$ crystallographic facets. It was demonstrated that a difference in optical density and impurity segregation exists between {112} and $\{\bar{1}\bar{1}\bar{2}\}$ growth sectors. In this chapter also the results are discussed of a comparative study of crystals grown by the Bridgman technique and the Czochralski technique.

Chapter 4 comprizes an elaborate study of the most sensitive microscopical techniques and their applicability as characterization methods for BGO crystals. Using stress birefringence microscopy, the Burgers vector of the dislocations occurring in Bridgman grown crystals could be identified as 1.[110] . Dark field microscopy revealed the presence of micro-inclusions and their relationship to grown-in dislocations. In a separate study the detection of dislocation etch pits on rough and flat crystal faces is analysed.

Chapter 5 is devoted to the crystal morphology of BGO. The PBC theory of Hartman and Perdok, extended with the Rijpkema formalism [6] is applied to the crystal structure of BGO. Starting from a careful analysis of the bonds in the crystal and the melt, this theory enables the calculation of the morphological importance (MI) of the crystallographical faces and their critical Ising temperature. The results of the calculations are compared with the experimentally determined crystal morphology of BGO. The absolute roughening temperature of the most important crystal faces is predicted.

References

[1] J.G. Burke, Origins of the Science of Crystals (University of California Press, Berkely, 1966).

[2] W.K. Burton, N. Cabrera and F.C. Frank, Phil. Trans. Roy. Soc. London A243 (1951) 299.

[3] Proceedings of the Eight International Conference on Crystal Growth, York 1986, J. Crystal Growth 79 (1986).

[4] B. Cockayne, J Crystal Growth 42 (1977).

[5] International Workshop on Bismuth Germanate, Princeton, 1982.

[6] J.J.M Rijpkema, H.J.F. Knops, P. Bennema and J.P. van der Eerden, J. Crystal Growth 61 (1983) 295.

CHAPTER 2

HIGH TEMPERATURE IN-SITU MICROSCOPY

Journal of Crystal Growth 82 (1987) 678-688
North-Holland, Amsterdam

IN SITU MICROSCOPY OF THE GROWTH OF BISMUTH GERMANATE CRYSTALS FROM HIGH TEMPERATURE MELTS

W.J.P. VAN ENCKEVORT and F. SMET

Department of Solid State Chemistry, Department of High Energy Physics, Faculty of Science, University of Nijmegen, Toernooiveld, 6525 ED Nijmegen, The Netherlands

Received 31 March 1986, manuscript received in final form 26 January 1987

The growth behaviour of $Bi_4Ge_3O_{12}$ crystals has been studied in situ by direct observation of the growth processes in the high temperature melt using visible light and IR transmission microscopy. The observations have been recorded by a video system. Three forms of $Bi_4Ge_3O_{12}$ were encountered and examined: (i) a stable phase with a cubic structure, growing at 1050 ° C as facetted blocks or dendrites, (ii) a metastable phase with a platelet habit, which grows at an undercooling of about 200 ° C, (iii) glass-like amorphous material, which transforms to the stable or metastable structure at 500 ° C. The structural relationships between the three forms and the melt are discussed on the basis of optical characteristics.

1. Introduction

Recently bismuth germanate ($Bi_4Ge_3O_{12}$) has received much attention as a scintillator crystal for detection of X-rays and gamma radiation in the fields of medical science and high energy physics. At this moment efforts are underway in several industrial and university laboratories to grow large sized single crystals of this compound from the melt. To produce these crystals successfully, a detailed fundamental knowledge of the growth behaviour of the material is of importance.

Recently Tsukamoto et al. [1] developed a technique to observe in situ the growth of crystals from high melting point melts by optical transmission microscopy. By this method they succeeded in observing the time dependent behaviour of surface patterns and a roughening transition for melt-grown diopside crystals at 1600 K.

In the present paper the application of the in situ method as a tool to obtain information on the growth processes in melts with a composition of 40 mol% Bi_2O_3 and 60 mol% GeO_2 is described. By this technique, the crystal growth and phase transformation properties of three different forms of $Bi_4Ge_3O_{12}$ (BGO), namely the stable cubic phase, a metastable orthorhombic phase and an amorphous glass form, were studied. The results are discussed phenomenologically in terms of crystal growth theories.

2. Experimental

2.1. Growth system

The major problem in designing a growth vessel for in-situ observations of crystal growth from BGO melts by optical transmission microscopy, is the fact that liquid BGO attacks almost all materials except the platinum group of metals. Therefore a method very similar to the one described by Tsukamoto et al. [1] was used, where the liquid is suspended in a loop or a coil of Pt–Rh wire. The design of the vessel is given in fig. 1: The body of the vessel, made of brass, is cooled by a water flow. The growth chamber is equipped with two opposite quartz windows to allow for transmission microscopy. The circular top quartz plate is placed excentrically so that in case of contamination by evaporating material, it can simply be rotated to acquire a clean window area. The experiments were carried out in an oxygen atmosphere. Temperature measurement was carried out by placing

0022-0248/87/$03.50 © Elsevier Science Publishers B.V.
(North-Holland Physics Publishing Division)

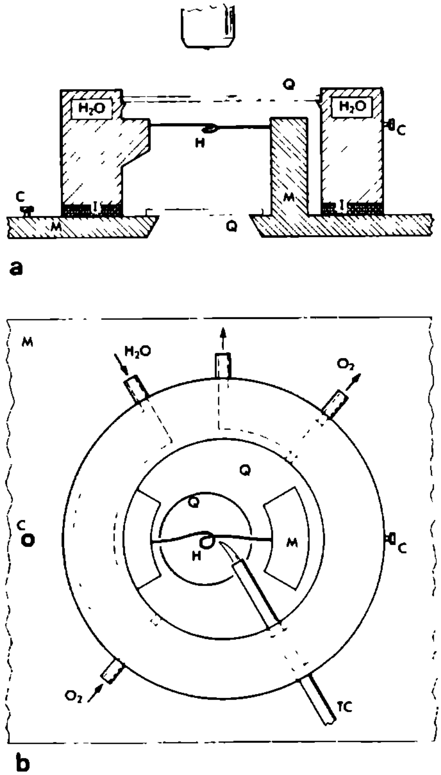

Fig. 1. Schematic representation of chamber for in situ observations of crystal growth processes from high temperature melts: (a) side view; (b) top view M: brass growth chamber; Q: quartz top and bottom windows; I: insulating layer between top and lower part of growth chamber; H: loop of Pt–10% Rh wire; C: contacts for heating current; TC: thermocouple; H_2O: water cooling.

a Pt/Pt–10% Rh thermocouple in contact with the growth cell.

The growth cell itself was made of a loop of Pt–10% Rh wire. A proper design and winding of this wire (0.35 mm in thickness) is essential. Heating of the cell was achieved by passing a current (5–10 A, 3 V) through the wire. To eliminate effects of electrolysis (molten BGO is an ionic conductor), AC current (50 Hz) was used. The temperature stability of the cell was within a few degrees Celsius during a period of 15 min.

Leaching of Rh from the Pt/Rh growth cell and thermocouples, as reported by Whiffin et al. [15] for $Bi_{12}SiO_{20}$ did not influence the experiments. This can be understood from the following: (a) an experimental run takes maximal only 30 min; (b) the growth cell is regularly replaced; (c) only relative temperatures, taking the melting point of $Bi_4Ge_3O_{12}$ as reference, were measured. Further a Pt/Rh thermocouple kept for several hours in molten $Bi_4Ge_3O_{12}$ gave no substantial decrease in temperature read-out.

To eliminate the possibility that some of the phenomena reported in this paper are a result of residual electrolysis, all the experiments were repeated in a conventional heating stage for optical microscopy fitted with a platinum crucible. Observation by reflection microscopy showed an exactly identical optical and crystal growth behaviour as in the above described system for transmission microscopy.

2.2. Optical system and source material

Liquid BGO does not transmit a detectable amount of visible light at or above the melting point of $Bi_4Ge_3O_{12}$ (1050 °C). On the other hand, infrared light is transmitted well. A strongly undercooled melt of BGO at about 850–900 °C also transmits red light. Therefore to carry out the in situ observations by means of optical transmission microscopy, use was made of an IR sensitive video camera. To minimize the disturbing effects of the visible – red – heat radiation, the microscope was fitted with a high intensity light source. In addition a cut-off filter, which stops radiation with $\lambda < 780$ nm, and a neutral absorption filter were placed in front of the video camera. In general only bright field illumination was used.

The growth process of the crystals is recorded on video tape by means of the video camera, which is connected to an analog contrast amplifier in order to increase the image contrast to a large extent.

As source material small, inclusion free parts of good quality BGO crystals grown by the Bridgman method were used.

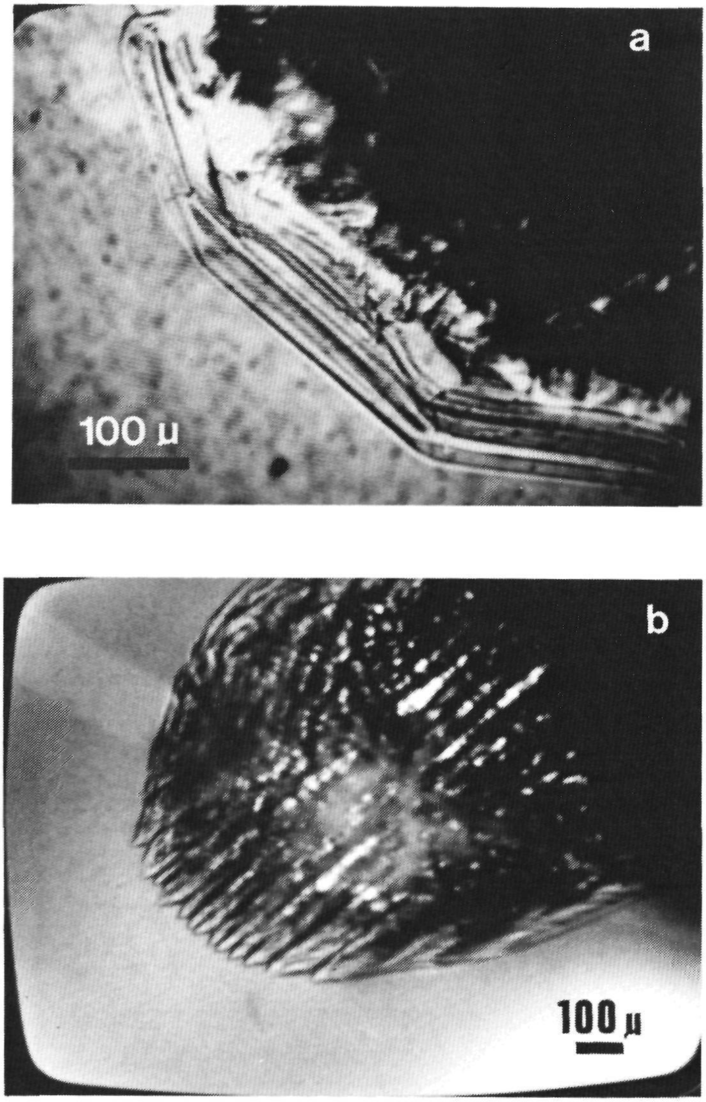

Fig. 2. Crystals of eulytine type $Bi_4(GeO_4)_3$ growing in a slightly undercooled melt at 1050 °C: (a) slow growth: facetted crystals; (b) fast growth: cellular structure.

3. Observations and discussion

3.1. Stable phase

To allow for observation of the crystal growth process in the melt, an undercooled melt was prepared by first melting a piece of crystalline BGO at 1060 ° C, and subsequently cooling down the liquid a few degrees. In many cases the melt tended to undercool strongly. To initiate crystal growth in these cases a small seed crystal or a cold nucleation point was introduced in the liquid.

In general, the growing crystals were bounded by planar facets. In the case of slow growth and in absence of large temperature gradients, well shaped facetted crystals (fig. 2a) were formed. For high growth rates, cellular – but still facetted – and dendritic growth were observed (fig. 2b). Irradiation of the crystals with UV light at room temperature gave a greenish-white luminescence. Powder X-ray diffraction established the structure to be eulytine type $Bi_4(GeO_4)_3$ [2]. This is the stable phase of BGO (BGO_s) as reported by Speranskaya and Arshakuni [3].

An intriguing observation was that the growing or dissolving BGO crystals were colourless (maybe slightly yellowish) and transparent at 1050 ° C, whereas the melt was opaque for visible light and transparent only for IR radiation.

3.2. Metastable phase

Cooling down of thoroughly molten BGO_s from a temperature slightly above its melting point often resulted in the formation of a highly undercooled melt that crystallizes at 850–900 ° C. The crystals formed in this way had a platelet-like habitus (fig. 3), completely different from the crystals growing in a non-undercooled melt. Often the platelets nucleated at the platinum–melt interface; in some cases also spontaneous nucleation in the melt was observed. No solid state transition was observed during cooling down of the crystal plates to 20 ° C. Irradiation by UV light at room temperature gave no visible luminescence. X-ray powder diffraction analysis showed that the lattice parameters and systematic extinctions of the reflections were identical to the compound Bi_2GeO_5

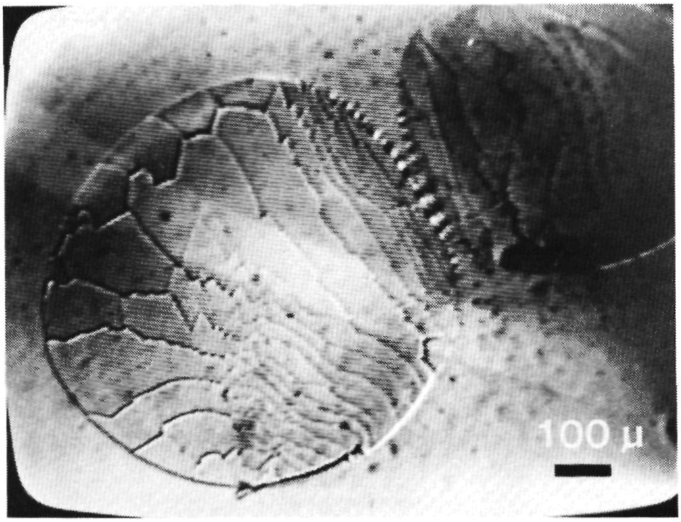

Fig. 3. Platelet shaped crystals of orthorhombic Bi_2GeO_5 crystals growing in a highly undercooled melt at ± 900 ° C.

reported by Aurivillius et al [4] Tananaev et al [5] reported Bi_2GeO_5 also to be the metastable phase in the system Bi_2O_3/30–40 mol% GeO_2

To prevent nucleation of the stable phase in the undercooled melt prior to the formation of metastable BGO (BGO_{ms}), it is essential that all three-dimensional nuclei of BGO_s are dissolved This was achieved by heating the melt for a short period at about 10 to 30 ° C above the melting point of BGO_s Such an overheating of the melt might also introduce a structural change at molecular scale, enhancing the formation of the metastable phase as discussed by Tananaev and coworkers [5,14] for $Bi_{12}GeO_{20}$ An increased cooling rate (even 50 ° C/s^{1}) did not cause a premature crystallization of BGO_s in the traject 1050–850 ° C

Reheating of the crystallized metastable phase gave complete melting at ± 850 ° C From the in situ observations it is apparent that the melt or growth trajectory of BGO_{ms} is not very large Small changes in temperature led to a complete solidification or melting Continued heating of the molten BGO_{ms} combined with the introduction of a small seed of BGO_s or a cold point in the liquid resulted in a sudden formation of BGO_s, which again melted at ±1050 ° C If no external influence was exerted the melt did not recrystallize upon heating

If a seed of BGO_s or a cold point was introduced into a BGO_{ms} phase, which was heated slightly below its melting point of 850 ° C, the BGO_{ms} was quickly transformed into BGO_s via a solid state phase transition

During growth or melting of BGO_s at 1050 ° C the liquid was only transparent for IR light, whereas the solid was transparent for visible and IR light Upon undercooling to 850 ° C, the liquid became also transparent for red light The crystallizing BGO_{ms} at this temperature showed a similar red colour as the melt Only a little difference in optical behaviour (BGO_{ms} was somewhat more transparent than its melt) could be detected by visual inspection During the cooling down of the metastable phase to room temperature, the crystals became more transparent for visible light and got a pale brown reddish colour

Aside from the in-situ experiments, BGO_{ms} was also grown in larger furnaces Starting from high purity (5N–6N) 40 mol% Bi_2O_3 and 60 mol% GeO_2 source materials a few cubic centimeters of BGO_{ms} crystal plates were obtained The crystals were transparent with a pale brown tint The crystallization temperature was about 850 ° C, the melting point about 900 ° C For 50% Bi_2O_3 and 50% GeO_2, the exact stoichiometric composition of the metastable phase, a sharp melting point at 931° C was found

In cases of not too high growth rates (< 100 μm/s), the BGO_{ms} crystals grew as thin circular platelets (fig 3) The thickness was only a few microns A platelet habit is in agreement with the unit cell dimensions of BGO_{ms} [4] Application of the Donnay-Harker law [6], which relates crystal shape to lattice properties, shows that structures with one very long unit cell axis (for BGO_{ms}, $a = 1\ 56$ nm) compared to the other ones ($b =$ 0 5492 nm, $c = 0\ 5383$ nm) generally give planar shaped crystals, with their longest axis normal to the plate surface Verification by X-ray diffraction confirmed that the platelet top and bottom surfaces indeed are (100) faces The side faces of the platelet-like crystals were not facetted, regardless of growth rate This means that these faces grow above the roughening point [7] In many cases the non-facetted side faces showed a wavy pattern, which oscillates during growth

When growth proceeded fast (> 100 μm/s), the BGO_{ms} crystals had a needle-like shape (length/width ≈ 3–10)

In cases when one or only a very few crystals were growing in the cell, the platelets floated on the melt The plate surface exposed to the oxygen atmosphere showed a large number of high (non-moving) macrosteps, introduced by instabilities of the side faces during growth The opposite (planar crystal–melt) interface, however, was very smooth as far as could be judged by simple bright field microscopy Thickness growth of the crystal plates was extremely difficult In many cases plane-parallel crystal sheets were formed due to nucleation at defects on the crystal surfaces, leading to the formation of layered polycrystalline material In other cases macrosteps advancing over the plate surfaces could be observed as shown in fig 4

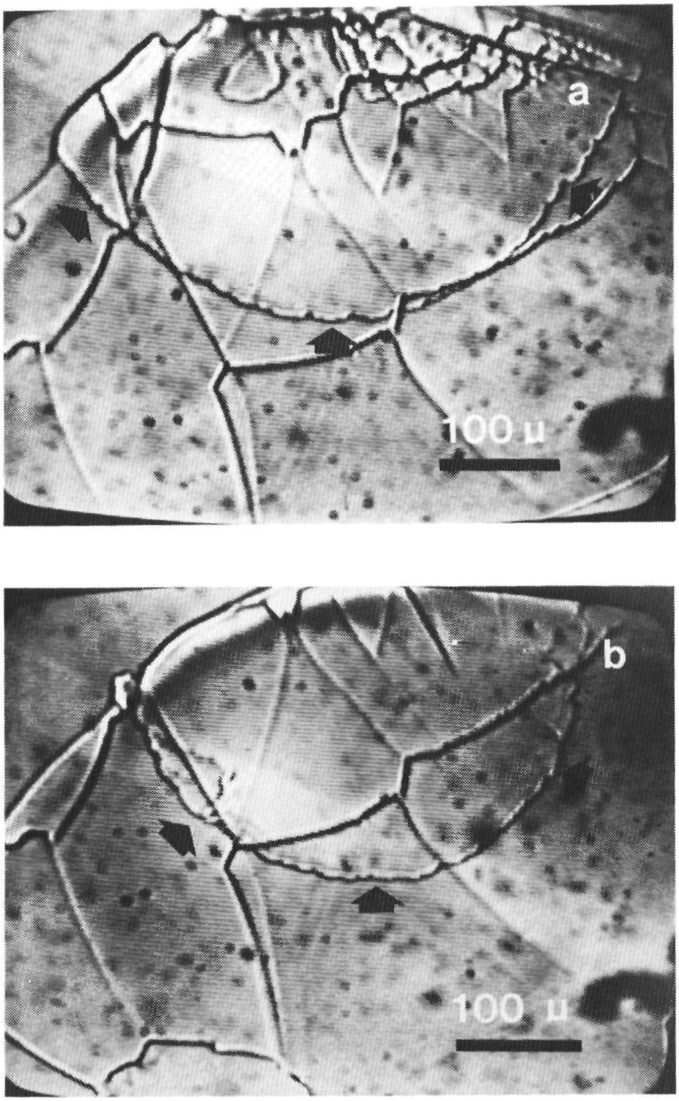

Fig. 4. Macrostep propagating over the solid–melt interface of a growing BGO_{ms} platelet. The step is indicated by arrows. The other (non-moving) steps are at the opposite crystal–oxygen interface. Time interval between (a) and (b): 2s.

3.3. Amorphous state

By quickly cooling down (±50 °C/s) of small amounts of undercooled BGO melt from 850 °C to room temperature a glass-like substance was formed. X-ray powder diffraction proved the material to be amorphous. UV irradiation of the glass-like compound gave no visible luminescence at room temperature. At liquid N_2 temperature an orange luminescence colour was found. A similar orange fluorescence, only occurring at low temperatures, was also reported for Bi_2GeO_5 and $Bi_{12}GeO_{20}$ [8].

The colour of the vitreous BGO at the temperature of formation (transparent red) did not differ from the melt. At room temperature the material was transparent, i.e. pale brown red. For all temperatures only a slight difference in colour between the metastable phase and the glass state was observed by visual inspection.

Heating of the glass led to a devitrification at about 400 to 500 °C, a process which proceeded slowly at the lower end of the temperature range and abruptly at higher temperatures. The crystals formed in this manner often showed a platelet, block or dendritic shape (fig. 5). The recrystallization process could easily be followed by the in situ system. After recrystallization, the orange red coloured crystals melted at ± 900 °C, so the divitrification product is the metastable phase of BGO.

From the present in situ study it can be concluded that Bi_2O_3–60% GeO_2 may occur in four states: liquid, BGO_s, BGO_{ms} and glass. The observed interstate transitions and some optical properties in dependence on state and temperature are summarized schematically in fig. 6.

4. Structural relationships between the three types of BGO and the melt

4.1. Nucleation rate

The difference in Gibbs free energy between an undercooled melt and solid, ΔG_{l-s}, is equivalent to $\Delta T \Delta H_m / T_m$ [9], where ΔT is the undercooling, T_m the temperature of melting and ΔH_m the molar heat of melting. For a melt which is undercooled

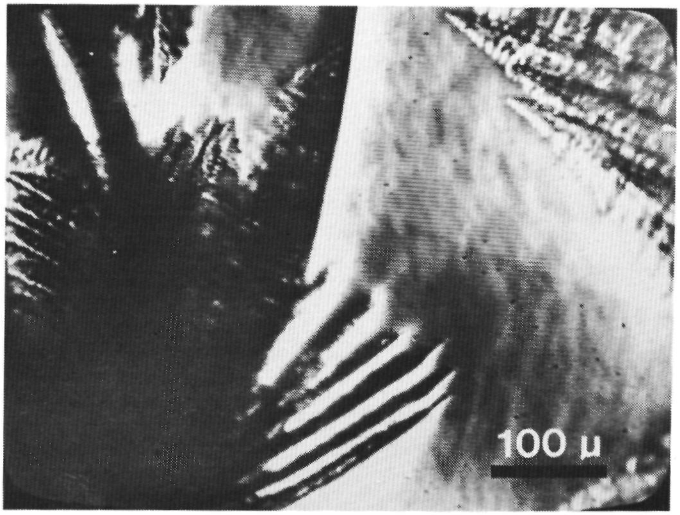

Fig. 5. Dendritic growth of BGO_{ms} crystals from the glass state of BGO. T ± 450 °C.

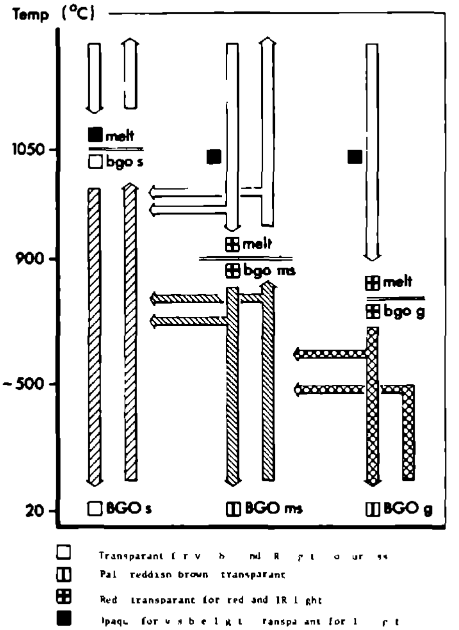
Temp (°C)
1050
900
~500
20
melt
bgo s
melt
bgo ms
melt
bgo g
BGO s
BGO ms
BGO g
Transparant for visible and IR light colourless
Pale reddish brown transparant
Red transparant for red and IR light
Opaque for visible light transparant for IR light

Fig 6 Observed mutual transitions between four possible states (stable metastable amorphous liquid) at the composition 40 mol% Bi_2O_3–60 mol% GeO_2

200°C with respect to the crystallization temperature of BGO_s, $(\Delta G_{l-s})_{BGO,s}$ is by far larger than $(\Delta G_{l-s})_{BGO,ms}$, because $\Delta T_s \gg \Delta T_{ms}$ and $\Delta H_{m,s} > \Delta H_{m\,ms}$ [3,5] In spite of this it is the metastable phase which preferentially crystallizes from such a melt BGO_{ms} is formed at only a few to a few tens degrees below its melting point of about 900°C The preferential crystallization of BGO_{ms} is not a result of a difference in activation energy for the growth process itself introduction of a small seed BGO_s leads to a vigorous growth of BGO_s in the undercooled melt The only explanation that can be given is that the initial nucleation of BGO_s is by far more difficult than for BGO_{ms} In other words, the formation rate of nuclei, J, is much higher for BGO_{ms} than for BGO_s This also holds for the preferential crystallization of BGO_{ms} from the glass state at 400–500°C

In the present case only three-dimensional homogeneous nucleation will be considered Further, the approximation is introduced that the initial three-dimensional nuclei are spherical and the surface free energy of the crystal–melt interface, σ, is isotropic In this case the rate of nucleation, J, is given by

$$J = N_0 V \exp(-\Delta G^*/kT), \qquad (1)$$

where N_0 is the number of sites for stable nuclei, V is the rate at which atoms are added to the nucleus and ΔG^* the free enthalphy of the critical nucleus [10,11] Since BGO_s and BGO_{ms} grow from the same liquid, N_0 and V do not differ too much for both cases Further, the factor in front of the exponential term is of limited importance for the ultimate value of J [9] This means that the difference in nucleation rate of BGO_s and BGO_{ms} must be attributed to the exponential term $\Delta G^*/kT$, so that $\Delta G^*_{ms} < \Delta G^*_s$ The free enthalphy for the critical nucleus, ΔG^*, is given by

$$\Delta G^* = \frac{16\pi\sigma^3 v^2 T_m^2}{3\,\Delta T^2 \Delta H_m^2}, \qquad (2)$$

where v is the molar volume of the growth units in the crystal From this it follows

$$\frac{\sigma_{ms}}{\sigma_s} = \left[\left(\frac{\Delta T_{ms}}{T_{m\,ms}}\right)^2 \left(\frac{T_{m\,s}}{\Delta T_s}\right)^2 \left(\frac{\Delta H_{m\,ms}}{v_{ms}}\right)^2 \times \left(\frac{v_s}{\Delta H_{m\,s}}\right)^2 \left(\frac{\Delta G^*_{ms}}{\Delta G^*_s}\right)\right]^{1/3}$$

For a given volume of melt the heat of crystallization of BGO_{ms} is less than the heat of crystallization of BGO_s This can be inferred from DTA measurements [3] and from the fact that upon crystallization of BGO_s from the melt an incandescence effect was observed in contrast to BGO_{ms} [5] This means that $\Delta H_{ms}/v_{ms} < \Delta H_s/v_s$ Further $\Delta G^*_{ms} < \Delta G^*_s$ and $\Delta T_{ms} \ll \Delta T_s$, thus $\sigma_{ms} < \sigma_s$ In other words, the wetting of the melt is better for the metastable phase This indicates that the melt (and also the glass state) has a stronger structural similarity with BGO_{ms} than with BGO_s, because the melt (glass) "fits" better with the surface of BGO_{ms}

In the case of heterogenous nucleation in ΔG^*, extra surface energy terms for the melt–substrate and solid–substrate interfaces are included To verify the influence of these factors the experiments were repeated in the presence of foreign solid materials like Al_2O_3 or Fe_2O_3, or carried out in a Al_2O_3 growth cell Aside from effects resulting from partial dissolution of the foreign materials in the melt, no essential differences were observed, the influence of additional surface energy terms appears to be not relevant in the present case

4 2 Some optical and structural properties

From fig 6 it is clear that for transmission of light the red colour of BGO_{ms} and BGO_{glass} close to their melting points is similar to the colour of the melt On the other hand, BGO_s remains colourless transparent up to its melting point This suggests an equivalence in environment of the Bi^{3+} ions in BGO_{ms}, BGO_{glass} and the melt, whereas the configuration around Bi^{3+} in BGO_s appears to be completely different from the melt

The glass state can be considered as a frozen melt, leaving the short range order intact Thus it is to be expected that the structure of BGO_{glass} is similar to the melt Therefore in relating structural properties of BGO_s and BGO_{ms} with the melt, we shall also relate their properties with BGO_{glass}, which can be handled at room or lower temperatures

Upon UV irradiation BGO_s gives a strong, white luminescence BGO_{ms} and BGO_{glass} do not fluoresce at room temperature, but only at liquid N_2 temperature, giving an orange colour, in the same manner as reported for $Bi_{12}GeO_{20}$ [8] The pale brown colour of BGO_{glass} and BGO_{ms} at room temperature (red at high temperatures) and their orange luminescence indicate a lower excitation and emission energy than for the transparent and white luminescent BGO_s In other words, the energy difference between the $^1S_0$ and the $^3P_0$ or $^3P_1$ states of the Bi atoms is smaller for BGO_{ms} and BGO_{glass} than for BGO_s [12] This means that for the glass and metastable states the covalence of the Bi–O bonds is stronger than for the stable phase [12] It is very probable that in the glass, and thus in the melt, covalent Bi–O complexes occur in a similar manner as for $(Bi_2O_2)^{2+}$ in BGO_{ms} [4] In the stable phase only the (completely different) Bi^{3+}–GeO_4^{4-} interaction with a weak covalent character occurs

As a second test, IR spectra were recorded from the three solid state phases of BGO, using the KBr pellet technique The results are presented in fig 7 It is obvious that, aside from a rounding off of the features due to disorder in the glass, the spectra of BGO_{glass} and BGO_{ms} are quite similar The spectrum of BGO_s is rather different In the spectra of the metastable and glass phase a peak at 500–550 cm^{-1} can be seen, which is probably due to Ge–O–Ge bonds [13] In the spectrum of BGO_s this peak does not occur The occurrence of Ge–O–Ge bonds, linking together GeO_4^{2-} tetraeders is a well known phenomenon in germanate or silicate glasses In the crystal structure of BGO_{ms} Ge–O–Ge bonds play a major role, in BGO_s they do not occur

As shown by Tananaev and coworkers [5,14], molten $Bi_{12}GeO_{20}$ occurs in three states with different molecular structures (A) a low temperature state from which the stable solid phase crystallizes, (B) an intermediate temperature state, from which the metastable δ^* phase is formed, (C) a high temperature form Earlier work by the same group [16] gives evidence that a structural change of the liquid state also exists for molten $Bi_4Ge_3O_{12}$ As can be deduced from their logarithmic plots of viscosity versus reciprocal temperature, this transition occurs at about 10 °C above the melting point of BGO_s During the present experiments no marked effects of such a liquid–liquid transition were observed This is probably due to the inhomogeneous temperature distribution in the growth cell if the last nucleus of BGO_s has been molten, the temperature at the periphery of the cell is well above the 10 °C superheating zone Therefore in most experiments the melt has been overheated more than 10 °C, so that the metastable and glass phase are preferentially formed In situ experiments carried out in the system 10–20% GeO_2/80–90% Bi_2O_3, however, show indeed optical effects resulting from different kinds of liquids [17]

From the above it can be concluded that the

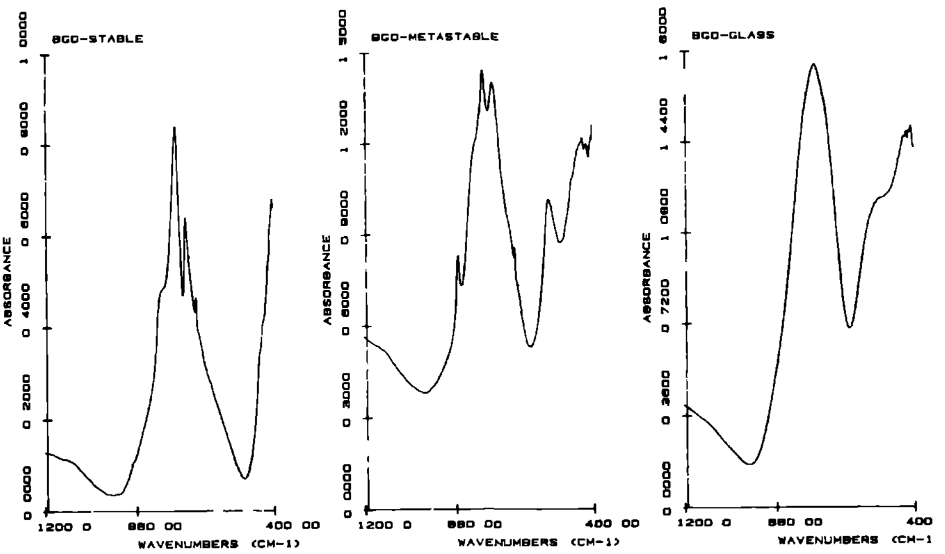

Fig 7 Infrared spectra of BGO_s BGO_{ms} and BGO_{glass} recorded by means of a Fourier transform infrared spectrofotometer using the KBr pellet method

molecular structures of BGO_{ms} and BGO_{glass}, and thus the melt, are very similar but are both different from BGO_s This explains the better wetting of the melt to BGO_{ms} as compared to BGO_s, deduced from nucleation considerations in the previous section A similar kind of structural relationship between melt and solid Bi_2O_3–GeO_2 compounds was suggested by Zhereb et al [14] on the basis of DTA measurements in the region up to 40% GeO_2

5. Conclusions

High temperature in situ transmission microscopy is a relatively simple but powerful method to obtain direct information on the complex crystallization behaviour of high temperature refractory oxide materials from the melt In the present work the formation is described of three types of solid, namely a crystalline stable and metastable state as well as a glass state, all from a melt consisting of 40 mol% Bi_2O_3 and 60 mol% GeO_2 A complicated scheme of allowed mutual transitions between the three phases and the melt and their dependence on temperature and treatment was constructed from numerous in situ observations

The preferential formation of the metastable phase in a melt, highly undercooled with respect to the stable phase, was interpreted in terms of a difference in wetting of the melt with the two crystalline phases The better wetting of the metastable phase with its melt is explained on the basis of a structural equivalence This was confirmed by a resemblance in optical properties between the glass state and the metastable phase, the stable phase showed a completely different optical behaviour

Acknowledgements

The authors are indebted to Prof Dr P Bennema, Prof Dr R T Van de Walle and Drs M

Raaymakers for their interest in the present work They are grateful to F Derksen for the construction of the growth vessel and to Drukker International B V for the use of the Fourier transform infrared spectrofotometer. Finally, they wish to acknowledge the financial support from the Foundation for Technical Sciences (STW)

References

[1] K Tsukamoto, T Abe and I Sunagawa, J Crystal Growth 63 (1983) 215

[2] A Durif and M Averbuch-Pouchot, Compt Rend (Paris) 295 (1982) 555

[3] E I Speranskaya and A A Arshakuni, Russ, J Inorg Chem 9 (1964) 226

[4] B Aurivillius C I Lindblom and P Sténson, Acta Chem Scand 18 (1964) 6

[5] I V Tananaev, V M Skorikov, Y F Kargin and V P Zhereb, Izv Akad Nauk SSSR, Neorg Mater 14 (1978) 2024

[6] J D H Donnay and D Harker, Am Mineralogist 22 (1937) 446

[7] H J Human, J P van der Eerden, L A M J Jetten and J G M Odekerken, J Crystal Growth 51 (1981) 589

[8] G Corsmit, M A van Driel, R J Elsenaar, W van de Guchte, A M Hoogeboom and J C Sens, J Crystal Growth 75 (1986) 551

[9] K A Jackson, in Crystal Growth A Tutorial Approach, Eds W Bardsley, D T J Hurle and J B Mullin (North-Holland, Amsterdam, 1979) p 139

[10] J C Brice, The Growth of Crystals from the Melt, Series of Monographs on Selected Topics in Solid State Physics, Ed E P Wohlfarth (North-Holland, Amsterdam, (1965)

[11] S Toschev, in Crystal Growth An Introduction, Ed P Hartman (North-Holland, Amsterdam, 1973) p 1

[12] G Boulon, B Moine and J C Bourcet, Phys Rev B22 (1980) 1163

[13] L N Demianets, A N Lobachev and G A Emelchenko, in Crystals Growth, Properties and Applications, Vol 4, Ed H C Freyhardt (Springer, Berlin, 1980) pp 130–134

[14] V P Zhereb, Yu F Kargin and V M Skorikov, Izv Akad Nauk SSSR, Neorg Mater 14 (1978) 2029

[15] P A C Whiffin, T M Bruton and J C Brice, J Crystal Growth 32 (1976) 205

[16] Yu F Kargin, V P Zhereb, V M Skorikov, A V Kosov, V A Kutvitskii and E I Nuriev, Russ J Inorg Mater 13 (1977) 114

[17] F Smet and W J P van Enckevort, work in progress

IN SITU MICROSCOPIC INVESTIGATIONS OF CRYSTAL GROWTH PROCESSES IN THE SYSTEM Bi_2O_3-GeO_2

F.SMET and W.J.P. VAN ENCKEVORT*

Dept. of Solid State Chemistry, Dept. of High Energy Physics,
Faculty of Science, University of Nijmegen
Toernooiveld, 6525 ED, Nijmegen
The Netherlands

Abstract:

The crystal growth processes occurring in the system Bi_2O_3-GeO_2 *were investigated systematically by in situ high temperature microscopy. Nucleation, growth and dissolution of stable and metastable phases at temperatures between 700 and 1100 °C were directly observed and recorded by means of a video system. The morphology of each phase and its dependence on growth rate and motherphase composition is discussed, and a morphological phase diagram is given. The observed crystal forms are compared with the results of a Bravais-Friedel- Donnay-Harker analysis. Two new metastable phases are described and their location in the phase diagram is indicated.*

---

* Present address: Drukker International B.V.
Beversestraat 20, 5431 SH Cuijk, The Netherlands.

1. Introduction

During the last few years in situ microscopy has proved to be a powerful method for the investigation of crystal growth processes in low temperature aqueous solutions. By the observation of time dependent patterns on crystal surfaces, actually operating growth mechanisms were determined and new crystal growth models could be tested [1]. Recently the in situ method was adapted for studying crystal growth in fluxes and melts at elevated temperatures [2,3,4]. A domain of crystal growth that was difficult of access was thereby opened up to direct observation.

The equilibrium phase diagram of the Bi_2O_3-GeO_2 system is quite well known [5,6]. It interrelates the properties of the stable melts and the stable compounds $Bi_{12}GeO_{20}$, $Bi_4Ge_3O_{12}$ and $Bi_2Ge_3O_9$. In addition a metastable phase diagram has been measured, containing the Bi_2GeO_5 compound [5,7]. These diagrams were measured by means of differential thermal analysis (DTA). This technique gives information on the temperatures and enthalpies of the phase transitions, but not on the mechanisms involved.

The aim of the present study was to obtain structural information, complementary to the equilibrium phase diagram, related to the various growth processes. This was realized by direct, in situ microscopic observation. In contrast to a previous article on the growth of bismuth germanate from a melt of fixed composition [3], now phase transitions in the whole composition range of the Bi_2O_3-GeO_2 system will be considered.

2. Experimental

2.1. Growth system and optical technique

The growth system was the same as described in ref [3]. A short description is given below.

In a water cooled brass chamber a .35 mm diameter Pt-20%Rh wire is mounted the center of which is shaped into a loop. To allow for observation by transmission microscopy the shape of this loop is adjusted precisely so that a thin plane parallel film of the sample liquid is formed by surface tension. The liquid is heated by a current passing through the wire. To avoid electrolysis effects, alternating current (18 kHz) is used. Temperature stability is better than 2 °C in a 15 min. period. Absolute temperature determination is less accurate: ± 25 °C.

The experiments were carried out in an oxygen atmosphere, except for experiments at liquid compositions below 30 mol% GeO_2, in which air or a nitrogen atmosphere was used.

The microscopic images were recorded on video tape by means of an IR sensitive video camera connected to an analog contrast amplifier. When neccesary a high pass (λ > 780 nm) filter, and neutral density absorption filters were used.

2.2. Source materials and sample preparation

In the composition range 10 mol% GeO_2 to 90 mol% GeO_2 samples were prepared in the following manner. High purity $Bi_4Ge_3O_{12}$ powder and 5N GeO_2 powder or 4N Bi_2O_3 powder were weighed in the desired proportions and mixed thoroughly in an agate mortar. After homogenisation the mixtures were compressed into pellets which could conveniently be added to the growth cell.

2.3. X-ray powder diffraction

For identification of the observed phases some of the samples were analysed by X-ray powder diffraction. To this end the samples (volume $\approx$ 1.5 mm^3) were quenched, removed from the growth cell and carefully grinded.

2.4. Considerations regarding the phase diagram Bi_2O_3-GeO_2

According to ref. [5], five stable compounds crystallize from the liquid; in addition one metastable compound is described. The composition range of the (stable) phase diagram can therefore be thought partitioned into seven portions, each containing a liquidus part ranging from a compound to an eutectic composition.

Three L-S growth situations can thus be anticipated:

i. Stoichiometric composition: The pure compound crystallizes by melt growth;

ii. Liquidus growth: A crystallization trajectory is present. In the course of the experiment , when more and more of the volume crystallizes, the composition and temperature will change markedly towards the eutectic point.

iii. Eutectic growth: Two phases crystallize simultaneously by flux growth.

In principle each of the crystalline phases can undercool substantially, anywhere along the liquidus. This may give rise to a whole collection of metastable eutectics, between stable and metastable compounds. In DTA measurements, this can lead to very complicated results [5].

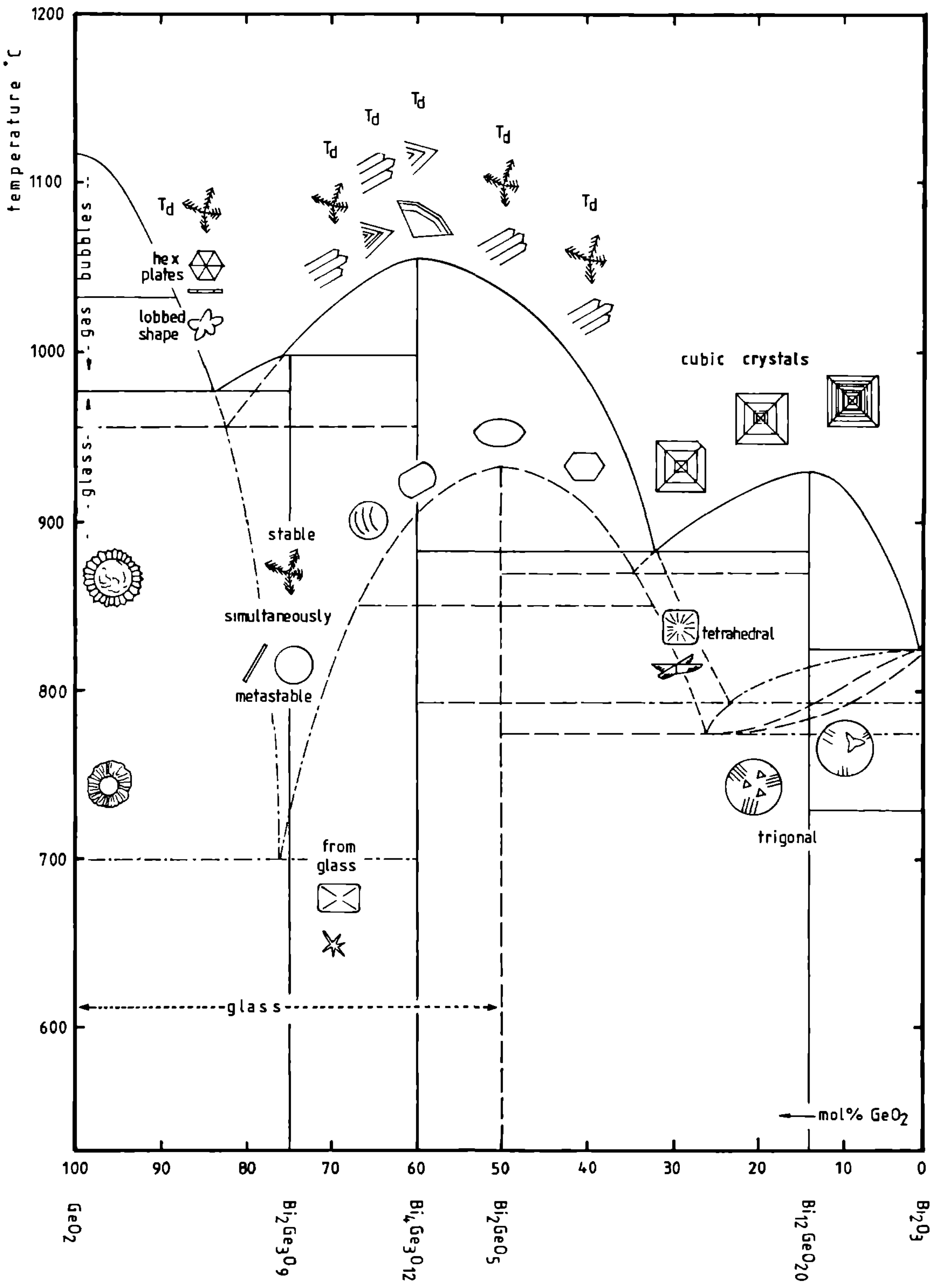
temperature °C
1200
1100
1000
900
800
700
600
gas bubbles
glass
Td
Td
Td
Td
Td
Td
hex plates
lobbed shape
stable
simultaneously
metastable
from glass
glass
cubic crystals
tetrahedral
trigonal
← mol% GeO_2
100
90
80
70
60
50
40
30
20
10
0
GeO_2
$Bi_2Ge_3O_9$
$Bi_4Ge_3O_{12}$
Bi_2GeO_5
$Bi_{12}GeO_{20}$
Bi_2O_3

3. Observations

For the investigations, a number of liquid compositions systematically spread over the composition range of the phase diagram was selected. Most liquids showed a strong tendency to undercool, and metastable phases could easily be grown and observed. When necessary the stable phase was nucleated by introduction of a cold point into the undercooled liquid.

In the following, the formation of the solid phases in liquids of varying compositions are described. The dynamic images of nucleating, growing and dissolving crystals at low and high rates contain a rich abundance of fascinating details which could not all be pursued within the scope of this paper. Therefore we feel that this is only a survey of the phenomena in this phase diagram.

A compilation of the typical morphologies that were encountered is depicted in fig. 1 ,at their location of occurrence in the phase diagram.

3.1. The $Bi_4Ge_3O_{12}$ phase

At 60 mol% GeO_2, the stoichiometric composition for $Bi_4Ge_3O_{12}$, the melt tends to undercool strongly. At low growth rates the $Bi_4Ge_3O_{12}$ compound (from now on refered to as BGO^{60}) grows as well shaped, facetted crystals (fig. 2a) in a very convective melt. Apparently the viscosity at this composition and temperature (1055 °C) is low. At high growth rates the growth front becomes cellular, but remains facetted.

By manipulation of the temperature, often a stationary situation could be created where a single crystal moves from a lower to a higher temperature region, thereby simultaneously growing at the cold side and melting at the hotter side. This gives the illusion of the camera being locked into the growth front of an outgrowing crystal.

At 65 mol% GeO_2 the cellular growth is more pronounced (fig 2b). From the morphology of the teeth patterns, it was derived that most probably the growth directions are $<\bar{1}\bar{1}\bar{1}>$, the tips of the teeth are bounded by the fast growing $\{\bar{1}\bar{1}\bar{2}\}$ facets, and the sides are formed by the slower growing {112} facets (see fig. 3 of ref. [8]). At high growth rates the habit changes from cellular to dendritic.

Fig. 1. Growth morphology of stable and metastable crystal phases in the system Bi_2O_3 - GeO_2. The background phase diagrams are reproduced from Corsmit et al. [5]. The morphologies are derived from in situ observations at the indicated compositions. In the area 40 to 75 mol% GeO_2 the upper and lower drawings along the stable liquidus represent the morphologies at respectivily high and low growth rates.

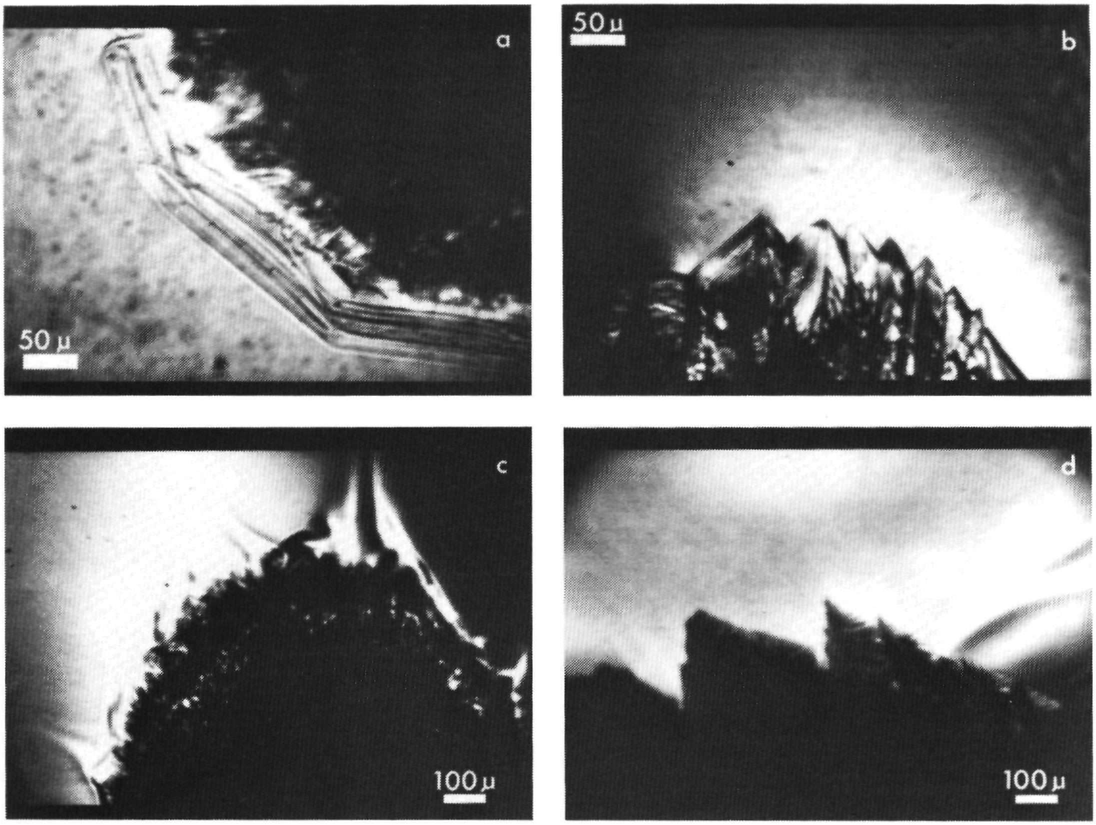

Fig. 2. In situ microscopic images of $Bi_4Ge_3O_{12}$ *('*BGO^{60}*') crystals growing from liquids of different compositions: (a) facetted growth from the melt at 60 mol% GeO*$_2$*; (b) cellular growth at 65 mol%* GeO_2*; (c) concentration gradients causing a 'Schlieren effect' at 70 mol%* GeO_2*; (d) fine dendritic growth at 75 mol%* GeO_2*.*

At 70 mol% GeO_2 the viscosity of the liquid is much higher and at low solidification rates BGO^{60} grows cellular, with smaller tip sizes. In the microscope BGO^{60} appears as bright colourless crystals in a dark red liquid. A strong 'Schlieren' effect is noted during growth and especially during dissolution (fig. 2c). Apparently the rejected liquid (GeO_2 during growth and BGO^{60} during dissolution) mingles very slowly due to the high viscosity of the flux. At high growth rates the morphology changes into fine tetrahedral dendrites ("pine trees"), as in fig. 2d, with secondary and tertiary side branches.

At 75 mol% GeO_2, always a dendritic growth front is found for BGO^{60} , ranging from slight (thick branches) to extremely dendritic ("pine trees", fig. 2d) for increasing growth rates. Nucleation seems to be much more localized: instead of a few nuclei rapidly growing out, now many small isolated tetrahedral crystals throughout the whole liquid are generated after a sharp decrease in temperature.

Sometimes circular platelets are nucleated simultaneously with the stable phase, which after further growth are 'eaten up' by the stable dendrites. Examination of a quenched sample with polarisation microscopy showed the platelets to be very thin, and optically anisotropic in each direction. The composition of the liquid is equivalent to the stoichiometric composition of the hexagonal $Bi_2Ge_3O_9$ (BGO^{75}) phase, with space group P $6_3/m$ and cell parameters c= 9.786 Å and a= 7.006 Å [6]. The expected morphology according to the Friedel-Bravais-Donnay-Harker law [9] is a hexagonal crystal, columnar along the c-axis. The optical axis is parallel to the c-axis, so this should be an optically isotropic direction. Since the expected morphology and optical behaviour do not agree with the observations it can be concluded that the platalets are not the BGO^{75} phase. Probably they constitute the metastable Bi_2GeO_5 phase, which agrees with the observations by Corsmit et al. that BGO^{75} does not nucleate spontaneously from a melt.

On the Bi_2O_3-rich side of the stoichiometric BGO^{60} composition, the growth morphology is not very different from that on the GeO_2-rich side. This in spite of the fact that here during growth a Bi_2O_3-rich liquid is rejected from the solidification front, and the viscosity is less.

At 50 mol% and 40 mol% GeO_2 no single crystals can be grown. Pronounced cellular growth (facetted) is found at low growth rates, which changes into more dendritic growth with coarse secondary branches at high growth rates. No fine dendrites are observed here.

At 40 mol% GeO_2 the stable BGO^{60} and the metastable BGO^{50} are found nucleating simultaneously. No glass could be produced at this composition. This confirms the observations of K. Nassau et al. [10] who report the region of glass formation as 100 - 50 mol% GeO_2.

At 30 mol% GeO_2, at the opposite side of the eutectic point, no BGO^{60} was observed.

3.2. The metastable Bi_2GeO_5 phase

At 60 mol% GeO_2 the Bi_2GeO_5 ('BGO^{50}') phase is easily crystallized from a highly undercooled liquid. The crystals have a circular platelike habit as was described in detail in ref. [3]. The identity of the platelets was verified by in situ polarization microscopy : all crystals were optically anisotropic. This excludes the BGO^{60} and the BGO^{14} phase, which have a cubic lattice. The identification of BGO^{50} was confirmed by X-ray diffraction. It was observed that at very low growth rates two opposite sides of the platelets are facetted (fig. 3a). This indicates that under the present experimental conditions these faces are just below their -equilibrium- roughening temperature [11]. At somewhat higher growth

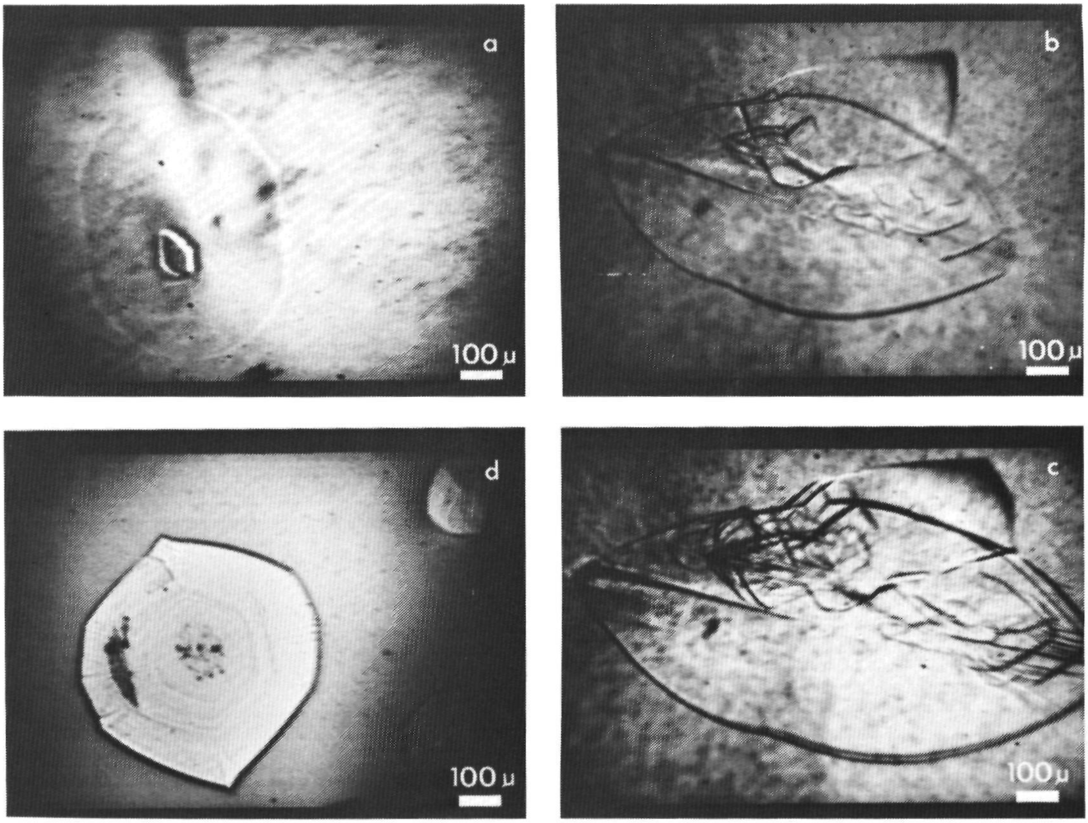

Fig. 3. In situ microscopic images of metastable Bi_2GeO_5 *crystals growing from liquids of different compositions: (a) partly facetted platelets at low growth rate, at 60 mol%* GeO_2*; (b) rounded platelets from the melt at 50 mol%* GeO_2*; (c) as (b), after a time interval of 1 second; (d) platelets at high growth rate, at 40 mol%* GeO_2.

rates the faces disappear due to kinetical roughening [12].

At 65 mol% GeO_2, in a treacly liquid, only the circular platelets occur.

BGO^{50}, growing from the *70 mol%* GeO_2 liquid has a rectangular platelike habit. This liquid solidifies very easily into (brown) glass. In one experiment this glass was slowly heated. At ≈ 600 °C the metastable BGO^{50} started to crystallize from the glass, growing out as needles and as irregular rectangular plates (fig. 8d). At ≈ 700 °C the metastable (orange coloured) crystalline mass recrystallized slowly into BGO^{60}. Sometimes the BGO^{60} is formed directly from the glass.

At 75 mol% GeO_2 (and ≈ 750 °C) BGO^{50} crystallizes as very thin circular platelets together with the stable phase, as was mentioned above. Apparently the maximal undercooling for the stable phase is about 250 °C at this point.

On going to *85 mol% GeO_2*, the metastable eutectic is crossed according to the phase diagram. Indeed no BGO^{50} was found.

50 mol% GeO_2 is the stoichiometric composition of BGO^{50} (see fig. 1). At 930 °C BGO^{50} grows from its metastable melt as elliptically shaped platelets (fig. 3b,c). These are much thicker than the platelets encountered at 60 mol% GeO_2 and other compositions. Advancing macrosteps are more often seen on the top and bottom faces. Apparently growth along the {100} faces is much hampered at off-stoichiometric compositions. Sometimes on the platelets new platelets are nucleated, parallel to the basal plane , both in the correct orientation or 90 degrees rotated.

At 40 mol% GeO_2, the metastable liquid is more viscous, and the optical transparency has decreased. An approximately hexagonal platelet habit was found here (fig. 3d). At moderate and higher growth rates kinetical roughening occurs and the facetted edges become rounded and tend to to be dendritic.

At 30 mol% GeO_2 the BGO^{50} phase was not detected. Instead a metastable phase with different crystal symmetry was found (see sect. 3.4).

3.3. The $Bi_{12}GeO_{20}$ phase

According to the equilibrium phase diagram, $Bi_{12}GeO_{20}$ (BGO^{14}) is the stable phase in the region 32 - 1 mol% GeO_2.
At 30 mol% GeO_2, intentional disturbance of the undercooled liquid yields yellow coloured cubic crystals (fig. 4d) growing in a convective liquid. X-ray powder diffraction established this phase to be $Bi_{12}GeO_{20}$ [13]. At low growth rate, visually perfect crystals can be grown. At high growth rates growth striations are formed, but the sides remain completely flat and no dendritic distortions are brought about. This indicates a very strong tendency to facetting: apparently the cube, {100}, faces grow far below their roughening point.

At 20 mol% GeO_2 the liquid is more viscous, and its optical transparency is decreased to such an extent that even in the near-IR region no clear images can be obtained.
It was discovered here that upon exchanging the oxygen atmosphere by air or a nitrogen atmosphere, transparency can be improved dramatically (see sect. 5.). Therefore, observations at 20 mol% and 10 mol% GeO_2 were carried out in a nitrogen atmosphere.

The morphology of the stable BGO^{14} phase at 20 mol% is similar to its morphology at 30 mol% GeO_2 : strongly facetted cubes. Often only one nucleus is formed, which yields one growing crystal in the liquid. A very elegant experiment could be conducted here as follows. Upon increasing the temperature of the growth cell, such a single crystal cube dissolves slowly, thereby changing its shape

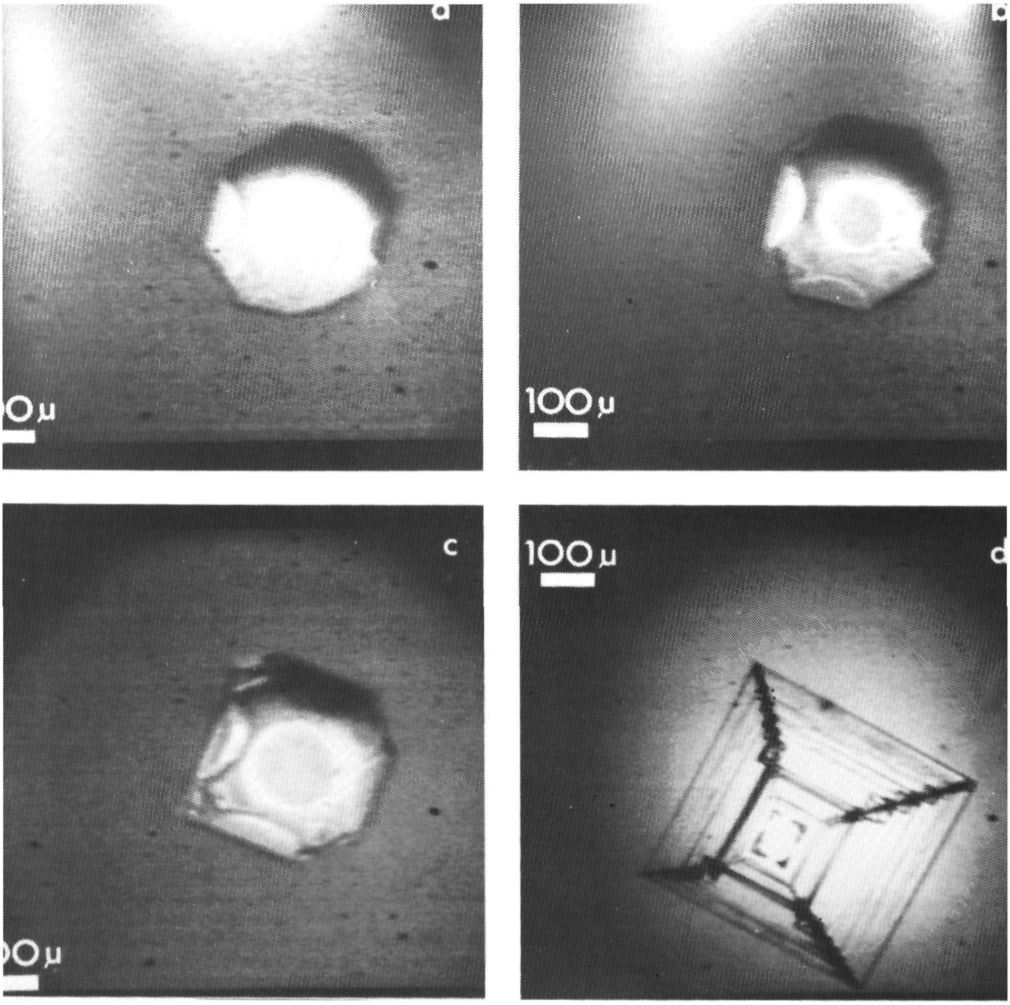

Fig. 4. Crystal morphology of $Bi_{12}GeO_{20}$: (a,b,c) in situ sphere growth experiment at 20 mol% GeO_2 showing the development of cubical {100},{110} and {111} or {112} faces; (d) cubic crystals at 30 mol% GeO_2; (e) schematic drawing of (b).

very quickly into an almost perfect sphere. By creation of such a sphere, as large as possible, and permitting it to grow again very slowly, an 'in situ sphere growth experiment' [14] could be carried out (fig. 4). In principle each F-face [15] which occurs in the crystal structure of BGO^{14} and which is not roughened at the conditions of growth should develop on the sphere. The Morphological Importance [15] of these F-faces can then be determined from their relative widths. In figure 4a,b,c it is clearly visible that the {100} and {110} faces are respectively the first and second in

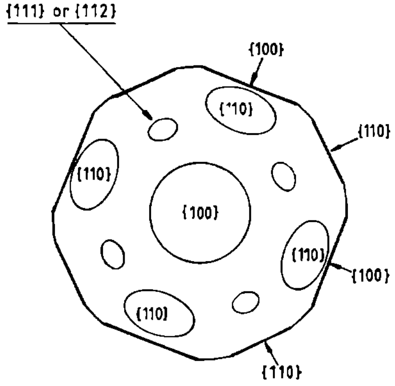

morphological order. Further smaller, third order faces {111} or {112}, which one is not clear from the in situ images, can be seen. Since no other faces appear on the sphere it is concluded that the fourth and higher order faces are roughened.

At 10 mol% GeO$_2$, BGO[14] also grows with cubic morphology, in an almost opaque liquid. The infrared images were obtained from an extra thin liquid film.

3.4. The metastable phases at the Bi_2O_3-side of the phase diagram

At 30 mol% GeO$_2$ a metastable phase nucleates at lower temperature, and in a more viscous and less transparent liquid than the adjacent composition 40 mol% (sect. 3.2). Upon lowering the temperature, many nuclei are formed almost instantaneously, emerging from one point in the liquid (possibly a solid residu). The nuclei grow out into crystals with two entirely different morphologies (fig. 5,6), which do not depend on size and growth rates.

One type has the shape of feathered wings. These wings grow out primarely in the two opposite tip directions, and broaden in a direction 30° apart from these in the same halfplane (fig. 5a,b). Sometimes several 'wings' are attached to each other at various angles at their nucleation point. This gives a butterfly-like impression (fig. 6d).

The other type comprises very thin (few µm) square platelets with rounded corners.

These two morphologies always appear together. In addition it was observed that at higher growth rates the edges of the platelets (growth front) become somewhat cellular, the cells having the appearance of a parallel series of wings, closely resembling the wings described above. Therefore the two morphologies probably belong to the same crystal phase.

At 20 mol% GeO$_2$ another metastable phase is formed, which crystallizes as circular platelets at low and high growth rates (fig. 7a). The patterns on the plate surfaces are characterized by perfect triangular features which apparently accompagny thickness growth. Further near the perifery, lines parallel to the sides of the triangles can be seen, which are left behind by the fast growing (roughened) sides. This points to a crystal structure with trigonal symmetry and a unit cell in which the c-axis is much longer than the

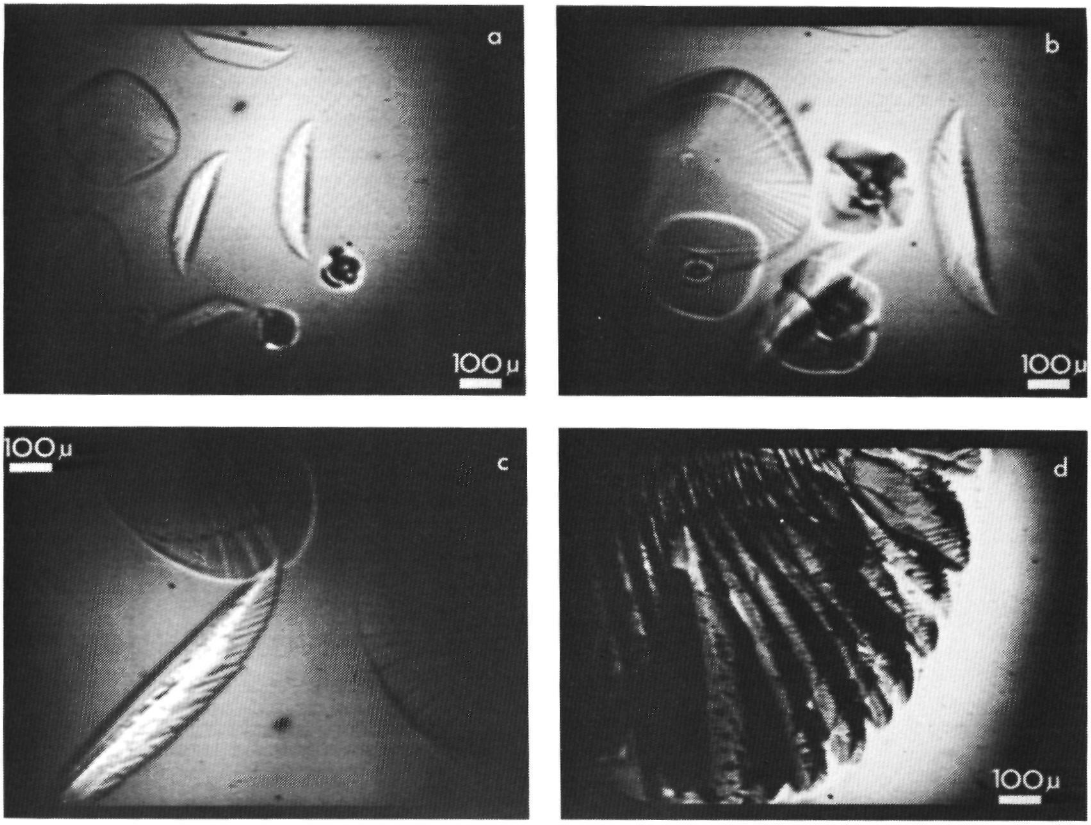

Fig. 5. In situ microscopic images of the metastable phase formed at 30 mol% GeO_2: (a,b) growing wing-shaped and plate-shaped crystals recorded with a time interval of 0.1 seconds; (c) wing shaped crystal growing from the tip; (d) growth front at the side of a platelet: note the similarity with the morphology at (c).

a-and b-axes (sect. 4.). From X-ray analysis of the samples no additional information was obtained (sect. 5). Sometimes another phase was noted, nucleating on top of the platelets (fig. 7b) and growing as thick rounded tetrahedral dendrites. This is indicative for cubic symmetry.

At 10 mol% GeO_2 the triangles on the platelets become rounded with a dendritic appearance. Despite this alteration the three-fold symmetry persists. It is suggested that here the trigonal phase is further away from its stoichiometric composition than at 20 mol% .

Pure Bi_2O_3 melt is opaque for visible and near-IR light and therefore it was not accessible to in situ examination.

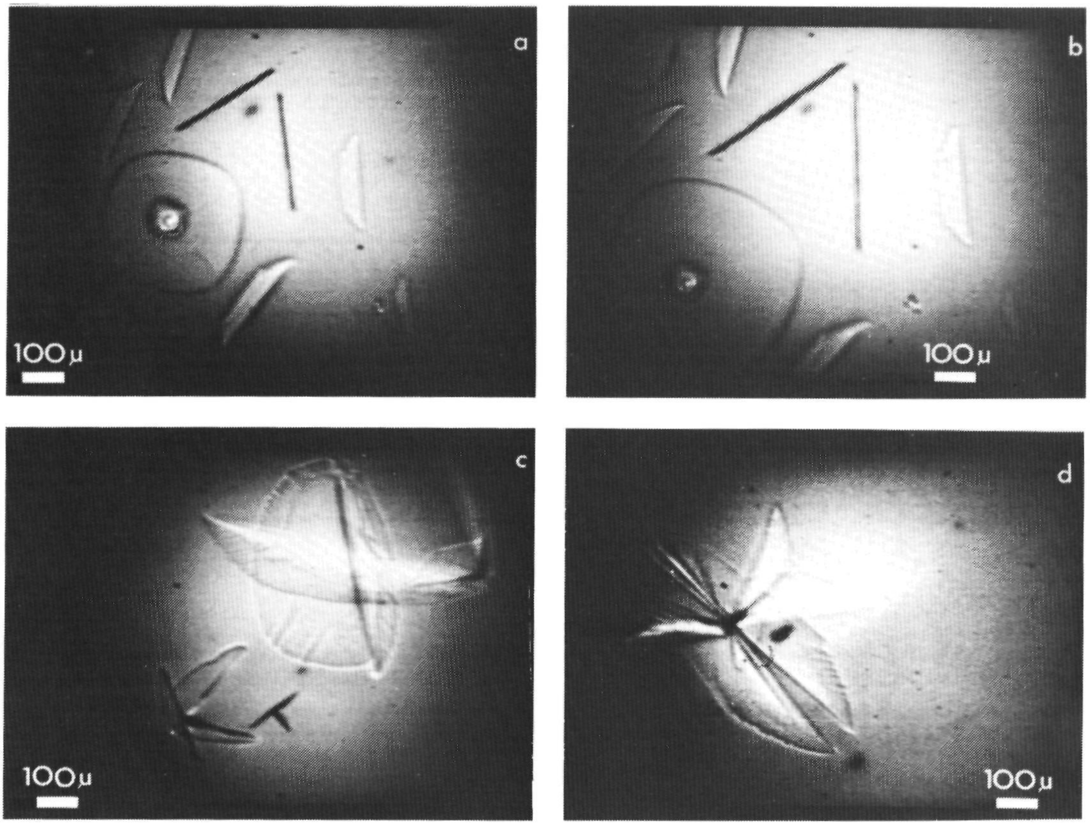

Fig. 6. In situ microscopic images of the metastable phase at 30 mol% GeO_2: (a,b) growing crystals recorded with a time interval of 0.1 seconds; (c,d) wing shaped crystals.

3.5. The GeO_2-rich side of the phase diagram

At 85 mol% GeO_2, left from the stable eutectic, an extremely thick liquid is encountered. Three types of crystals were observed here at 900 - 1000 °C:

i) Thin hexagonal platelets (diameter to thickness ratio of about 15). According to the equilibrium phase diagram this might be the high temperature GeO_2 phase (table 1.) or the BGO^{75} phase;

ii) Isolated, extreme dendrites with tetrahedral symmetry (fig. 8c), clearly recognizable as BGO^{60} ;

iii) An unclear shaped growth form (fig. 8a), which resembled a slightly or not facetted, truncated octahedron.

Since the solidified material was composed of three or more

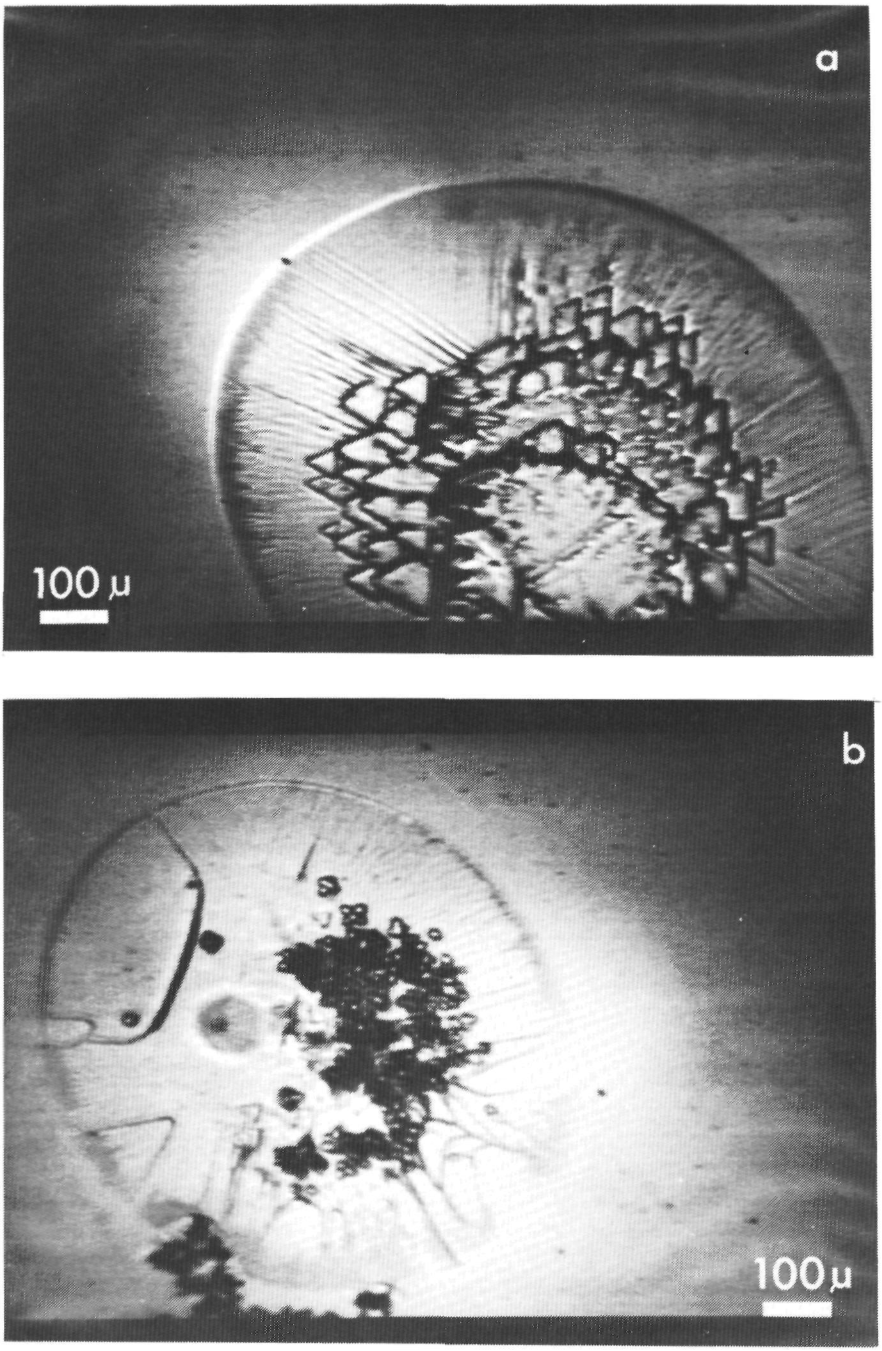

Fig. 7. In situ microscopic images of the metastable phase at 20 and 10 mol% GeO_2: (a) circular platelets with trigonal symmetry at 20 mol%; (b) circular platelets with a second phase at 10 mol% GeO_2. An improved image quality was obtained by using a N_2 atmosphere.

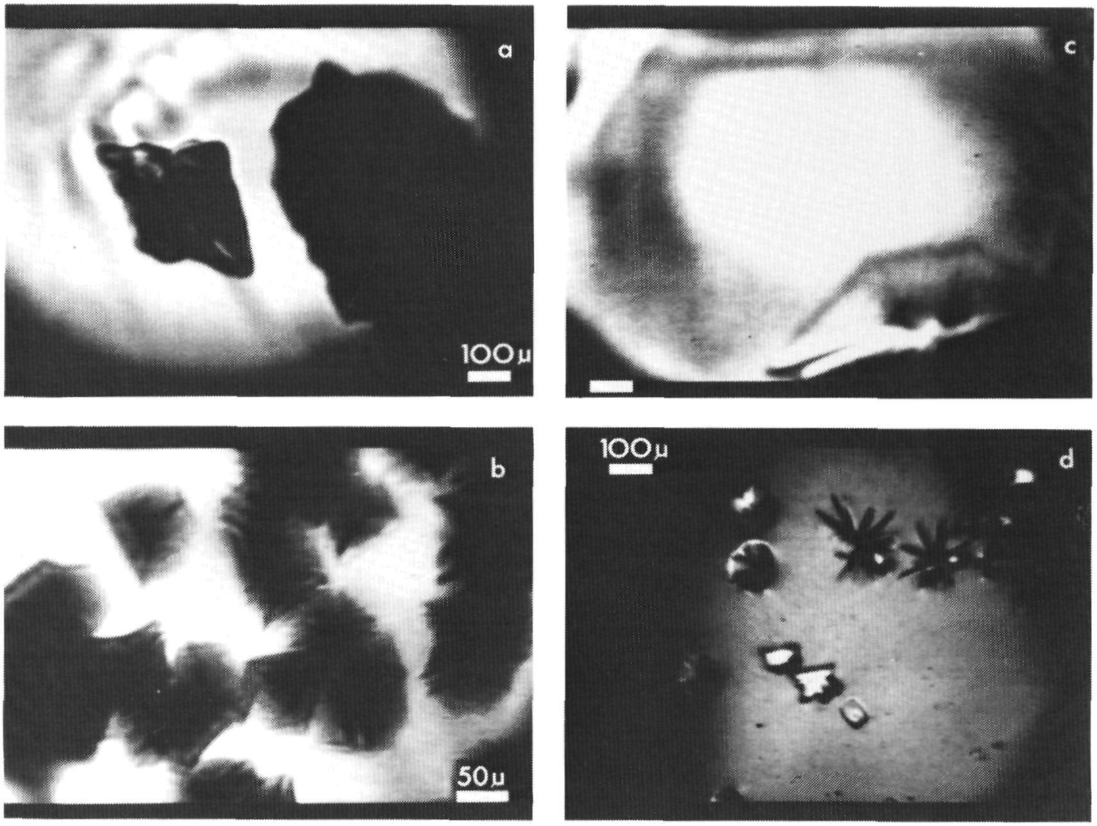

Fig. 8.a,b,c In situ microscopic images of crystal phases at 85 mol% GeO$_2$: (a) rounded irregular crystals, probably GeO$_2$; (b) hexagonal platelets, probably Bi$_2$Ge$_3$O$_9$; (c) isolated tetrahedral dendrites, Bi$_4$Ge$_3$O$_{12}$.
Fig. 8d Bi$_2$GeO$_5$ growing from the glass phase at 70 mol% GeO$_2$. Temperature approximately 850 °C.

phases, no X-ray work was carried out for further crystallographic identification. These different types of crystals were found simultaneously floating and growing in the same liquid, all very slowly. Apparently considerable inhomogeneity can occur, due to the high viscosity. None of these phases requires large supersaturation to nucleate. Any attempts to increase the growth rate by lowering the temperature promptly turned the liquid into glass. This also prevented the observation of lower temperature metastable phases.

Additional observations at 80 mol% GeO$_2$ showed the -most probably- BGO^{75} phase to crystallize as very thin hexagonal plates, and the GeO$_2$ phase as extremely dendritic curved crystals. Both phases only crystallize after disturbance of the liquid.

The solidification of *pure GeO$_2$* melt was not investigated in detail, because crystal growth was prevented by glass formation.

Recrystallization of GeO$_2$ glass at 800 - 900 °C yielded prismatic shaped, optically anisotropic crystals.

Crystal phase	**Crystal System**	**Space Group**	**Cell parameters Å**	**Stoichiom. melting point °C**	**Ref.**
GeO$_2$ (HT) β-quartz	hex	P3$_1$21	a= 4.987 c= 5.652	1116	[24]
GeO$_2$ (LT) rutile	tetra	P4/m2/m2/m	a= 4.395 c= 2.866	(1086) tr.1049	[24]
Bi$_2$Ge$_3$O$_9$ (BGO^{75})	hex	P6$_3$/m	a= 7.006 c= 9.786	1010	[25,6]
Bi$_4$Ge$_3$O$_{12}$ (BGO^{60})	cubic	$I\bar{4}3d$	a=10.497	1055	[26,8]
Bi$_2$GeO$_5$ (BGO^{50})	orthor.	Ama2	a=15.681 b= 5.493 c= 5.384	(931)	[27,28, 3]
Bi$_{12}$GeO$_{20}$ (BGO^{14})	cubic	I23	a=10.145	920	[13]
α-Bi$_2$O$_3$ (LT)	monocl.	P2$_1$c	a= 5.848 b= 8.166 c= 7.510 ß= 113°	tr. 730	[23]
δ-Bi$_2$O$_3$ (HT)	cubic	Pn3m	a= 5.66	825	[23]
β-Bi$_2$O$_3$ (metast.)	tetra	$P\bar{4}2_1c$	a= 7.750 c= 5.631		[23]

Table 1.

4. Morphological analysis

In general, the morphology of a facetted crystal is described by one or more forms. A form is a set of faces which are equivalent by symmetry. In principle the symmetry of the external shape of a crystal is identical to the pointgroup symmetry of its crystal structure [16]). The relative development of each crystal form on the growth habit (which is equivalent to the morphological importance) can be estimated by application of the Bravais-Friedel-Donnay-Harker law [9]. The BFDH law relates the shape of a crystal to its lattice properties. It is consistent with a surface kinetics limited, layered growth model and calculates the relative growth rates of the different growth forms on the basis of their unit step height. Although it does not take into account the anisotropy of bonds in the crystal, it is generally succesful [15,17,18].

In the following the BFDH law is applied to the crystal phases in the system GeO_2-Bi_2O_3, and a comparison is made with the observed morphologies described in the previous sections.

Table 1 summarizes some crystallographic properties of the phases which are known to occur in the system Bi_2O_3 - GeO_2.

The expected morphology of the phases according to BFDH are presented in table 2. The morphological order of the six most important forms is given in the third row of the table. The resulting crystal shapes derived from this are given in the fourth row (names adopted from ref. [16]). In the fifth row the predicted shapes are compared with the morphologies of the crystals that were observed at low growth rates during the present in situ experiments.

As can be seen the BFDH results agree well with the experimentally determined morphologies:

- For the BGO^{75} phase the {001} faces were found to be dominant. This form was predicted to be third in morphological order.
- As predicted, the habit of BGO^{60} crystals growing from the melt or flux is indeed determined by {112}/$\{\bar{1}\bar{1}\bar{2}\}$ faces. For a thorough morphological analysis of this compound see ref. [18].
- The observed dominant crystal form for the BGO^{50} phase is {100} as predicted. At the stoichiometric composition all the side faces are apparently roughened (fig. 3b). At 60 mol% GeO_2 an additional crystal form is present (fig. 3a). This form must be {hk0} as can be derived from the point group symmetry mm2. Of this family {020} is the highest in morphological order.
- The experimental morphological order of the BGO^{14} phase as determined in the sphere growth experiment (sect. 3.3) is {100},{110},{111} or {112}. This is in conformity with the BFDH analysis. In view of the predictions the third in order is most probably {112}.

In addition it can be concluded from symmetry considerations that the dominant form for the metastable phases at 30 mol% GeO_2 (tetragonal) and at 20 and 10 mol% GeO_2 (trigonal) must be {001}.

It is remarkable that all metastable crystals are thin platelets, whereas the stable ones have a variety of shapes, like cubes, dodecahedra or plates.

Crystal-phase	GeO_2 (HT) β-quartz		GeO_2 (LT) rutile		$Bi_2Ge_3O_9$ (BGO^{75})		$Bi_4Ge_3O_{12}$ (BGO^{60})	
Point-group	32		$\frac{4}{m}\frac{2}{m}\frac{2}{m}$		$\frac{6}{m}$		$\bar{4}3m$	
Donnay-Harker morphology								
M.I.	*{HKL}*	*d Å*	*{HKL}*	*d Å*	*{HKL}*	*d Å*	*{HKL}*	*d Å*
1.	100	4.32	100	4.40	100	6.07	211	4.29
2.	101	3.43	110	3.11	101	5.16	220	3.71
3.	110	2.50	001	2.87	002	4.89	310	3.32
4.	102	2.36	101	2.40	102	3.81	321	2.81
5.	111	2.28	111	2.11	110	3.50	400	2.62
6.	201	2.02	210	1.97	111	3.30	420	2.35
Shape	Hexagonal prism		Tetragonal prism		Hexagonal prism		Tristetrahedron	
Observed morphology								
Shape					Hexagonal plates {001}		Tristetrahedron {112}	

Table 2.

5. Discussion

In sect. 3.1 the growth of the BGO^{60} phase from liquids with compositions between 40 and 80 mol% GeO_2 has been described. The growth morphology at the various compositions can be summarized as follows: Only at, or close to the stoichiometric composition crystal growth proceeds undisturbed and well formed, facetted crystals are obtained. At somewhat off-stoichiometric compositions the growth front becomes serrated and cellular growth occurs, which at higher growth rates changes into dendritic growth. The tendency to dendritic growth increases progressively on going to more off-stoichiometric compositions.

These large changes in morphology can be explained in the following manner. At the stoichiometric composition pure melt growth occurs and only the heat of crystallization has to be transported. Therefore at low growth rate the growth is totally limited by

Bi_2GeO_5 (BGO^{50})		$Bi_{12}GeO_{20}$ (BGO^{14})		α-Bi_2O_3 (LT)		δ-Bi_2O_3 (HT)		β-Bi_2O_3 (metastab.)	
mm2		23		$\frac{2}{m}$		m3m		$\bar{4}2m$	
Donnay-Harker morphology									
{HKL}	*d Å*	*{HKL}*	*d Å*	*{HKL}*	*d Å*	*{HKL}*	*d Å*	*{HKL}*	*d Å*
200	7.84	110	7.17	100	5.38	110	4.00	110	5.48
011	3.84	200	5.07	011	5.28	111	3.27	101	4.56
111	3.73	211	4.14	111	4.50	200	2.83	100	3.88
211	3.45	310	3.21	110	4.49	211	2.31	210	3.47
311	3.10	222	2.93	020	4.08	221	1.89	201	3.19
020	2.75	321	2.71	021	3.52	310	1.79	211	2.95
A-pinacoid		Dodecahedron		A-pinacoid		Dodecahedron		Tetragonal prism	
Observed morphology									
A-pinacoid {100}		Cube {100}, {110}, {211}							

surface kinetics and the crystal shape is dictated by the crystallograpic habit. At off-stoichiometric compositions we will have flux growth and the excess flux has to be rejected from the solidification front (fig. 2.c). Constitutional supercooling causes the growing crystal surface to be cellular. If material transport becomes limiting the dendritic crystal shapes are developed. From the observed relation between off-stoichiometry of the starting materials and crystalline perfection, it is obvious that stoichiometry is a factor of great importance for the production of good quality, large sized BGO^{60} crystals [8].

The growth of the BGO^{50} phase was also observed in the same composition range (sect. 3.2). Compared to the stable compound, its morphology varied considerably less. The metastable crystals are thinner at off-stoichiometric compositions but retain their platelet morphology. Apparently, due to this shape, material transport is much facilitated and does not limit growth, even at the somewhat higher viscosities along the BGO^{50} liquidus.

As was mentioned in sect. 3.2 , side faces appear on the BGO^{50} platelets at 40 and 60 mol% GeO_2. At these compositions the temperature is lower and the interfacial energy is probably higher compared to the stoichiometric composition, which allows these faces to grow beneath their roughening temperature.

Within the composition range of the phase diagram the optical transparency of the (meta)stable liquids changes gradually. At 100 mol% GeO_2 the liquid is completely transparent and colorless. With increasing Bi_2O_3 content, an increasing absorption is noticed in the blue region of the visible light spectrum. At 100 mol% Bi_2O_3, the liquid is opaque. At lower temperature the absorption is less: In a liquid with BGO^{60} composition only I.R light is transmitted at the BGO^{60} melt temperature (1055 °C), whereas at the BGO^{50} liquidus temperature (≈900 °C) it is transparent for red light. This effect was also noticable at Bi_2O_3-richer compositions. The absorption is probably related to the $^1S_0$ to $^3P_0$ or $^3P_1$ electronic transition of the Bi-atom, similar to the absorption in the Bi-containing crystals in this system [20,21]. The increase in optical absorption upon temperature rise must be due to a temperature broadening of the absorption band in question.

In Bi_2O_3-rich liquids the absorption of VIS-IR light was found to be strongly dependent on the composition of the surrounding atmosphere in the growth chamber (sect. 3.4). In gas mixtures N_2/O_2, at constant temperature the absorption decreased for decreasing O_2 content. At 20 and 10 mol% GeO_2 this effect was much larger than the change in absorption with temperature. By using O_2-poor gas mixtures probably dissolved oxygen is removed from the liquid, thereby shifting the composition away from the quasi-binary cross section a.GeO_2-b.Bi_2O_3 in the ternary phase diagram Ge-O-Bi. This possibly changes the liquid structure (entering the B-type liquid area mentioned in ref. [7,22]) or alternativily the oxydation state of a fraction of the Bi-atoms. No changes in crystal morphology were detected however.

The in situ observations are within experimental error consistent with the stable and metastable phase diagrams measured by Corsmit et al. [5]. All the crystal phases mentioned in this work were observed. In addition two new phases were found, respectivily at 30 mol% GeO_2 (tetragonal) and at 20 and 10 mol% GeO_2 (trigonal, sect. 3.4).

For the identification of these phases a number of possibilities is available.

Tanavaev et al. [7,5] suggest a δ^*-Bi_2O_3 solid solution in this area, which however should have cubic symmetry. Medernach et al. [23] have compiled the metastable bismuth-oxides reported in literature and calculated their powder diffraction patterns. Four of these phases are tetragonal, but none of them is trigonal. X-ray analysis of the grown samples at 30 and 20 mol% GeO_2 showed the presence of BGO^{50} and δ^*-Bi_2O_3. However the broadness and irregularity of the peaks in both diffractograms indicate that the metastable phases decomposed during the queching procedure. Therefore the equivalence of the tetragonal phase with one of the tetragonal bismuth oxides is not excluded.

Corsmit et al. [5] reported a solid-solid transition of the metastable BGO^{50} phase at 850 °C. If the metastable eutectic between BGO^{50} and Bi_2O_3 is correctly situated at 26 mol% GeO_2 then crystal growth of the low-temperature BGO^{50} phase can only be observed at the liquidus part between 26 and 31 mol% GeO_2 (fig. 1). Since we did detect the tetragonal phase at 30 mol% GeO_2 but not at other compositions we tentatively ascribe it to the low temperature BGO^{50} phase.

In the interpretation of his data between 26 and 0 mol% GeO_2, Corsmit leaves open two possibilities: The δ^*-solid solution of Tanavaev, or a new compound. The in situ observation of the trigonal phase at 20 and 10 mol% GeO_2 shows the second possibility to be correct. The observations indicate that the stoichiometric composition is approximately 20 mol% GeO_2. The composition of the eutectic point between the trigonal phase and the δ-Bi_2O_3 is below 10 mol% GeO_2.

6. Conclusions

In situ high temperature microscopy is a simple but powerful method for the investigation of growth phenomena in high temperature solutions and melts. It gives supplementary information on the phase diagrams obtained by differential thermal analysis methods.

In the present study the complete Bi_2O_3-GeO_2 system was systematically surveyed. Nucleation, growth and dissolution of the various stable and metastable phases were recorded and examined.

The crystal morphology of all phases observed at low growth rate was confronted with the Bravais-Friedel-Donnay-Harker law, which is applicable for surface kinetics limited growth. In general the BFDH law was obeyed, only minor deviations occurred.

The growth morphology at higher growth rates and at off-stoichiometric compositions could satisfactorily be explained with arguments of mass transfer limited growth.

The phase equilibria following from the in situ observations are in close agreement with the phase diagrams given by Corsmit et al.. In the Bi_2O_3-rich area two new phases were discovered. They could satisfactorily be incorporated within the metastable phase diagram.

Acknowledgements

The authors are indebted to Prof. Dr. P. Bennema, Dr. M. Seal and

Prof. Dr. R.T. Van de Walle for their interest in the present work. They are grateful to H.G. Schaeken for the X-ray powder diffraction work. Part of this study was financially supported by the Foundation for Technical Sciences (STW).

REFERENCES

[1] see for instance: L.A.M.J. Jetten, B. van der Hoek and W.J.P. van Enckevort, J. Crystal Growth 62 (1983) 603.

[2] K. Tsukamoto, T. Abe and I. Sunagawa, J. Crystal Growth 63 (1983) 215.

[3] W.J.P. van Enckevort and F. Smet, J. Crystal Growth 82 (1987) 678.

[4] T. Abe, K. Tsukamoto and I. Sunagawa, ICCG 8, Film session, 1986, York, England.

[5] G. Corsmit, M.A. van Driel, R.J. Elsenaar, W. van de Guchte, A.M. Hoogeboom and J.C. Sens, J. Crystal Growth 75 (1986) 551.

[6] A.A. Kaminskii, S.E. Sarkisof, A.A. Maier, V.A. Lomonov, D.V. Asafov and P.N. Zakaznov, Izv. Akad. Nauk. SSSR, Neorg. Mater. 19 (1983) 1035.

[7] I.V. Tanavaev, V.M. Skorikov, Yu.F. Kargin and P. Zhereb, Izv. Akad. Nauk. SSSR, Neorg. Mater. Vol 14, 11 (1978) 2024.

[8] F. Smet and W.J.P. van Enckevort, J. Crystal Growth 88 (1988) 169.

[9] J.D.H. Donnay and D. Harker, Am. Mineralogist 22 (1937) 446.

[10] K. Nassau and D.L. Chadwick, J. Am. Cer. Soc. 65 (1982) 199.

[11] see for instance: J.P. van der Eerden, P. Bennema and T.A. Cherepanova, Prog. Crystal Growth Charact. 1 (1978) 219.

[12] M. Elwenspoek, Appl. Phys. A41 (1986) 123.

[13] S.C. Abrahams, P.B. Jamieson and J.L. Bernstein, J. Chem. Phys. 47 (1967) 4034.

[14] B. Honigmann, Gleichgewichts- und Wachstumsformen von Kristallen (Steinkopff, Darmstadt, 1958).

[15] P. Hartman in: Crystal Growth: An Introduction, Ed. P. Hartman (North-Holland, Amsterdam, 1973) p. 367.

[16] M.J. Buerger, Elementary Crystallography (Wiley, London, 1963) p. 119.

[17] see for instance: R.A. Terpstra, P. Bennema, P. Hartman, C.F. Woensdregt, W.G. Perdok and M.L. Senechal, J. Crystal Growth, 78 (1986) 468.

[18] P. Bennema and J.P. van der Eerden in: Morphology of Crystals, Ed. I. Sunagawa, Vol A (Reidel, Dordrecht, 1988), p. 72.

[19] F. Smet, P. Bennema, J.P. van der Eerden and W.J.P. van Enckevort, J. Crystal Growth, accepted.

[20] G. Boulon, B. Moine and J.C. Bourcet, Phys. Rev. B22 (1980) 1163.

[21] C.W.M Timmermans and G. Blasse, J. Solid State Chem. 52 (1984) 222.

[22] V.P. Zhereb, Yu.F. Kargin and V.M. Skorikov, Russ. J. Inorg. Mater. 14 (1978) 1580.

[23] J.W. Medernach and R.L Snyder, J. Am. Cer. Soc. 61 (1978) 494.

[24] R.P. Eliot, Constitution of Binary Alloys, First Supplement (McGraw-Hill, New York, 1965), p. 483.

[25] B.C. Grabmaier, S. HaussÜhl and P. KlÜfers, Z. Kristallogr. 149 (1979) 261.

[26] A. Durif and M Averbuch-Pouchot, Compt. Rend. (Paris) 295 (1982) 555.

[27] B. Aurivillius. C.I. Lindblom and P. Sténson, Acta Chem. Scand. 18 (1964) 6.

[28] A.V. Firsov, N.E. Skorokhodov, A.V. Astaf'ev, A.A. Bush, S.Yu. Stefanovitch and Yu.N. Venevtsev, Sov. Phys. Crystallogr. 29 (1984) 304.

CHAPTER 3

THE GROWTH OF LARGE SINGLE CRYSTALS

Journal of Crystal Growth 88 (1988) 169–179
North-Holland, Amsterdam

ON THE DISTRIBUTION OF POINT DEFECTS IN LARGE SIZED BISMUTH GERMANATE CRYSTALS

F. SMET and W.J.P. VAN ENCKEVORT *

Department of Solid State Chemistry and Department of High Energy Physics, Faculty of Science, University of Nijmegen, Toernooiveld, 6525 ED Nijmegen, The Netherlands

Received 24 November 1987

The spatial distribution of UV–blue absorbing point defects in Bridgman grown bismuth germanate ($Bi_4(GeO_4)_3$) crystals has been imaged by means of UV absorption topography From the occurrence and position of growth bands and sector boundaries it was concluded that in all conditions the crystals only grow via the crystallographic non-equivalent $\{112\}$ and $\{\bar{1}\bar{1}\bar{2}\}$ facets The exclusiveness and the F-type character of the (slower growing) $\{112\}$ and (faster growing) $\{\bar{1}\bar{1}\bar{2}\}$ faces were confirmed by sphere growth experiments and ex-situ surface microtopography Within many crystals it was found that the $\{112\}$ sectors show a higher UV–blue absorption and thus an enhanced impurity segregation than the adjacent $\{\bar{1}\bar{1}\bar{2}\}$ sectors This points to kinetically (i e non-equilibrium) determined segregation Imaging of crystals by the Schlieren method showed a higher optical density for the $\{\bar{1}\bar{1}\bar{2}\}$ growth sectors. Laser light scattering disclosed a preferential occurrence of inclusions near sector boundaries

1. Introduction

In recent years, single crystalline $Bi_4Ge_3O_{12}$ (BGO) has become increasingly important as a scintillator material for nuclear medicine, industrial and high energy physics applications [1,2]. Due to its short radiation length, it is particularly suitable for high energy calorimetry in the GeV range [1,2]. Therefore BGO is intended to be used as detector material in forthcoming LEP-3 experiments at CERN [2]. Many applications require the production of larger, high quality crystals, free from voids and coloration.

The two major difficulties that were encountered during Bridgman growth of large BGO crystals are:

(a) A yellowish colour caused by impurities and deviations from stoichiometry. This lowers the optical transmission of the crystal considerably and thus introduces a decreased scintillation efficiency.

(b) The formation of voids and inclusions.

The investigation presented in this paper was concentrated primarily on the coloration and its inhomogeneous distribution in relation to the growth history and growth morphology of the crystals. The inclusions were recently investigated by Horowitz and Kramer [3].

2. Experimental

2.1. Crystal growth and specimen preparation

The bismuth germanate crystals used in this study were produced by the research group at the department of High Energy Physics. University of Nijmegen. The crystals, with dimensions up to 25 × 3 × 3 cm^3 were grown by both vertical and horizontal Bridgman techniques. During crystal growth a platinum crucible filled with molten BGO was translated at a rate of 0.5–5 mm/h through a temperature gradient of 2–20 °C/cm.

To investigate the interior of the crystals by optical methods, windows were polished at the side faces of the BGO boules. To obtain a view end-on, from some crystals slices were cut normal to the growth direction and subsequently polished.

---

* Present address Drukker International B V., Beversestraat 20, 5431 SH Cuijk, The Netherlands

0022-0248/88/$03.50 © Elsevier Science Publishers B.V.
(North-Holland Physics Publishing Division)

2 2 Morphological methods

To obtain information on the crystal habit during growth, sphere growth experiments [4] were carried out The necessary spheres were made by machining single crystalline BGO material with a lathe The crystal spheres were slightly grown in a supercooled melt ($\Delta T = 1$–$2°C$) during a few minutes and then quickly removed In this way relatively unperturbated surfaces were obtained The resulting morphology of the spheres was examined by optical goniometry

Small crystals for morphological studies were obtained by dipping a Pt wire for a few minutes in a supercooled melt After separation from the liquid several crystallites (~ 3 mm in size) were nucleated on the wire

For topological examination of as-grown surfaces, polished crystal plates (~ $20 \times 20 \times 2$ mm^3) parallel to {112} were slightly grown in the same manner as the spheres The growth patterns on the plate surfaces were observed by a Nomarski interference contrast microscope

To characterize the crystallographic polarity of the crystals [5] several {112} and $\{\bar{1}\bar{1}\bar{2}\}$ faces were etched with 10% HCl in H_2O solution during 10 30 min prior to optical microscopy

2 3 Optical characterization methods

2 3 1 UV absorption topography

Variations in growth circumstances in time and place lead to differences in impurity segregation along and across crystals [6] For BGO the impurities generally give rise to an enhanced blue, ultraviolet light absorption [7,8] Fig 1 shows the VIS UV absorption spectra (recorded by a conventional technique) from two adjacent regions in the same crystal Clearly a large difference can be seen in the near ultraviolet region

To image the spatial distribution of the impurity absorption centra, light absorption topographs [9] were made by projecting crystals with two parallel polished windows in a nearly parallel light beam directly on a high contrast, fine grain photographic film As can be seen from fig 1, the

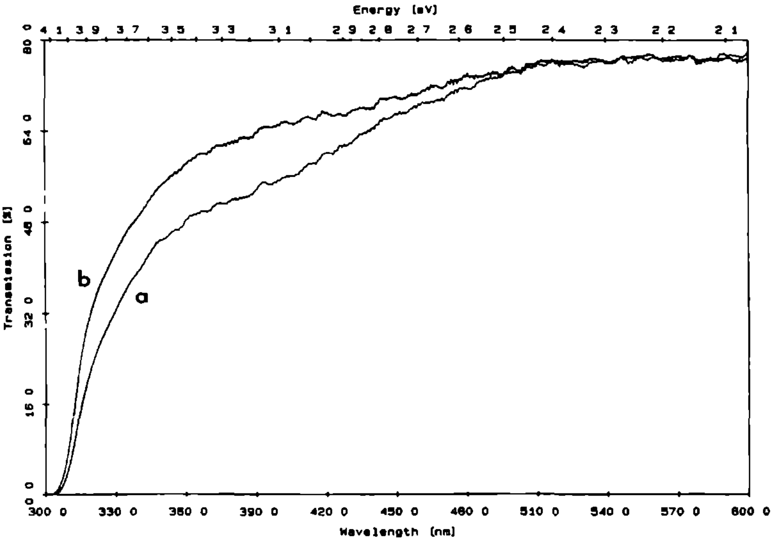

Fig 1 VIS–UV absorption spectra of two neighbouring growth sectors in the same Bridgman ($\langle\bar{1}1\bar{2}\rangle$) grown crystal (a) {112} growth sectors (b) $\{1\bar{1}\bar{2}\}$ growth sectors

maximum variation in transmitted light intensity is expected to occur near the absorption edge of BGO, $\lambda \approx 300$ nm. Therefore, to obtain maximal contrast, light was used in the wavelength range of 300–400 nm.

2.3.2. Light scattering

The presence and distribution of inclusions was investigated by means of a simple laser light scattering technique. An optical arrangement made up of a 10 mW He–Ne laser, a beam expander and a cylindrical lens was used to illuminate a plane of 20×20 mm^2 and 20–100 μm thickness in the crystal. Three windows were polished on the crystals: two to allow the planar beam to pass the crystal, a third one perpendicular to the previous ones for observation of the scattered light. The scattered light distribution (scattering angle = 90 °) was recorded on a red sensitive photographic film.

2.3.3. Schlieren method

Gradients in optical density at the boundaries between adjacent growth sectors [10] were imaged by a similar Schlieren type optical set-up as described in ref. [11]. To prevent interference of the Schlieren image by surface defects, it was essential that the plane-parallel windows of the specimen crystals were polished very carefully.

3. Morphological aspects

3.1. Sphere growth experiments

A layer of 100–500 μm was grown on four BGO crystal spheres by immersion in a slightly supercooled melt. After separation from the melt they showed well developed {112} and {$\bar{1}\bar{1}\bar{2}$} faces, the sizes of which are nearly the same (fig. 2). No other faces could be detected. In the area between the faces bands [12], i.e. staircase shaped patterns composed of facets parallel to the two faces at the end points, can be seen. Bands are only formed between neighbouring {112} faces; no bands were found between adjacent {$\bar{1}\bar{1}\bar{2}$} faces and neighbouring {112} and {$\bar{1}\bar{1}\bar{2}$} faces (fig. 2b). The morphology of the grown spheres is in accordance with the non-centrosymmetric pointgroup of BGO, $\bar{4}3m$.

3.2. Morphology of small crystals

Small crystals grown from a slightly supercooled melt almost invariably show a tristetra-

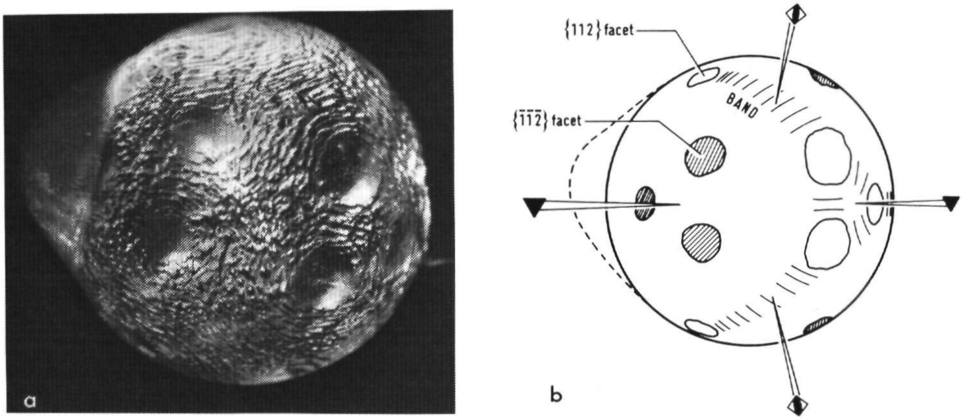

Fig. 2. Development of facets and growth bands on a single crystal sphere after immersion in a slightly undercooled melt: (a) view approximately along ⟨110⟩ direction; (b) schematic drawing.

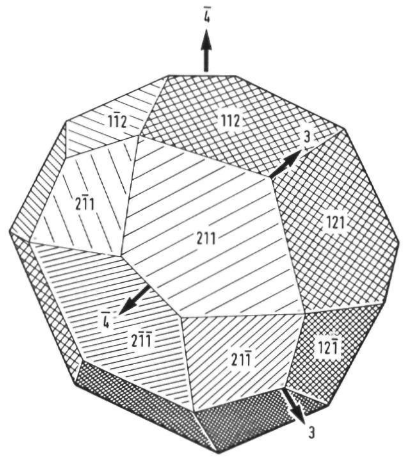

Fig. 3. Crystal habit of BGO formed under Bridgman growth conditions. The crystal is bounded by $\{112\}$ and $\{\bar{1}\bar{1}\bar{2}\}$ planes in agreement with the pointgroup $\bar{4}3m$ of $Bi_4(GeO_4)_3$. The larger $\{112\}$ faces grow slowest.

hedral [13] growth form. This means that only the $\{112\}$ facets determine the crystal morphology and the opposite – crystallographic non-equivalent – faces $(\bar{1}\bar{1}\bar{2}\}$ do not occur. Since a crystal is only bounded by the slower growing faces [3], this implies a difference in growth rate between $\{112\}$ and $\{\bar{1}\bar{1}\bar{2}\}$ faces. In the following the slow growing ("strong") faces are defined as $\{112\}$ and the faster growing ("weak") as $\{\bar{1}\bar{1}\bar{2}\}$.

As will be discussed in section 4, the Bridgman grown crystals are bounded by both $\{112\}$ and $\{\bar{1}\bar{1}\bar{2}\}$ faces. The morphology expected in the case of a slow growing $\{112\}$ and a faster growing $\{\bar{1}\bar{1}\bar{2}\}$ face in pointgroup $\bar{4}3m$ is a complex polyhedron as shown in fig. 3. It is clear that the $\{112\}$ faces are pentagonal and the $\{\bar{1}\bar{1}\bar{2}\}$ faces quadrangular. This distinction in shape will be helpful in differentiation between $\{112\}$ and $\{\bar{1}\bar{1}\bar{2}\}$ growth sectors in the Bridgman grown crystals.

3.3. Etching

Crystal slices polished parallel to $\{112\}/\{\bar{1}\bar{1}\bar{2}\}$, were etched in a diluted HCl solution. For the two plane-parallel surfaces of each slice, a different etch pattern was obtained: one face shows a well developed etch pit pattern (fig. 4a), the opposite face shows striations (fig. 4b). This once more confirms the non-equivalence of the $\{112\}$ and the $\{\bar{1}\bar{1}\bar{2}\}$ faces.

Knowing the growth direction of the crystal (section 4.1) from which the slices were sawn, the etch pit pattern could be identified as belonging to $\{112\}$, the opposite side to $\{\bar{1}\bar{1}\bar{2}\}$.

3.4. Surface morphology of as-grown surfaces

To get information about the growth mode of the BGO crystal surfaces, crystal plates parallel to $\{112\}$, slightly grown from the melt, were examined by optical microscopy. The as-grown $\{112\}$

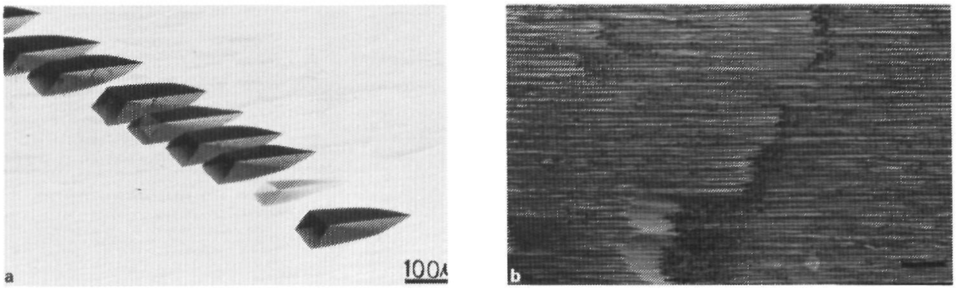

Fig. 4. The opposite $\{112\}$ and $\{\bar{1}\bar{1}\bar{2}\}$ crystal faces of BGO show different etching patterns after treatment with a solution of 10% HCl in H_2O: (a) $\{112\}$; (b) $\{\bar{1}\bar{1}\bar{2}\}$.

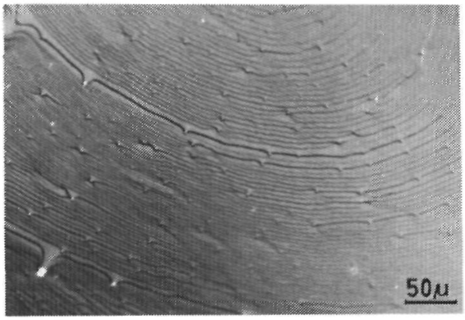

Fig. 5. Interference contrast micrograph of an as-grown $\{112\}$ BGO surface showing curved steps. Estimated stepheight is 300 Å.

and $\{\bar{1}\bar{1}\bar{2}\}$ faces were, aside from artifacts formed during separation of the plate from the melt, extremely flat (fig. 5). Only a few curved growth steps, with estimated step heights varying from 5 nm to 1 μm could be seen. No difference between $\{112\}$ and $\{\bar{1}\bar{1}\bar{2}\}$ was found.

From this surface morphology it can be concluded that the $\{112\}/\{\bar{1}\bar{1}\bar{2}\}$ faces grow via a step flow mechanism, i.e. are F-faces [14]. The observation that the step spacing is quite large (> 10 μm) indicates that the α-factor [15,16] is high, else narrowly spaced spiral hillocks or 2D nuclei would be observed. The conclusion that the $\{112\}/\{\bar{1}\bar{1}\bar{2}\}$ faces grow well below the roughening temperature [15,16] is confirmed by a related experiment in which it was shown that crystals growing at rates up to ~ 10 mm/s from a highly supercooled melt (900 °C) still exhibited planar faces. No kinetical roughening [17,18] occurred.

If one neglects the difference between step and surface energies then the α-factor increases for increasing interfacial energies [19]. Therefore the high α-values for the $\{112\}$ and $\{\bar{1}\bar{1}\bar{2}\}$ faces agree well with the conclusion made from earlier in-situ experiments [20] that for BGO a high interfacial energy exists between crystal and melt.

4. Optical characterization of the internal structure

4.1. Crystals grown by the vertical Bridgman method

The radially symmetric crystal boules (length/diameter ratio ≈ 7) were viewed both in a direction normal ("side-on") and parallel to the growth

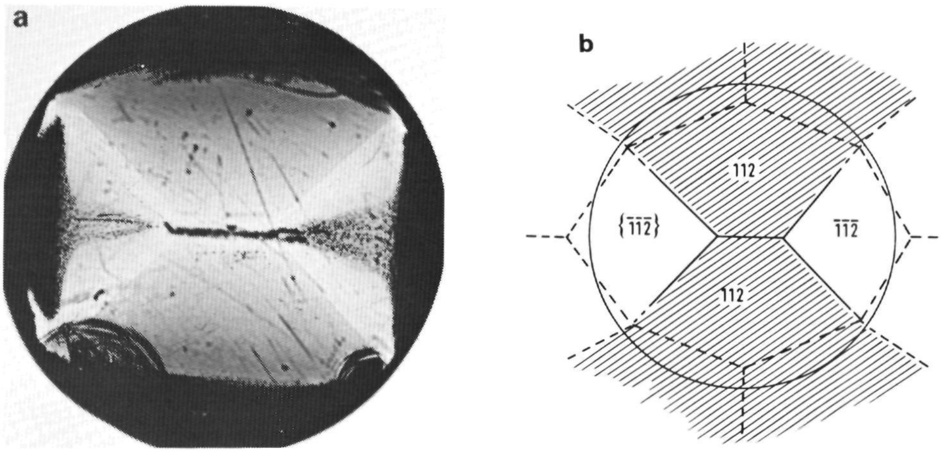

Fig. 6. (a) UV absorption topograph of a Bridgman (⟨100⟩) grown crystal viewed end-on. Adjacent $\{112\}/\{\bar{1}\bar{1}\bar{2}\}$ growth sectors with different absorption are visible. (b) Schematic drawing of (a) indicating the type of growth sectors. Crystal diameter 20 mm.

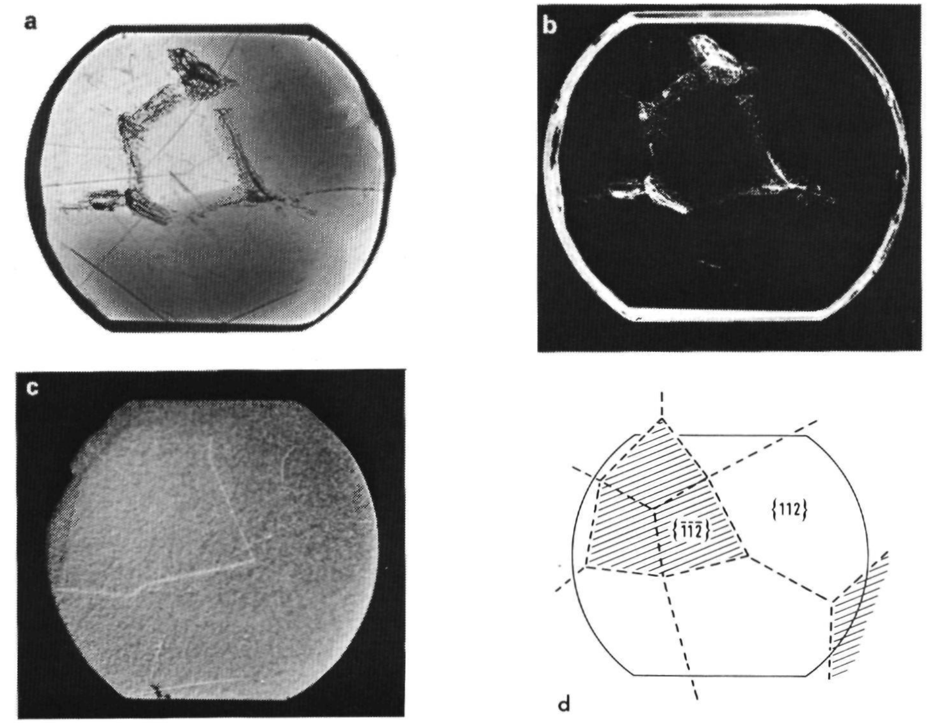

Fig. 7. Bridgman ($\langle\bar{1}\bar{1}\bar{2}\rangle$) grown crystal viewed end-on: (a) UV absorption topograph showing a higher segregation for the two darker {112} growth sectors compared to the three brighter $\{\bar{1}\bar{1}\bar{2}\}$ sectors; (b) inclusions delineating growth sectors, imaged by laser light scattering; (c) Schlieren picture revealing a difference in optical density between {112} and $\{\bar{1}\bar{1}\bar{2}\}$ growth sectors; (d) schematic drawing. Crystal diameter 34 mm.

direction ("end-on"). For the end-on examination slices (5–10 mm thickness) cut and polished perpendicular to the growth axis were used. For viewing side-on two opposite plan-parallel windows were polished along the length direction of the crystal boules.

4.1.1. Viewed end-on

Figs. 6 and 7a show UV absorption topographs of crystal slices cut from two crystal boules, which were grown along $\langle 100\rangle$ and $\langle\bar{1}\bar{1}\bar{2}\rangle$ respectively. Adjacent growth sectors [10] (i.e. crystal volumes the growth of which was gouverned by different growth faces) with different UV light absorption are clearly visible. To enhance the image contrast of the UV topographs, the crystals were preirradiated with UV light. Near the end of the crystal rods and for lower quality crystals the sector boundaries are delineated by inclusions, which can be visualised by light scattering (fig. 7).

From shape, known pointgroup symmetry and using X-ray diffraction, the growth sectors were found to correspond with {112} and $\{\bar{1}\bar{1}\bar{2}\}$ faces. No evidence was found for sectors related to other faces. This means that also the large Bridgman crystals show facetted growth via {112} and $\{\bar{1}\bar{1}\bar{2}\}$ faces. The larger sectors, which are pentangular in shape (compare fig. 7 with fig. 3) correspond with the slow growing {112} faces. These sectors always show the increased UV absorption. The smaller quadrangular sectors are related to the faster growing $\{\bar{1}\bar{1}\bar{2}\}$ faces and show the lower UV absorption.

For crystals grown along ⟨112⟩, $\langle\bar{1}\bar{1}\bar{2}\rangle$ or other directions careful observation of the growth sectors combined with Laue X-ray diffraction demonstrated the occurrence of a convex front [21], which must have been introduced by a convex melt isotherm. From this the polarity [5,22] of the $\{112\}/\{\bar{1}\bar{1}\bar{2}\}$ faces could be established, which again allowed the assignment of the etch patterns.

The conclusion drawn from the absorption topographs that the "strong" {112} faces exhibit more UV light absorption than the "weak" $\{\bar{1}\bar{1}\bar{2}\}$ faces is confirmed by taking UV-VIS absorption spectra from both sector types within one crystal as shown in fig. 1. The increased UV absorption in the {112} sectors points to a higher degree of impurity, vacancy, or other defect segregation as compared to the adjacent $\{\bar{1}\bar{1}\bar{2}\}$ sectors. This indicates that the defect segregation is gouverned by surface kinetics rather than the equilibrium distribution coefficient. In the latter case no difference should exist between both sectors. Such a defect incorporation determined by growth kinetics is not unusual for facetted growth [23,24] and might be explained by a difference in impurity adsorption on different growth faces, similar to the case of {100} and {101} KDP [25,26].

In figs. 6 and 7a, it can be seen that the UV absorption gradually increases upon going from the periphery towards the middle of the "strong" {112} growth sectors. This points to an increased defect incorporation at the central parts of the {112} facets during crystal growth. A possible explanation might be given as follows: in the case of facetted growth along a convex curved freezing isotherm, the central parts of the planar faces are exposed to the largest supersaturation [27]. This implies that here the step velocity and the step spacing are maximal. Since rapidly advancing steps capture impurities or create defects more easily, the segregation is maximal at the central facet region.

Figs. 7c and 8 show Schlieren images of slices cut from crystal rods grown in the $\langle\bar{1}\bar{1}\bar{2}\rangle$ and $\langle\bar{1}\bar{1}\bar{1}\rangle$ directions respectively. At the borderline of {112} and $\{\bar{1}\bar{1}\bar{2}\}$ growth sectors a sharp change in optical density can be noticed. From the image contrast it was deduced that the "weak" $\{\bar{1}\bar{1}\bar{2}\}$ sectors have the highest index of refraction. Between crystal volumes belonging to adjacent {112}

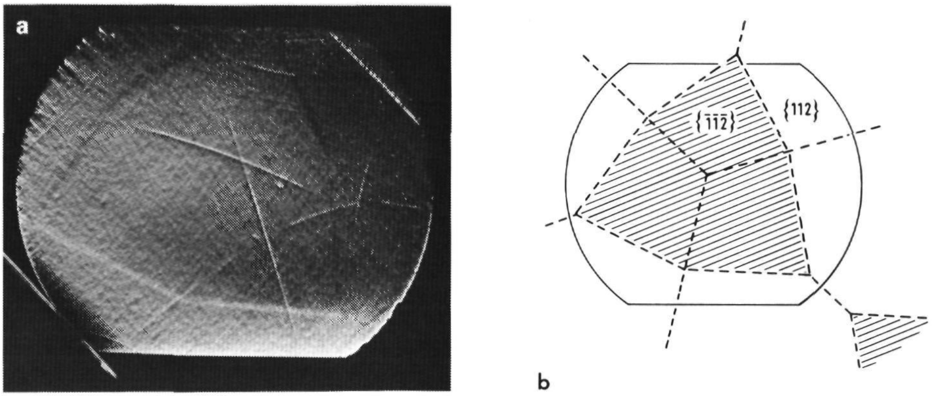

Fig. 8. (a) Schlieren image of a Bridgman ($\langle\bar{1}\bar{1}\bar{1}\rangle$) grown crystal. Despite the fact that in this specimen no detectable amount of UV–blue absorbing colour centres was found, still a difference in optical density was present between the {112} and $\{\bar{1}\bar{1}\bar{2}\}$ growth sectors. (b) schematic drawing of (a). Crystal diameter 34 mm.

or adjacent $\{\bar{1}\bar{1}\bar{2}\}$ sectors no difference in refractivity was found.

The difference in optical density is not coupled with a difference in yellowish colouring or UV absorption: the crystal of fig. 8 was a perfectly clear crystal, with no spatial variation in UV transmission. This indicates that the difference in optical density is introduced by another defect then the UV-light absorbing "colour" centres.

4.1.2. Viewed side-on

Time dependent variations in growth conditions introduce variations in absorption of impurities and other defects in the crystal. This leads to striations and growth banding as revealed by the UV absorption topographs of crystal rods, viewed side-on, in fig. 9. In the ⟨110⟩ grown crystal (fig. 9a) the facetted nature of the solidification front is clearly visible. Further examination of the growth band patterns in this crystal showed that, during growth the overall shape of the solid–liquid interface and thus the freezing isotherm was convex to the melt. For a crystal boule grown in the "strong" ⟨112⟩ direction, the solidification front was almost planar as can be concluded from the striation patterns in fig. 9b.

For all the investigated crystals never a concave solidification front was observed. The most dominant factor that determines the morphology of the solid-liquid interface is the crystallographic growth direction. Since the distribution of both the inclusions and the segregation in radial direction are directly related to this morphology, the crystallography seems to be a factor of major importance for the quality of the crystals.

Aside from the volume near the seed end, for most crystal rods no essential change in averaged UV–blue absorption could be observed along the growth direction. Optical measurement of one boule (length 250 mm) showed no essential violet ($\lambda = 400$ nm) absorption near its lower end; near the middle and the top end the optical absorption per unit length was equivalent within a few percent. This indicates that aside from an initial transient at the beginning of growth the effective segregation coefficient of the yellowish colouring defects is about 1. This points to a diffusion controlled segregation mechanism as described by Smith et al. [28]. The final transient as discussed by these authors, manifests as a small volume of high inclusion density at the outer end of the crystals, due to the separation of a second phase.

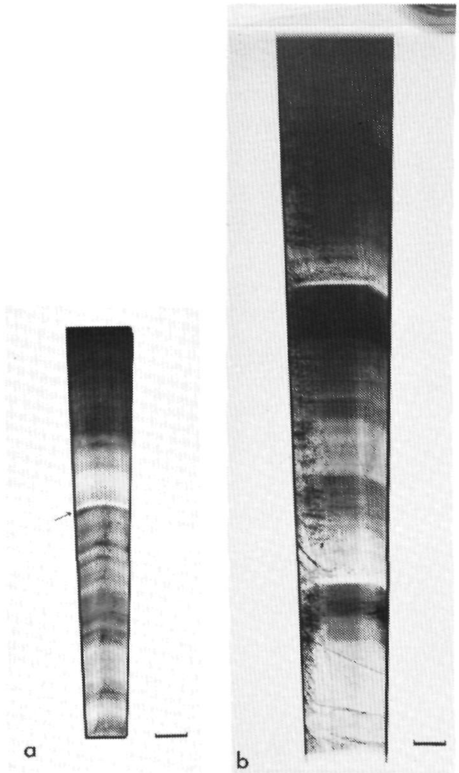

Fig. 9. UV absorption topographs of Bridgman grown crystals viewed side-on, revealing facetted growth: (a) ⟨110⟩ grown crystal; note the accidental remelting near the arrow; (b) ⟨112⟩ grown crystal. The dark areas correspond with an increased impurity content. Bright side crystallized first; scale bar represents 10 mm.

Deviation from stoichiometry also affects the optical properties: an excess of 0.2 mol% Bi_2O_3 introduces an increase is UV and blue absorption, which can be recognized as an increased yellowish colouring of especially the "strong" {112} growth sectors.

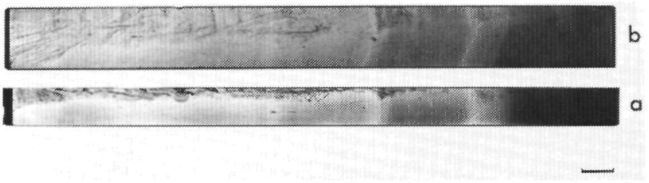

Fig. 10. Crystals grown by the horizontal Bridgman technique, viewed side-on by UV absorption topography: (a) side view: (b) as (a) after rotating the crystal 90 ° along its length axis. Bright side crystallized first, scale bar represents 10 mm.

4.2. Crystals grown by the horizontal Bridgman method

The UV absorption topographs of crystals grown in a horizontal Bridgman furnace (fig. 10) show the same general features as vertically grown crystals. The growth band patterns of these crystals again point to a facetted (parallel to $\{112\}$ or $\{\bar{1}\bar{1}\bar{2}\}$ interface, convex towards the melt.

In contrast to the vertical Bridgman technique however, the horizontal method is characterized by a lack of radial symmetry along the crystal axis. Furthermore the horizontal temperature gradient normal to the vertical gravitation field introduces convection [29], which might be substantial because of the melt's low viscosity [30]. In related in-situ experiments [20] convection of BGO melt was indeed observed. This asymmetry and convection influences the growth band pattern and the inclusion distribution in the crystals to a large extent. For instance, inclusions are preferentially formed at the earlier stages of growth in the upper growth sectors. The morphology of the solid–melt interface as derived from the growth band patterns changes considerably during crystal growth. Finally the crystals were less uniform in impurity segregation due to convective mixing. In general, horizontally grown crystals were of lower quality than the vertically grown ones.

4.3. Crystal grown by the Czochralsky method

One – older – Czochralsky grown crystal, purchased from Harshaw Co. was examined by the optical methods described above. Fig. 11a shows an UV absorption topograph and fig. 11b

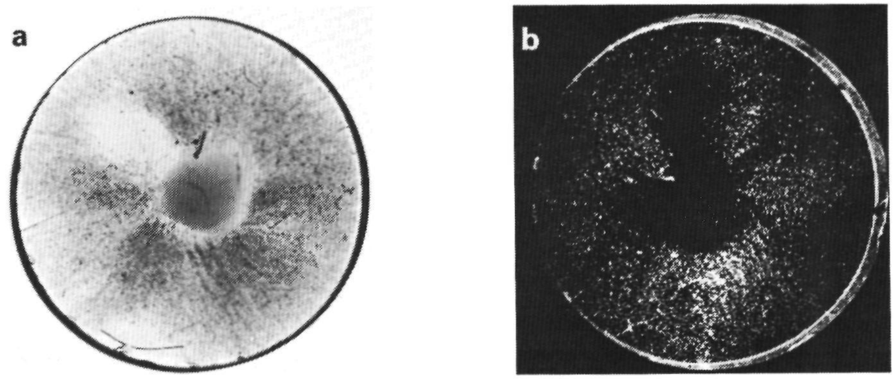

Fig. 11. Czochralsky grown crystal viewed end-on: (a) UV absorption topograph showing enhanced absorption at the core region; (b) laser light scattering image showing the distribution of inclusions. Diameter 25 mm.

the distribution of inclusions imaged by light scattering in a crystal slice viewed end-on. It is obvious that the crystal core shows a higher "colour centre" concentration but contains considerably less inclusions than the periphery Probably during crystal growth the core was facetted and the outer regions were more or less toothed.

5. Conclusions

The distribution of defects in Bridgman grown $Bi_4(GeO_4)_3$ crystals was imaged by means of UV absorption topography, laser light scattering and Schlieren techniques. To facilitate interpretation in addition sphere growth experiments and in-situ surface microtopography of as-grown surfaces were carried out.

Some important conclusions that could be drawn from the present study are.

(i) BGO crystals growing from the melt are always bounded by $\{112\}$ and $\{\bar{1}\bar{1}\bar{2}\}$ crystallographic facets, even at very high growth rates.

(ii) The $\{112\}$ and $\{\bar{1}\bar{1}\bar{2}\}$ faces of BGO can be classified as very strong F-faces, with a high α-factor and thus probably a high solid–liquid interfacial energy.

(iii) The opposite $\{112\}$ and $\{\bar{1}\bar{1}\bar{2}\}$ faces, which are crystallographically non-equivalent were arbitrarely denoted as $\{112\}$ for the slower growing and $\{\bar{1}\bar{1}\bar{2}\}$ for the faster growing face A difference in surface morphology of both faces after chemical etching was helpful for identification.

(iv) The impurity and off-stoichiometry segregation in the crystals is gouverned by kinetics, as was concluded from a lower (blue UV light absorbing) defect concentration in the $\{\bar{1}\bar{1}\bar{2}\}$ sectors compared to the $\{112\}$ sectors. The difference is especially notable in crystals grown from a Bi_2O_3 rich melt.

(v) The formation of inclusions is concentrated at the edges of the growth facets; impurity segregation is maximal near the centre of the facets.

Acknowledgements

The authors are indebted to professor P. Bennema, Professor R.T. Van de Walle and Drs. M. Raaymakers for their interest in the present work. Further they are grateful to J.J.H. Thönig, W.H. van der Linden and C. Brouwer for growing the crystals and to E.C. Antheunis for cutting and polishing the crystals. They wish to acknowledge the financial support of the Foundation for Technical Sciences (STW).

References

[1] F Lorenz, Recent Progress in Development for High Resolution Calorimetry (Max Planck Institute Report MPI-PAE/Exp EL 129, 1984)

[2] P Lecoq et al, Europhys News 8 (1985)

[3] A Horowitz and G Kramer, J Crystal Growth 78 (1986) 121

[4] B Honigmann, Gleichgewichts- und Wachstumsformen von Kristallen (Steinkopff, Darmstadt, 1958)

[5] R Cadoret, Thesis, University of Caen (1965)

[6] See, for instance, B Cockayne, J Crystal Growth 42 (1977) 413

[7] K Takagi, T Oi, T Fukazawa, M Ishii and S Akiyama, J Crystal Growth 52 (1981) 584

[8] R Voszka, G Gévay, I Foldvari and S Keszthelyi-Landori, Acta Phys Acad Sci Hung 53 (1982) 7.

[9] G S Woods and A R Lang, J Crystal Growth 28 (1975) 215

[10] H Klapper in Characterization of Crystal Growth Defects by X-Ray Methods, NATO Advanced Studies Institute Series, Ser B, Physics, Vol 63, Eds B K Tanner and D K Bowen (Plenum, New York, 1983) p 133

[11] W J P van Enckevort and M Matuchova, Crystal Res Technol 22 (1987) 167

[12] P Bennema, Z Krist 121 (1965) 312

[13] M J Buerger, Elementary Crystallography (Wiley, New York, 1963) pp 161, 166

[14] P Hartman, in Crystal Growth An Introduction, Ed P Hartman (North-Holland, Amsterdam, 1973) p 367

[15] I A M J Jetten, H J Human, P Bennema and J P van der Eerden, J Crystal Growth 68 (1984) 503

[16] J P van der Eerden, P Bennema and T A. Cherepanova, Progr Crystal Growth Characterization 1 (1978) 219

[17] M Elwenspoek, Appl Phys A41 (1986) 123.

[18] H J Human, J P van der Eerden, L A M J Jetten and J G M Odekerken, J Crystal Growth 51 (1981) 589

[19] P Bennema and J P van der Eerden, in Morphology of Crystals, Vol A, Ed I Sunagawa (Reidel, Dordrecht, 1987)

[20] W J P van Enckevort and F M Smet, J Crystal Growth 82 (1987) 678

[21] C E Chang and W R Wilcox, J Crystal Growth 21 (1974) 135

[22] H Binsma, W J P van Enckevort and G W M Staarink, J Crystal Growth 61 (1983) 147.

[23] D T J Hurle and B Cockayne, in Characterization of Crystal Growth Defects by X-Ray Methods, NATO Advanced Studies Institute Series, Ser B, Physics, Vol 63, Eds B K Tanner and D K Bowen (Plenum, New York, 1983) p 53

[24] A A Chernov, Modern Crystallography III Crystal Growth, Springer Series in Solid State Sciences, Vol 36 (Springer, Berlin, 1984) p 190

[25] H Jaffe and R F Kjellgren, Disc Faraday Soc 5 (1949) 319

[26] B Dam, P Bennema and W J P van Enckevort, J Crystal Growth 74 (1986) 118

[27] A A Chernov, Modern Crystallography III Crystal Growth, Springer Series in Solid State Sciences, Vol 36 (Springer, Berlin, 1984) p 229

[28] V G Smith, W A Tiller and J W Rutter, Can J Phys 33 (1955) 723

[29] J R Carruthers, J Crystal Growth 2 (1968) 1

[30] Yu F Kargin et al, Izv Akad Nauk SSSR, Neorgan Mater 13 (1977) 135

CHARACTERIZATION STUDY OF LARGE SIZED CZOCHRALSKI GROWN BISMUTH GERMANATE CRYSTALS

F. Smet and R.C. de Boer

Dept. of Solid State Chemistry, Dept. of High Energy Physics,
Faculty of Science, University of Nijmegen
Toernooiveld, 6525 ED, Nijmegen

and
W.J.P. van Enckevort

Drukker International B.V.
Beversestraat 20 5431SH Cuijk, The Netherlands

Abstract

Large Czochralski grown $Bi_4Ge_3O_{12}$ *(BGO) crystals were characterized using optical methods. The results are discussed in relation to the interface morphology and the specific conditions during growth. A comparison is made with crystals grown by the vertical Bridgman method. It was found that in Czochralski growth conditions, growth proceeds along an unfacetted curved interface. The main differences in crystal properties due to the two growth methods appear to be: (i) the coarse of the impurity segregation during growth; (ii) the spatial distribution of bubbles and inclusions; (iii) the dislocation density in the crystals.*

1. Introduction

Bismuth germanate ($Bi_4(GeO_4)_3$, BGO) is a synthetic crystalline material with interesting electro-optical, electromechanical and luminescence properties [1]. It received considerable attention, because of its attractive scintillation properties upon interaction with ionizing radiation [2]. Large single crystals of BGO have now found wide application as scintillation crystals in the fields of nuclear medicine, industry and high energy physics.

The single crystals needed for the above mentioned applications are succesfully grown from the melt, generally by Bridgman or Czochralski methods. To allow for the production of larger sized BGO crystals of high perfection however, a better understanding of the fundamental growth processes is required. To this end a number of studies have been carried out, concerning crystal morphology [3], growth behaviour at a microscopic scale [4] and defect structure [5,6].

Recently [5] the inhomogeneous distribution of point defects in large Bridgman grown crystals has been investigated in detail. In this study several optical characterization methods were used to image the spatial distribution of the defects: U.V. absorption topography, laser light scattering, and the Schlieren technique. The distribution of point defects was found to be directly related to the morphology of the facetted solid-liquid interface during crystal growth. During the present investigation, instead of Bridgman grown crystals, BGO crystals, grown by the Czochralski method were examined using similar techniques. Since for one crystal the same starting materials were used as for the Bridgman grown crystals described in [5], this offers an unique possibility of making a direct comparison of BGO specimen grown by the two growth methods.

2. Experimental

2.1 Crystal growth

The investigated crystals were grown in a diameter controlled Czochralski growth system, which was open to the air. Typical growth parameters are: growth rate 4.5 mm/h , rotation rate 32 rmp, diameter 55 mm, remaining melt 30%. Growth was terminated a by quick withdrawal of the boule from the melt, leaving the solid-liquid interface as undisturbed as possible. Crystals were annealed by keeping them at 1000 °C for several hours, followed by slow cooling.

A stoichiometric mixture of high purity Bi_2O_3 and GeO_2 powders was used as starting material.

One crystal was grown from a polycrystalline BGO-powder with increased impurity content (from here on refered to as the H43 crystal), from which previously [5] crystals were grown by the Bridgman method. This provided a useful reference in the interpretation of the growth phenomena and allowed us to distinguish impurity specific effects.

2.2 Methods of investigation

The crystallographic orientation of the crystals was determined by Laue X-ray diffraction. When neccesary some parts of a crystal were etched (10% HCl in H_2O) to distinguish between the polar directions, following the procedure described in [5].

At apropriate places, parallel and perpendicular to the growth direction, windows were cut and careful polished prior to examination of the interior of the crystals.
Optical methods were used to investigate the presence and distribution of the typical point defects which occur in BGO single crystals: i) U.V. topography for imaging small differences in impurity- or off-stoichiometry segregation; ii) Laser light scattering for inclusions; iii) Mechanical stress fields cause local optical anisotropy in the crystals. They were chracterized by birefringence topography [7,8]

3. Exterior of as-grown crystals

Visual inspection of the exterior of the crystals reveals some interesting features. The external shape is approximately cylindrical. At the top of the crystals (first grown part) the perimeter is circular; going down, flat parts appear on the perimeter at specific points until at the bottom (last grown part) it is completely flattened (see fig. 4a). The lower halve thus exhibbits more or less plane sides parallel to the growth axis. Under unfavourable growth conditions even 'wings' could develop from these flat sides as is shown in ref. [6] p. 298.

On the plane and cylindrical parts of the boules periodic ripples are present (typical dimensions: radius variation 1 mm, periodicity in direction of growth axis 5 mm) which are caused by the adjustments of the diameter control system. It was noticed that although the periodicity was the same on all parts of the boule, the exact profile on the plane parts (local radius as a function of the time) between two maxima or two minima was quite different. This means that each flat side has his own profile. We found that the location and orientation of these flat sides obey the crystallographic point group symmetry. For instance, on a <111>

grown crystal three different sides are present which are each repeated over an angle of 120°, thus reflecting the three fold rotation axis parallel to the growth axis.

This indicates that the contact angle (between the crystal and the melt during growth) is dependent on the crystallographic orientation, especially at the lower end of the boules where the temperature gradient is less. Probably a relation can be found between the growth habit of BGO (i.e. the crystal faces which are not roughened at the growth temperature, {112} and $\{\bar{1}\bar{1}\bar{2}\}$, [5]) and the orientation of the sides of the Czochralski grown boules [9].

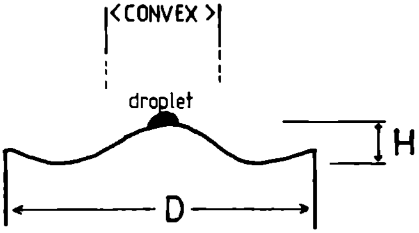

Fig. 1 Schematic representation of the interface shape of Czochralski grown BGO crystals. The convex part is marked C, its height is marked H.

The bottom of the crystals show the solid-liquid interface shape at the last stage of growth. From the observation of seven crystals with equal diameter, various lengths (6 - 14 cm) and various crystallographic orientations, the typical shape of the interface is depicted in fig. 1. This shape, which is also the shape of the melt isotherm, is determined by the total of heat flows in the crystal (conductive and radiative) and in the melt.

The heat flow in the melt is dictated by the flow pattern of the forced flow caused by the (moderate) crystal rotation which was used. In our case the expected flow pattern is one single flow cell in which the liquid is axially spiralling towards the interface [10,11]. The resultant diffusion layer, and impurity segregation, accompagning such a fluid flow pattern is expected to be largely constant along a flat interface [11,12].

As can be seen in fig. 1 the interfaces have a central part which is convex to the melt, while the surrounding perifery is concave in one dimension. The heigth/diameter ratio H/D of the crystals varied between 0.027 and 0.164 (due to differences in rotation rate, optical transmission of the crystals and lengths of the crystals). It is interesting that the proportion of the convex region on the interfaces with different H/D ratio was almost constant: 18 to 23% of the diameter. As will be discussed in section 4.1 an increased impurity segregation might be associated with this convex region.

Microscopic examination showed that the interfaces have a smooth surface with no bunches or other signs of layered growth.

Occasionally a smal facet is visible in the convex region. Details below 1 µm are however obscured by the adhering liquid layer which is crystallized after withdrawal from the melt.

One crystal with increased impurity content (the H43 crystal) exhibbited areas with periodic ripples (fig. 4a). The rotation direction is clearly visible; probably the direction of the ripples corresponds to the mean trajectory of the liquid flow along the interface during growth. The top edges of the ripples are straight and seem to have preferential directions. This indicates that the morphology is also partly determined by the crystallographic orientation. Probably it can be related to the growth habit of BGO [9]. From the observations in section 4.2 it is clear that this morphology is caused by constitutional supercooling, in the last stage of growth. Furthermore it apparently remained unchanged for at least three hours.

4. Optical characterization of the interior

The crystal boules were examined in a direction normal ('side-on') and parallel to the growth direction ('end-on'). For this purpose planparallel windows were cut and polished at the necessary locations on the boules.

4.1 U.V. topography

Figure 2a shows an U.V. topograph of the H43 crystal which was grown along a direction near $<\bar{1}\bar{1}\bar{4}>$. Striations caused by small variations (in time) in the growth conditions are visible. Exept for the first grown section (which had a low rotation rate) the interface shape appears to vary little during growth. The overall convexity is slowly decreasing towards the end. A convex central part and a concave periphery can be distinguished at the interface, as was also observed in section 3.

Throughout the whole crystal, a central area with increased absorption (core) is present. It can be seen in fig. 2a that this area was grown along the convex part of the interface. The discontinuous transition between this higher segregated area and the lower segregated area does suggest that a different incorporation mechanism is active along the convex and the concave parts of the interface. In connection to this, it is interesting that in a low temperature gradient a convex area is usually totally facetted [5] while in a concave area this is not the case due to the nucleation by reentrant corners [13].

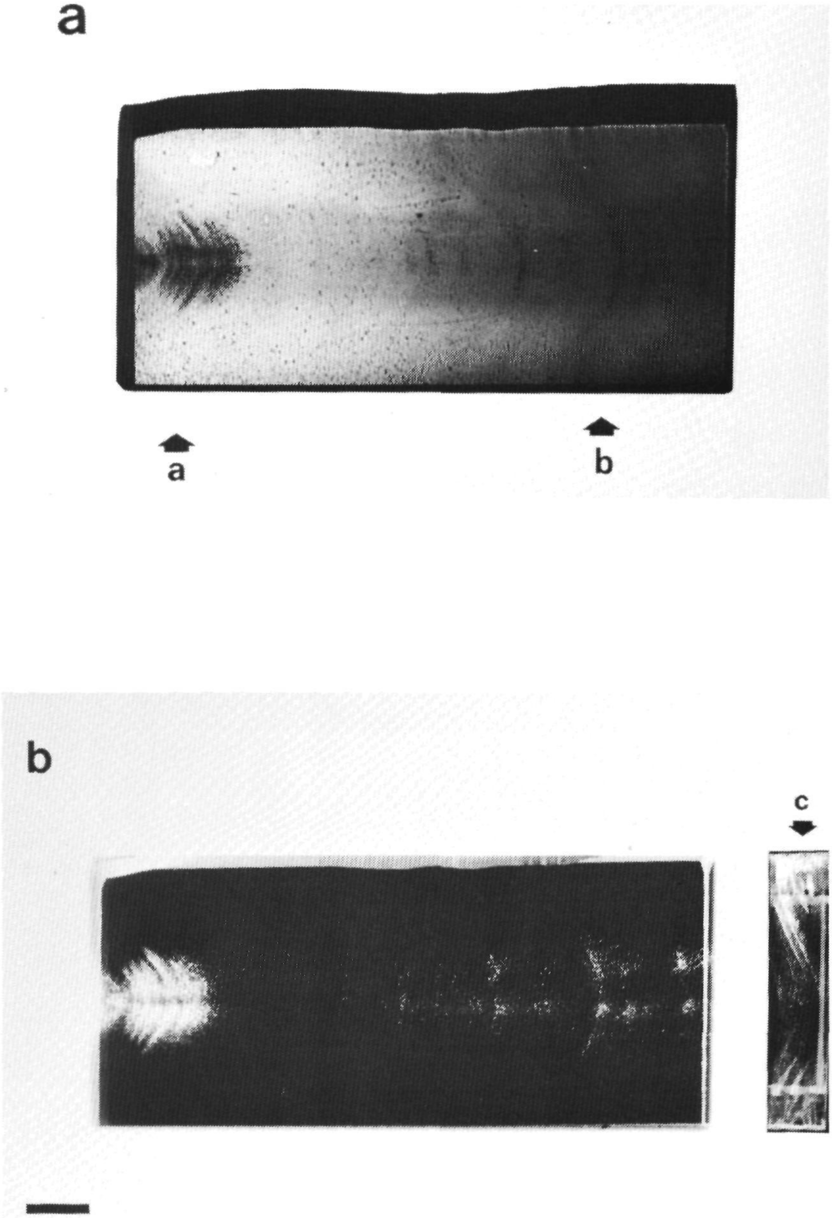

Fig. 2 BGO crystal grown along <$\bar{1}\bar{1}\bar{4}$> by the Czochralski method, viewed side-on: (a) U.V. absorption topograph revealing the solid-liquid interface shape during growth; (b) light scattering image of the same crystal showing the distribution of bubbles and inclusions. Bar indicates 1 cm.

In all areas the absorption increases gradually, going from the start to the end of the crystal. This indicates that the impurities which cause the absorption accumulate in the melt and that the effective segregation coefficient is smaller than unity.
This is in agreement with the condition of a well mixed melt. In the Bridgman growth of BGO [5] a segregation coefficient of about one was found due to a stagnant melt.

4.2 Laser scattering

In figure 2b inclusions (bubbles) are imaged by light scattering. A thin layer in the crystal (0.5 mm) normal to the direction of view was illuminated by a planar laser beam. A comparison with figure 2a shows that the inclusions occur during fluctuations in the growth rate, where also an increased segregation is present in the crystal. During such fluctuations, they occur primarily in the center, spreading out along the interface at larger fluctuations, regulary distributed in radial direction. In crystals with low impurity content equal behaviour was found.

The irregular growth in the initial stage (in the H43 crystal) caused many inclusions. Figure 3a shows the radial distribution in a thin section of the crystal perpendicular to the growth axis (at **a** in fig. 2b). A pattern of approximately circular, bubble free areas is clearly visible. During growth, {112} and $\{\bar{1}\bar{1}\bar{2}\}$ facets were present at these locations on the interface. This was verified by comparing the shape and location of the areas with the crystallographical orientation of the crystal, the local curvature, and the growth habit of BGO [5]. As can be seen in figure 2b, the facet area nearest to the center is extending throughout the crystal. From the size of the facet and the local curvature of the interface the facet lag is calculated to be 0.078 mm (**b** in fig. 2b). If the temperature gradient at the interface is estimated 100 °C/cm, then the extra undercooling for facetted growth (in comparison with the off-facet regions) measures 0.78 °C, at the present growth rate of 4.7 mm/hr [14].

The last part of the H43 crystal was grown from a more and more impurity enriched melt and contains a considerable amount of inclusions (**c** in fig. 2b). These are not pure bubble type inclusions (although the shape is similar), but partly filled with a brownish coloured phase. In figure 4b the spatial distribution in radial direction is shown, imaged by laser light scattering. The inclusions appear to be lined up periodically in a spiral pattern. This pattern matches precisely the rippled morphology of the interface visible at the crystal bottom, as described in section 3 (fig. 4a). From this it is clear that the interface is of the cellular type and that these inclusions are formed by constitutional supercooling.

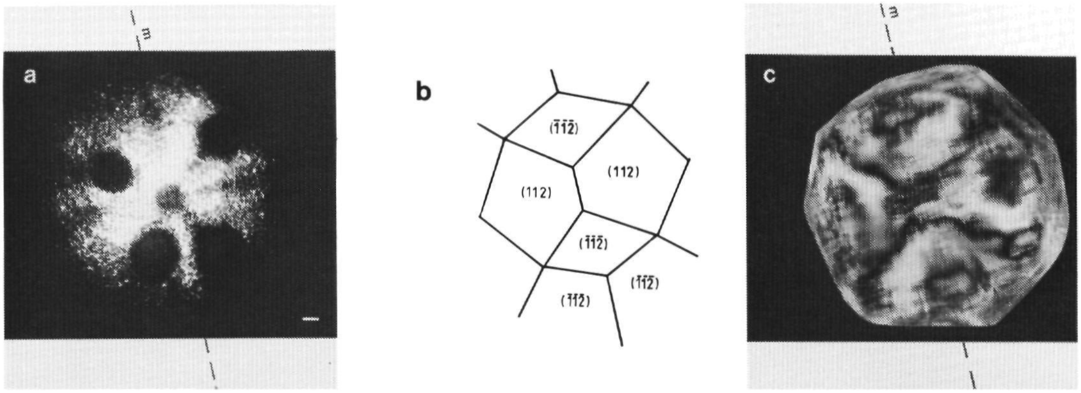
m
a
b
$(\bar{1}\bar{1}\bar{2})$
(112)
(112)
$(\bar{1}\bar{1}\bar{2})$
$(\bar{1}\bar{1}\bar{2})$
$(\bar{1}\bar{1}\bar{2})$
m
c
m
m

Fig. 3 Czochralski grown crystal (H43) viewed end on: (a) light scattering image. A thin section perpendicular to the growth axis (position a in fig. 2a) was illuminated by laser light. Bar indicates 1 mm. (b) Schematic drawing of the growth habit of BGO [5] in the same crystallograpical orientation, outlining the positions of the $\{112\}$ *and* $\{\bar{1}\bar{1}\bar{2}\}$ *facets. The crystallographic mirror plane parallel to the growth axis is marked m. (c) Stress birefringence image showing the distribution of stress fields.*

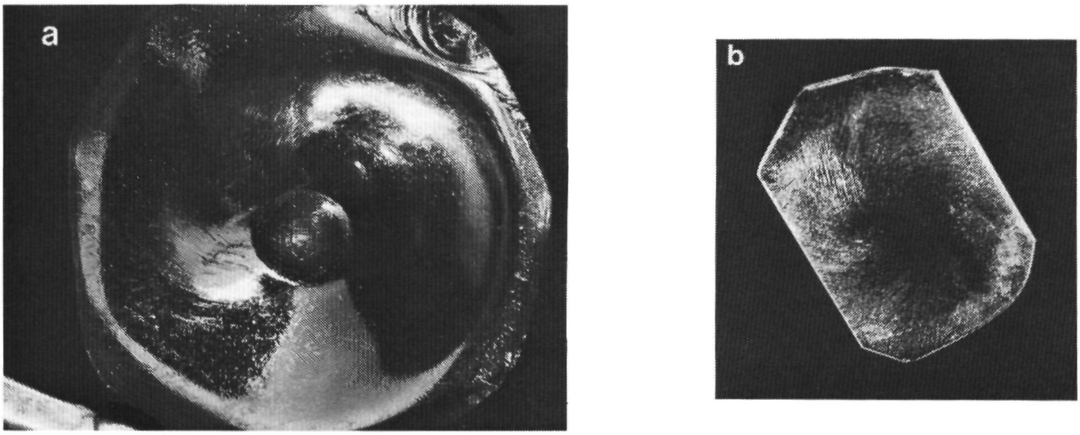

Fig. 4 The H43 crystal viewed end-on: (a) Surface morphology of the last grown part showing periodic ripples in a spiral pattern; (b) light scattering image of the crystal section below the interface (position c in fig. 2b) showing the corresponding distribution of inclusions.

Apparently the brownish phase is captured simultaneously with the gas at the interface. A similar observation was reported by Horowitz et.al. [6]. The morphology of the interface in figure 4a is thus representative for the solid-liquid interface during growth. The inclusion pattern in the crystal and therefore the interface morphology remained unchanged after its first appearance, i.e. the last three hours of growth.

4.3 Stress birefringence topography

Mechanical stress fields which remained in the crystals after annealing were investigated by birefringence topography. In fig. 4c the distribution of the stress fields in radial direction is shown, in the H43 crystal. In the patterns the symmetry of the mirror plane is visible which is parallel to the growth axis and perpendicular to $[1\bar{1}0]$. The crystals were highly strained in comparison to Bridgman grown crystals [5].

A slice, near the end and perpendicular to the growth axis of the H43 crystal, was examined by birefringence microscopy. In the slice three different areas could be distiguished. The central part contained a cloud of small inclusions (bubbles). In this part many irregulary curved dislocation lines were present. These were probably generated during the cooling period after growth, due to plastic deformation. In Bridgman grown crystals they also occur [8]. In regions around the central part, bundles of straight dislocation lines were found. The direction of the (edge) dislocations was approximately perpendicular to the interface. Probably they were

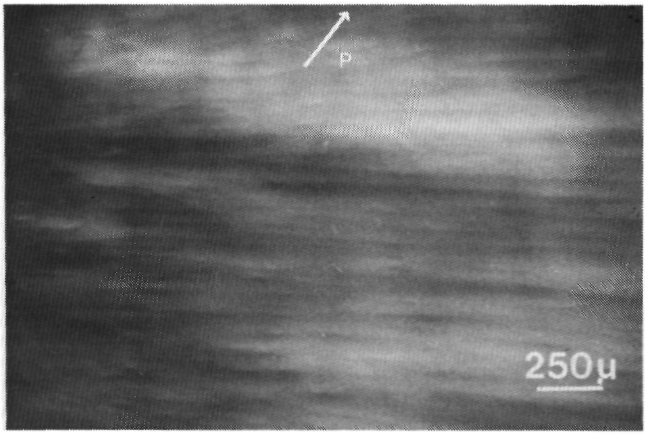

Fig. 5 Microscopic birefringence image of dislocation structure in the area of grown-in dislocations.

formed during growth as a result of the large radial temperature gradient which accompagnies the curved solid-liquid interface [11,15]. At the perifery of the slice many low angle grain boundaries were visible, parallel to the growth axis. They probably result from the relief of stress during the annealing procedure.

5. Discussion and conclusions

In the investigated crystals growth proceeds along an unfacetted, curved solid-liquid interface. This is in contrast to Bridgman grown crystals which were reported to grow totally facetted [5]. This difference in interface morphology can be explained by the much larger temperature gradient at the interface which is inherent in the Czochralski growth method. Along a convex interface a high temperature gradient geometrically limits the dimensions of facets [16]. The optical absorption in radial direction is largely homogeneous, without the growth sectors which occur in Bridgman grown crystals.

As was mentioned in sect. 4.1 , the optical absorption in axial direction increases towards the end, in accordance with the conditions of a well stirred melt, while in Bridgman grown crystals it was almost constant due to a stagnant melt. In the H43 crystal, which was grown from the same starting material as the Bridgman crystals, also the same coloration was found. This means that the impurity incorporated in the crystals by the two growth methods (facetted and unfacetted) causes the same type of light absorbing point defects. Crystals, grown from another starting material could be grown completely transparent. This indicates that also in Czochralski growth of BGO the purity of the starting material is of major importance.

As was described in sect. 4.2 bubbles primarily occur in the center of the crystals. In Bridgman grown crystals they were concentrated at the facet edges and were generally larger.

The dislocation density in the Czochralski grown crystals is very high compared to the Bridgman grown crystals which could be grown almost dislocation free.

From the observations in sect. 3 and 4 it is clear that the crystallographic orientation partly determines the external shape of the boules, the distribution of the inclusions and the distribution of the stress fields in the crystals. Since it does not determine the interface morphology it is concluded that in Czochralski growth the crystallograpic orientation is of less importance than in the Bridgman growth method.

Summarizing , it can be said that the main differences between crystals grown by the two methods are: (i) the coarse of the impurity segregation during growth; (ii) the spatial distribution of bubbles and inclusions; (iii) the dislocation density in the crystals.

Acknowledgements

The authors are indebted to Prof. Dr. P. Bennema and Prof. Dr. R.T. van de Walle for their interest in the present work. Furthermore they are grateful to H. Meeldijk and J. Jappes for growing the crystals and to E.C. Antheunis for cutting and polishing the crystals. F. Smet wishes to acknowledge the support of the Foundation of Technical Sciences (STW). R.C. de Boer acknowledges the support of Engelhard De Meern B.V.

REFERENCES

[1] K. Takagi, T. Oi, T. Fukazawa, M, Ishii and S. Akiyama, J. Crystal Growth 52 (1981) 584.
[2] International Workshop on Bismuth Germanate, Princeton University, Dept. of Physics, November 1982.
[3] F. Smet, P. Bennema, J.P. van der Eerden and W.J.P. van Enckevort, J. Crystal Growth, accepted.
[4] W.J.P. van Enckevort and F. Smet, J. Crystal Growth 82 (1987) 678.
[5] F. Smet and W.J.P. van Enckevort, J. Crystal Growth 88 (1988) 169.
[6] A. Horowitz and G. Kramer, J. Crystal Growth 79 (1986) 296.
[7] R. Bullough, Phys. Rev. 110 (1958) 620.
[8] W.J.P van Enckevort and F. Smet, J. Crystal Growth, to be published.
[9] F. Smet, R. de Boer and Y. Liao , work in progress.
[10] J.R. Carruthers and K. Nassau, J. Appl. Phys. 39 (1968) 5205.
[11] J.C. Brice, The Growth of Crystals from Liquids, Selected Topics in Solid State Physics, Vol. XII (North Holland, Amsterdam, 1973) p.134.
[12] J.R. Carruthers and A.F. Witt in: Crystal Growth and Characterization, Eds. R. Ueda and J.B. Mullin (North Holland, Amsterdam, 1975) p.109.
[13] D.T.J. Hurle and B. Cockayne in: Characterization of Crystal Growth Defects by X-Ray Methods, NATO Advanced Studies Institute Series, Ser. B, Physics, Vol 63, Eds. B.K. Tanner and D.K. Bowen (Plenum, New York, 1983) p.50.
[14] J.C. Brice, J. Crystal Growth 7 (1970) 205.

[15] G.O. Meduoye, D.J. Bacon and K.E. Evans, J. Crystal Growth 88 (1988) 409.
[16] J.C. Brice, J. Crystal Growth 6 (1970) 205.

CHAPTER 4

OPTICAL CHARACTERIZATION OF DISLOCATIONS

OPTICAL CHARACTERIZATION OF CRYSTAL DISLOCATIONS: THE CASE OF BISMUTH GERMANATE

W.J.P. van Enckevort [*,**] and F.Smet [*]

[*] Dept. of Solid State Chemistry,
Dept. of High Energy Physics,
Faculty of Science, Catholic University,
Toernooiveld, Nijmegen, The Netherlands

[**] Drukker International B.V.
Beversestraat 20
5431SH Cuijk, The Netherlands

Abstract

Dislocations in $Bi_4(GeO_4)_3$ single crystals were characterized by several optical methods:
i) Chemical etching followed by etch pit examination using optical microscopy.
ii) Stress birefringence microscopy, a method that reveals the anisotropy of the stress field around dislocations. For dislocations viewed end-on, the sign of the edge component has been determined by a simple procedure involving external compression of the crystal. Birefringence images of dislocations viewed side-on are only obtained when the Burgers vector has an edge component parallel to the direction of observation.
iii) Parallel beam, Schlieren and phase contrast microscopy, combined with analog contrast enhancement. By these techniques the field of mass densities around the dislocation is observed.
iv) Dark field microscopy to detect the inclusion strings that might decorate dislocations.

1. Introduction

Dislocation structures in crystals are usually imaged by X-ray diffraction and electron microscopic methods [1,2]. Here deformations of the crystal lattice are the actual cause of the dislocation image contrast. Bismuth Germanate ($Bi_4(GeO_4)_3$, BGO) crystals however, have a high absorption coefficient for X-rays and electrons, so these methods are of limited applicability. On the other hand, BGO crystals are transparent for visible light, so optical characterization methods can be used. Etching of crystal surfaces followed by etch pit examination using a visible light microscope is an indirect optical method, which can be considered as a standard technique [3]. Direct observation of the dislocations by optical techniques like stress birefringence microscopy [4-7] and laser light scattering [8,9] has been reported in a limited number of cases. Here local changes in refractivity introduced by the dislocation stress field are actually observed.

In the present paper the possibilities and limitations of optical methods to characterize dislocations in Bridgman grown BGO crystals are described. By these methods some information on the dislocation structure of BGO has been obtained.

2. Experimental

2.1 Crystal Growth

The single crystals were grown by the research group at the Department of High Energy Physics, University of Nijmegen. The boules were obtained by lowering a platinum crucible, filled with molten, high purity BGO starting material in a vertical Bridgman furnace. The lowering rate varied from 0.5 to 3 mm per hour; the temperature gradient ranged from 3 - 30 °C per cm. In general the crystals (20 cm in length, 3 cm in diameter) were clear, transparent (sometimes slightly yellowish), and almost free of inclusions.

2.2 Etching

To mark the outcrops of dislocations as etch pits at the crystal surface, chemical etching was applied. Prior to etching slices parallel to the {112}, {111} and {100} planes were cut from the crystals. Subsequently the plates were polished carefully to obtain smooth, mirror-like surfaces. Etching was carried out by immersing the plates for 15 - 45 minutes in an aqueous solution of 1-4 M HCL. The surface patterns were examined by optical reflection interference contrast microscopy.

2.3 Stress birefringence, parallel beam and dark field microscopy

Bismuth Germanate is a cubic crystal [10] and thus optically isotropic. Stress fields around dislocation lines, however, generate a slight, local, optical anisotropy that can be recognized as a brightening when observed between crossed polarizers [11,12]. The stress birefringence patterns of dislocations were imaged by means of a good quality polarization microscope. As specimens polished BGO crystal plates of 1-2 mm thickness were used.

To observe the overall change in refractivity, i.e. the relative change in volume introduced by the dislocation stress field, use was made of parallel beam [13], Schlieren [14] and phase contrast microscopy [14]. The parallel beam technique, which was the most succesful, was realized by employing a bright field transmission microscope with its aperture diafragm for illumination closed to an opening of 1 mm or less. The image obtained in this way was recorded by a video camera, which was connected to an analog contrast amplifier. In this way contrasts, not detected by eye, could be seen on the monitor.

Inclusions down to ≈ 100 nm in size were observed by *conventional dark field microscopy* [15].

For all microscopic examinations it was essential to polish the crystal surfaces to a smooth mirror-like finish.

3. **Etching**

3.1 Crystallographic aspects

Etching of polished {112} crystal plates in an aqueous HCl solution results in the formation of well developed etch pits on one of the faces (fig. 1a) and elongated striated patterns on the opposite face (fig. 1b). This difference in etch pattern is explained by the crystallographic non-equivalence of the opposite $\{112\}/\{\bar{1}\bar{1}\bar{2}\}$ faces in the point group $\bar{4}3m$ of BGO [10]. In both cases the etch patterns obey the two-dimensional point group symmetry, m of the $\{112\}/\{\bar{1}\bar{1}\bar{2}\}$ faces in point group $\bar{4}3m$ [16].

Also etching of {111} plates gave a difference in surface morphology for the opposite sides which are in the point group $\bar{4}3m$ non-equivalent: One of the faces showed well formed triangular pits (fig. 1c), fulfilling surface symmetry 3m1 [16], the opposite face only revealed an undefined pattern without clear pits. Etching of {100} plates yielded the same rough, granular pattern for both opposite faces (fig. 1d). In point group $\bar{4}3m$ {100} and $\{\bar{1}00\}$ are indeed equivalent.

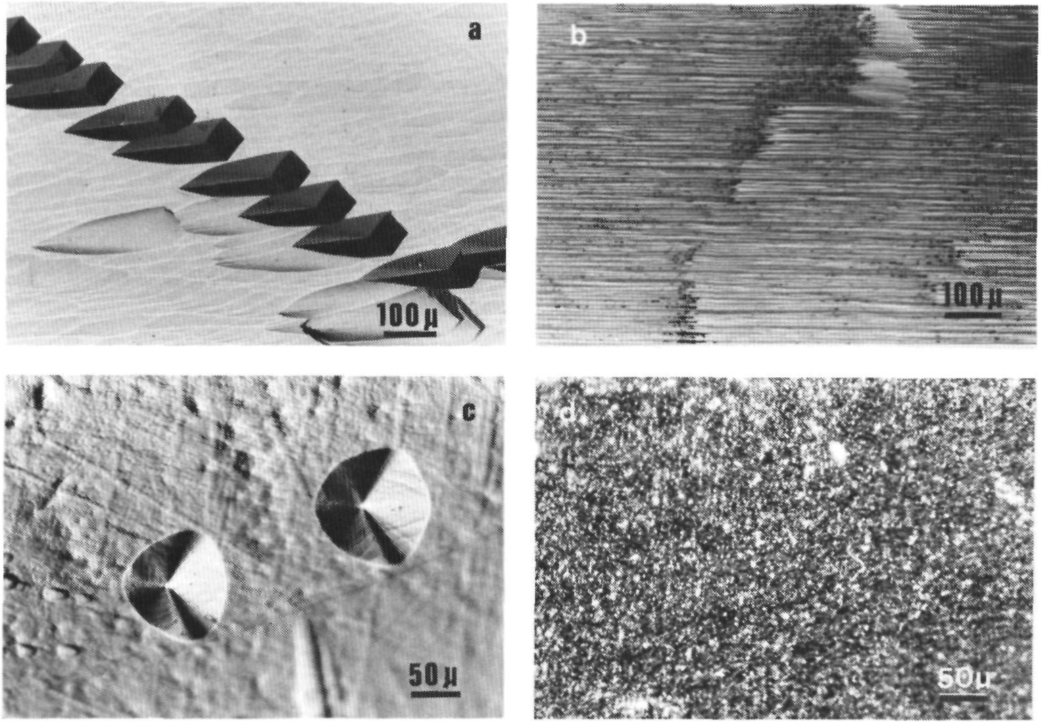

Fig. 1 Surface patterns on BGO formed after etching in an aqueous HCl solution: a) {112} face; b) {$\bar{1}\bar{1}\bar{2}$} *face; c) {111} face; d) {100} face.*

3.2 Correlation pits with dislocations

To verify whether the pits on the {112} faces are connected with dislocation lines ending at the surface, several slices (≈ 1mm thickness) were cut normal to the growth axis of one, high perfection BGO crystal rod, grown along the <112> direction. Subsequently the slices were polished and etched. For groups of successive slices it was found that the etch pit patterns of the {112} faces were (apart from slight translations) essentially identical. This means that the pits are related to line defects, which traverse the crystal plates perpendicular to the surfaces. Other evidence for a correlation with dislocations is that the etch pits often occur in rows, representing low angle grain boundaries.

BGO crystals, grown along the <112> direction by the Bridgman method are characterized by growth via a plannar melt-solid {112} interface perpendicular to the rod axis, as shown in a previous paper [17]. Combined with the fact that the dislocations run parallel to the growth axis, it follows that the defect lines tend to be oriented normal to the growth faces. Such a relative orientation of dislocations with respect to growth faces is typical for many solution and melt grown crystals and results from dislocation line energy minimalization during crystal growth [18].

In the remaining part of this work, the dislocation etch technique was used as a tool for identification of dislocations, observed by the other optical methods.

4. Stress birefringence microscopy

4.1 Dislocations viewed end-on

To obtain polarization microscopic images of dislocations viewed end-on, polished {112} slices, cut from the <112> crystal boule described in sect. 3.2 were used as specimens. The large majority of the birefringence images were similar to the patterns shown in fig. 2, which are characteristic for an edge dislocation viewed along its line direction in the presence of a long range back ground anisotropy [11,19]. The correlation of the birefringence patterns with dislocations was confirmed by etching. Figure 3a shows a row of birefringence images viewed end-on in a {112} plate. After chemical etching of the surface just above the crystal volume of fig. 3a , a group of dislocation pits was formed (fig. 3b). Comparison of figure 3a with 3b shows that each birefringence feature corresponds with a pit, i.e. a dislocation. In addition very few pits were observed which were not related with a birefringence image. Presumably these correspond with screw dislocations, which are -at least in (opto)elastic isotropic materials- not detectable by polarization microscopy [20].

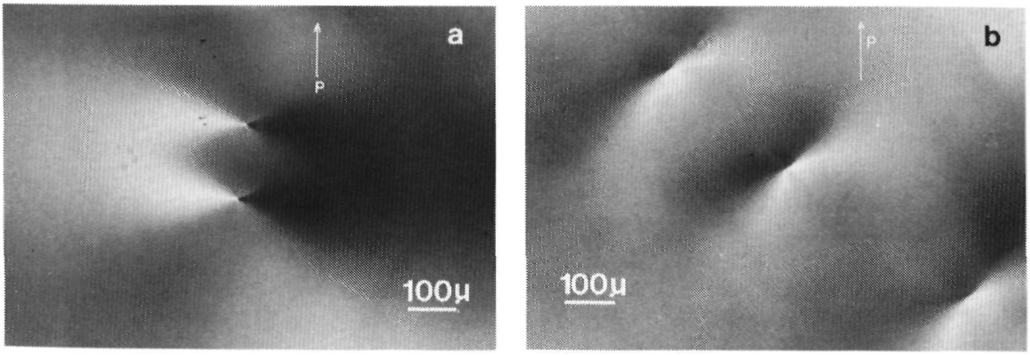

Fig. 2 Stress birefringence contrast of edge dislocations in BGO viewed end-on: (a) Polarizers parallel and normal to Burgers vector; (b) Polarizers oriented 45° with respect to Burgers vector.

The intensity levels of all the observed birefringence images were very similar, and no smaller or weaker patterns were found. This indicates that dislocations with a Burgers vector of unit cell dimensions, for example <100>, 1/2<111> or <110> are involved. If dislocations of multiple unit cell length were to be imaged a whole range in image size and contrast would be found. The almost one to one correspondence between dislocation patterns and etch pits gives additional evidence for unit dislocations.

From the lobe patterns of the majority of the dislocation images

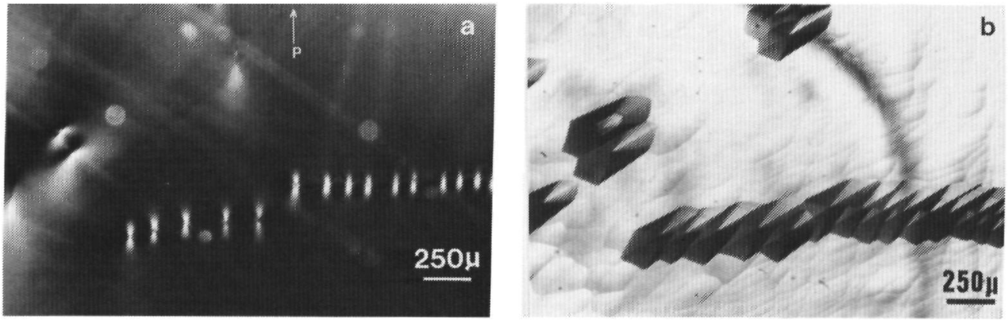

Fig. 3 Correspondence between birefringence images of dislocations and etch pits: (a) Polarization micrograph showing photo-elastic images of dislocations; (b) Pattern of pits formed after etching of the surface just above the crystal volume in (a).

the Burgers vector's edge component was deduced to be oriented 45±5 ° with respect to the $(\bar{1}10)$ mirror plane normal to the {112} slice surface. This corresponds with an orientation parallel to $[0.2\ \overline{2.2}\ 1.0]$ or its mirrored equivalent $[\overline{2.2}\ 0.2\ 1.0]$ (which will not be considered further) in point group $\bar{4}3m$. The screw component of a dislocation (as far as elastic and opto-elastic isotropic media are concerned) can not be imaged end-on [20], so no information on that component was obtained by the stress birefingence method. Since the total Burgers vector is the sum of an unknown screw component // [112] and an edge component // $[0.2\ \overline{2.2}\ 1.0]$ it is expected that it is parallel to one of the directions in the crystallographic zone $[\overline{2.3}\ 0.3\ 1.0]$ [21]. Because of energy minimalization, Burgers vectors tend to correspond with very low index crystallographic vectors. Since [010] is the low index vector, which lays closest to the $[\overline{2.3}\ 0.3\ 1.0]$ zone, it is the most probable candidate for the total Burgers vector.

By focussing the microscope, it is possible to trace the path of the dislocation lines through the specimen crystals. In {112} plates, cut from highly perfect, <112> BGO boules the large majority of the dislocations ran perpendicular to the plate surfaces, a conclusion already drawn from the etching experiments. In lower quality crystals, the majority of the dislocation lines followed an irregular path and were not oriented perpendicular to the {112} faces. Since "as grown" dislocation lines should be straight [18], the curved ones must have been subjected to post-growth glide [18]. Near inclusions in the crystals, a high density of curled dislocation lines was generally found. Probably these resulted from plastic deformation introduced by a volume change of the inclusion during cooling after growth.

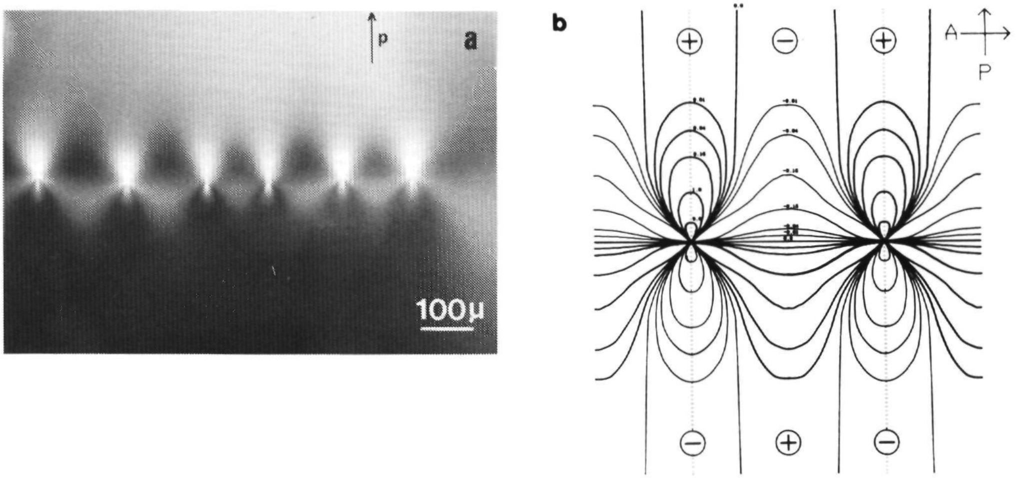

Fig. 4 Stress birefringence contrast of a tilt boundary. (a) Polarization micrograph of a linear array of dislocations with the edge component normal to the row direction, in the presence of a long range background stress field. (b) Iso-intensity profiles calculated for a tilt boundary in absence of a background stress field. A very clear birefringence photograph of a tilt boundary was also given by Nikitenko and Dedukh (Fig. 1b in [5]).

In many cases the dislocation patterns were ordered in rows, i.e. low angle grain boundaries [22], as shown in figure 4a. From the orientation of the lobe patterns it is suggested that the edge component of each dislocation is perpendicular to the row direction. This means that we are dealing here with a tilt boundary, which is a minimum energy configuration for a group of edge dislocations of equal sign [22]. Confirmation was obtained by comparison of figure 4a with a theoretical iso-intensity plot of a tilt boundary (fig. 4b), drawn on the basis of equations (18) and (19) in the work by Bullough [4].

Apart from dislocations, the boundaries between adjacent growth sectors [18], also introduce birefringence patterns in BGO crystals (fig. 5). The contrast was large for boundaries between strong [17] {112} and weak [17] {$\bar{1}\bar{1}\bar{2}$} sectors, a weak contrast was observed at the boundary of two {112} sectors and no contrast was found for adjacent {$\bar{1}\bar{1}\bar{2}$} sectors. In all cases maximal birefringence contrast was observed when the crossed polarizer and analyzer were oriented 45° with respect to the boundary direction. Extinction occurred when oriented 0°. In a previous paper [17] it was shown that the optical properties of adjacent {112} and {$\bar{1}\bar{1}\bar{2}$} sectors were not equal, because of a difference in defect concentration. This might cause a small difference in lattice parameter between adjacent BGO crystal volumes which again introduces stress near the sector boundary as reported earlier for the interface between {100} and {101} sectors in KH_2PO_4 crystals [23,24].

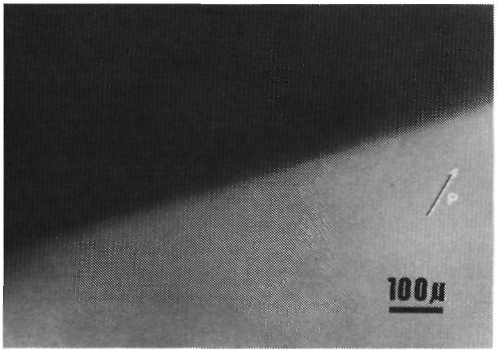

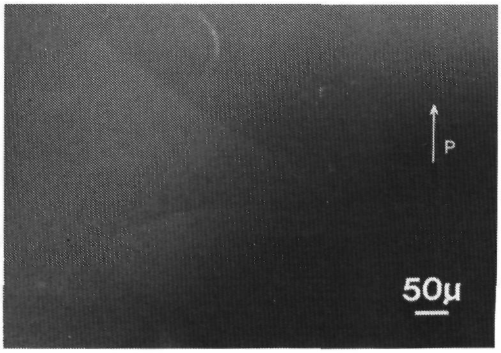

Fig. 5 Birefringence contrast at the boundary of adjacent {112} and $\{\bar{1}\bar{1}\bar{2}\}$ *growth sectors in BGO.*

Fig. 6 Stress birefringence image of a curved dislocation viewed from side. The defect line is in its maximum contrast orientation, which is 45° with respect to the polarizers.

4.2 Dislocations viewed side-on

To observe dislocations from the side, crystal plates were cut parallel to the growth direction of <112> grown boules and subsequently polished. Based on image contrast when viewed side-on by a polarization microscope the dislocation lines can be grouped into two categories:

i) Grown-in, straight dislocations parallel to <112>. Maximum contrast is obtained when the dislocation line (**l**) is oriented 25 - 30° or 115 - 120° with respect to the direction of the polarizer. Extinction occurs when oriented -20 - -15° or 70 - 75°. The contrast of the dislocation images is asymmetric: a sharp bright-dark transition along the defect line can be seen [6,12].

ii) Curved dislocations formed as a result of plastic deformation. Figure 6 gives a birefringence image of such a defect line in its maximum contrast orientation of 45°. Extinction is found when oriented 0° or 90° with respect to the crossed polarizers. Again the contrast is asymmetric. The behavior of the image contrast is independent of the line direction **l** in the crystal.

The extinction at the 0° and 90° orientations for the curved dislocations (type ii) indicates that edge dislocations are involved [11,20]. The asymmetric contrast points to an edge component more or less parallel to the microscope's optical axis [6,12]. Without exception this is the only Burgers vector component that was encountered for the type ii dislocations, regardless of the line direction. No dislocation lines with symmetric contrast or with extinction at 45° were found. This suggests that only edge components parallel to the microscope's axis can be imaged "side-on" by the photo-elastic method. In other words, for dislocations viewed side-on in BGO, edge components perpendicular to the optical axis and screw components give contrasts too weak to be seen. Recently this conclusion was also drawn for diamond [7].

From the above deduction for the curved dislocations that only edge components parallel to the microscope's optical axis can be imaged "side-on", it is suggested that the same holds for the grown-in dislocations parallel to <112> (type i). To verify this hypothesis a small (3x3x3 mm^3) cube of BGO, which contained a few, grown-in, dislocations was sawn and polished. The top and bottem faces were cut perpendicular to the defect lines; the side faces parallel and normal to the Burgers vector's edge component, $\mathbf{b}_-$ (fig. 7a). The orientation

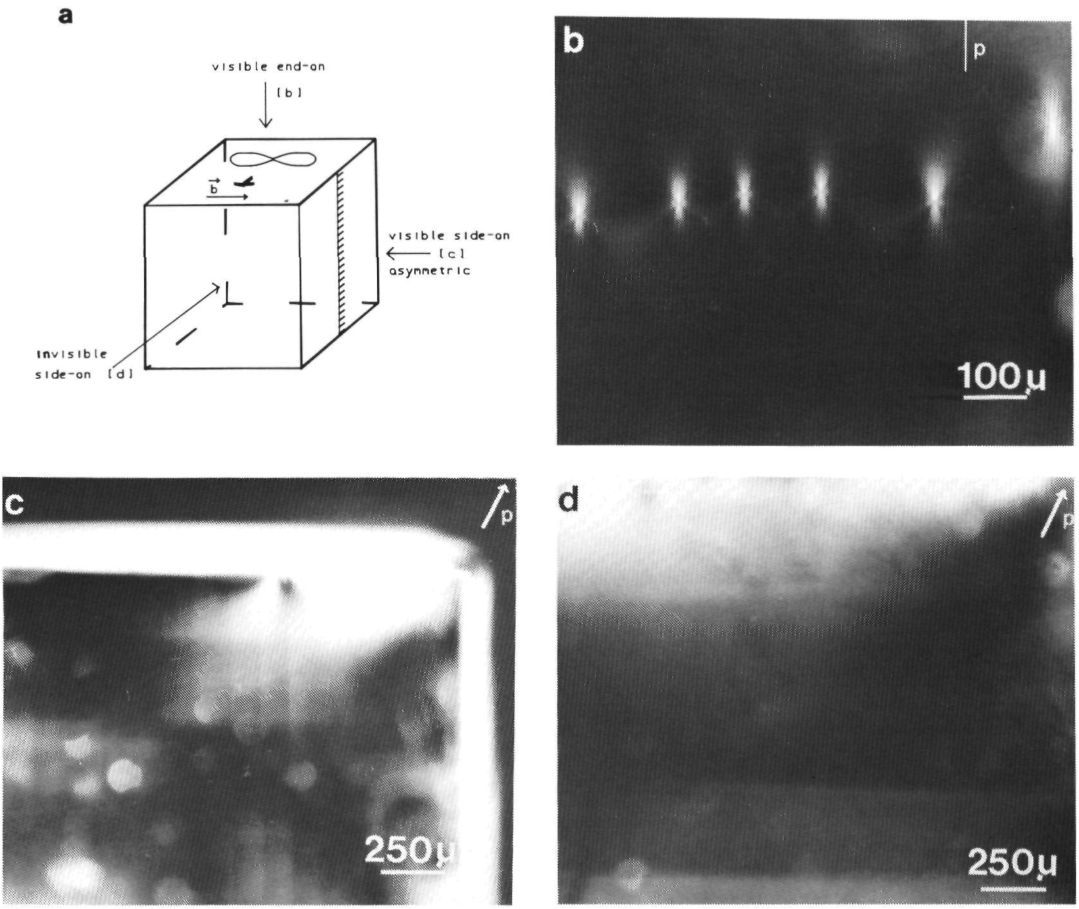

Fig. 7 Photo-elastic image contrast of dislocations in dependence of viewing direction: (a) Schematic representation of a BGO cube with a few dislocation lines perpendicular to the top and bottom faces; (b) Birefringence image viewed from top; (c) Image viewed from side, be parallel to the direction of sight; (d) No contrast when viewed from side and be perpendicular to the direction of sight.

of the latter was determined by stress birefringence microscopy from the top (fig. 7b).

Viewing through the cube faces parallel to **l** and normal to $\mathbf{b}_\perp$ shows the characteristic asymmetric birefringence images of dislocations type i, viewed side-on (fig. 7c). However, observation through the faces parallel to **l** and $\mathbf{b}_\perp$ revealed no detectable image contrast, regardless of the orientation with respect to the polarizers (fig. 7d). In other words, for type i dislocations also the only discernable image contrast is generated by edge components parallel to the microscope's optical axis. The somewhat different extinction positions of the type i dislocations compared to those for edge dislocations in isotropic materials [11,20], probably results from slight anisotropy of the elastic or opto-elastic behaviour of BGO.

During the above described experiment it was found that all the dislocations which were seen from the top of the sample could be imaged from one side (fig. 7d). Since these defects are characterized by a Burgers vector of unit length, this means that in BGO unit dislocations can also be observed side-on by polarization microscopy.

4.3 Sign determination of edge dislocations viewed end-on

The sign of the edge component of a dislocation line viewed from the top can be determined unambiguously by a very simple procedure. The method is as follows. First a dislocation is selected and the crossed polarizers are set parallel and perpendicular to the Burgers vector's edge component (fig. 8a and 9a), $\mathbf{b}_\perp$. In this case (fig. 8) the defect line is parallel to the z-axis, $\mathbf{b}_\perp$ to the x-axis and the extra half-plane is formed by the +y.z or -y.z half-planes depending on the sign of $\mathbf{b}_\perp$, (+x or -x respectively). In the absence of a long-range background stress field the birefringence image is dominated by two bright lobes pointing in the +x and -x directions. Then the crystal is compressed at an angle of +45° with respect to the +x axis (fig. 8b). When the +x lobe darkens and the -x lobe brightens, the extra plane is in the +y direction and $\mathbf{b}_\perp > 0$ (fig. 8b and 9b). When the opposite occurs, the extra half-plane is in the -y direction and $\mathbf{b}_\perp < 0$. Application of -45° compression leads to the reverse effect: the +x lobe brightens and the -x lobe darkens for $\mathbf{b}_\perp > 0$ (fig. 8c and 9c) and vice versa for $\mathbf{b}_\perp < 0$. Summarizing:

Sign(edge component) =
Sign(angle of compression)***Sign**(direction of dark lobe) [1]

The rule is elucidated in figure 8. In this drawing the strain tensors are schematized by ellipses. In the direction of the minor axis the crystal is compressed with respect to the direction of the major axis. Figure 8a shows that in the absence of a background strain field and for $\mathbf{b}_\perp > 0$ the major axes of the strain tensor ellipsoids at $y = 0$ are oriented +45° for $x>0$ and -45° for $x<0$.

Application of +45° compression generates a uniform strain tensor field, the ellipsoid of which has its major axis oriented -45° (fig. 8b). Addition of this field to the dislocation strain tensor field results in an increased strain anisotropy for the -x lobe and a decrease in anisotropy for the +x lobe. In other words the +x lobe darkens (less birefringence) and the -x lobe brightens (more birefringence). The same argument also holds for $\mathbf{b}_- < 0$ and compression at -45° (fig. 8c).

As explained in section 4.1 the edge component of the majority of dislocations directed along [112] parallels to $[0.2\ \overline{2.2}\ 1.0]$. Since in the point group $\bar{4}3m$ $[0.2\ \overline{2.2}\ 1.0]$ and $[\overline{0.2}\ 2.2\ \overline{1.0}]$ are not equivalent, it is relevant to determine the sign of $\mathbf{b}_-$. Application of the above described method to this category of grown-

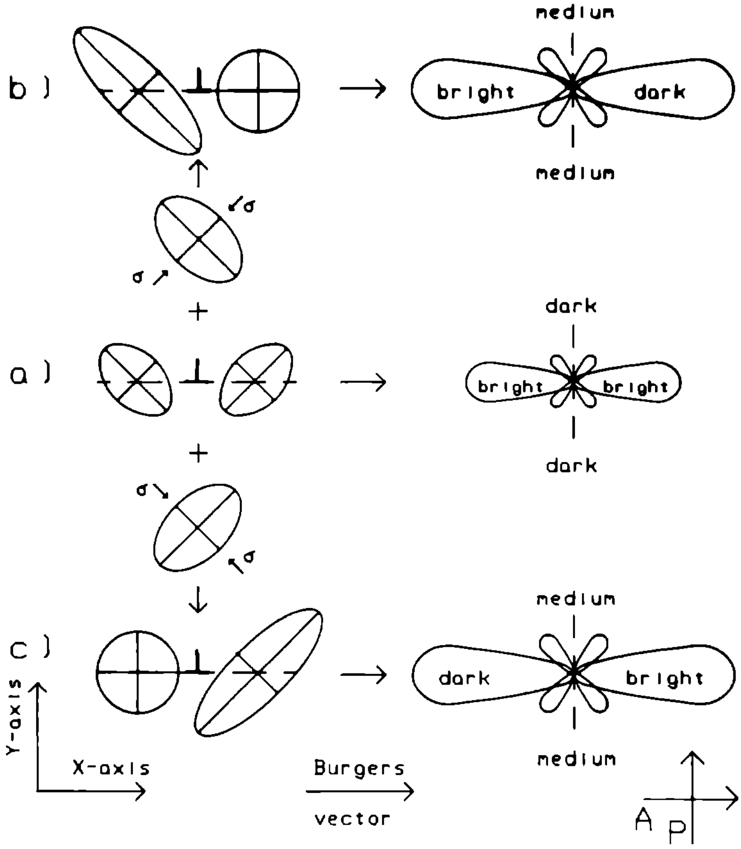

Fig. 8 Sign determination of an edge dislocation viewed end-on: (a) Image contrast and strain tensors at y = 0 of the edge dislocation in absence of external strain fields; (b) Change in image contrast and the y = 0 tensors upon application of external compression at +45° ; (c) Change of contrast upon compression at -45° .

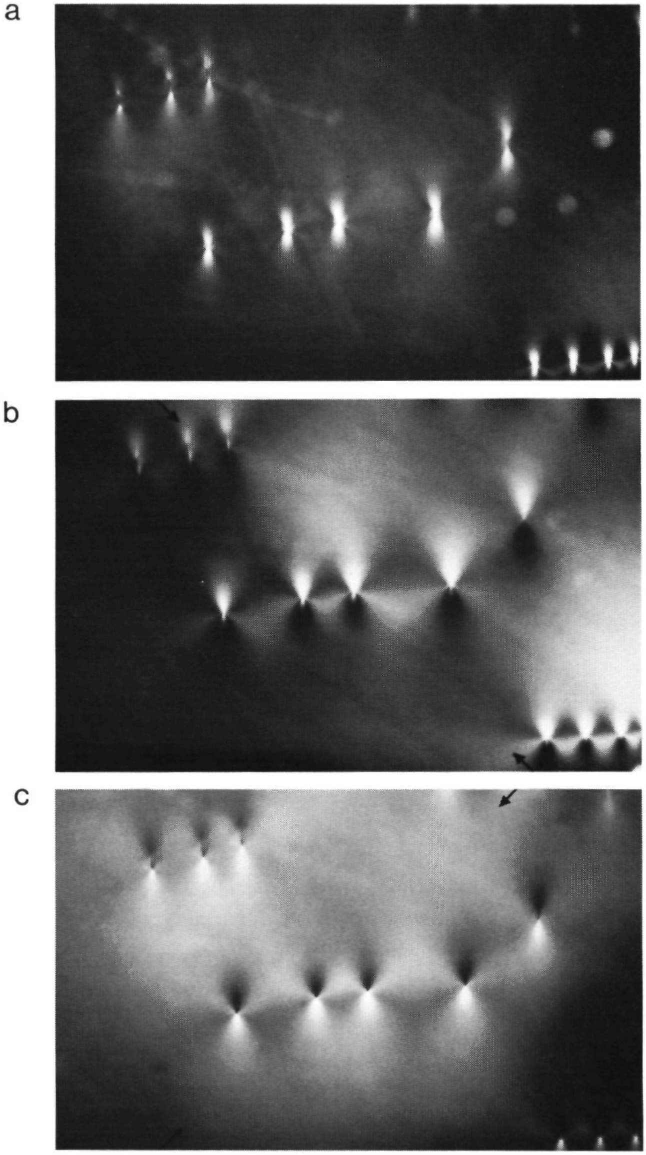

Fig. 9 Sign determination of the edge component of dislocations parallel to <112> in BGO: (a) Opto-elastic image of dislocations viewed end-on; (b) As (a) upon external compression at +45° ; (c) As (a) upon compression at -45° .

in dislocations (see fig. 9) showed that $\mathbf{b}_{-}$ is directed towards $[\overline{0.2}\ 2.2\ \overline{1.0}]$. This is roughly the same direction as for the projection of [010] on the (112) plane, so that the identity of the total Burgers vector as [010] is confirmed.

5. Phase sensitive microscopy

Parallel beam, Schlieren and phase contrast microscopy are all methods capable of imaging phase differences that result from light transmission through non-uniform objects. In appendix A it is shown that the relative volume change, i.e. the field of densities around dislocations can be mapped by making use of these methods in combination with unpolarized light. The image widths of dislocations viewed from the top are expected to be 10-20 times less than for stress birefringence microscopy.

Figure 10 shows a parallel beam (video) image of four dislocations viewed end-on in a {112} BGO plate. The width of the features is 5-10 μm, which is about one tenth the width of a birefringence image. The bright and dark background patterns are unsharp images of surface contamination and scratches. These are unavoidable, because of the extreme sensitivity of the method. By focussing through the specimen plate, the dislocation lines could be traced. The image quality for phase contrast and Schlieren microscopy was less than obtained by the parallel beam method.

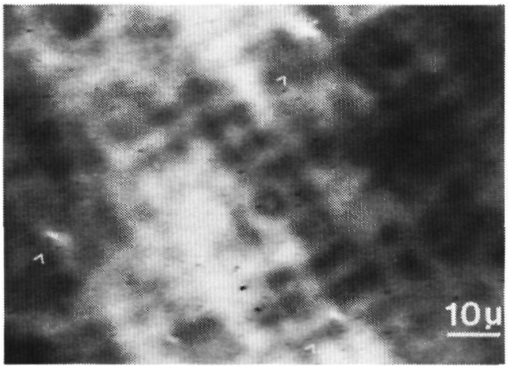

Fig. 10 Optical images of dislocations viewed end-on obtained by parallel beam microscopy followed by analog contrast enhancement.

By comparison of the birefringence and the parallel beam images of the dislocations it was found that the large majority of the dislocations in BGO are observable by phase sensitive microscopy. In other words the field of mass densities around unit dislocations produces detectable contrasts. To determine whether or not "hollow" tubes or precipitates at the dislocation cores [25] were observed instead of strain fields, dark field microscopy and laser light scattering tomography [9] were applied. By these techniques, which are capable of detecting submicroscopic particles, no evidence for the above mentioned phenomena was found.

As far as is known to us no optical imaging of the field of densities around individual dislocations has been reported in the literature.

6. Dark field microscopy

Recent work of among others Horowitz and Kramer [26] has established that BGO crystals often contain larger sized (several µm or more) inclusions, which comprise non-stoichiometric phases, gas bubbles and insoluble foreign particles. These defects are easily imaged by conventional bright field transmitted light microscopy. Application of dark field transmission microscopy to well polished crystal plates uncovered a second category of inclusions with a diameter below 1 µm. The best dark field images were obtained for crystal volumes free from larger sized inclusions: In that case the field of view was not clouded by scattered light of high intensity. The (sub)microscopic defects could not or only barely be seen by bright field microscopy.

The micro inclusions are not distributed uniformly in the crystals. Often they are ordered in extended rows, which are directed more or less perpendicular to the solidification front. In other crystal volumes they occur in large quantities, manifesting themselves as a "starry sky" in the dark field microscope. Verification by a low magnification polarization microscope showed that the latter crystal volumes are highly strained. The two different specific occurrences of the micro-inclusions in the BGO crystals suggest that a correlation exists with the dislocation structure.

To obtain more information on the relation ship between (sub)micro-inclusions and dislocations, use was made of stress birefringence microscopy. Figure 11a gives a photo-elastic image of a group of unit dislocations // [112] viewed end-on in a {112} slice, which was cut from a [112] BGO boule. Replacement of the polarization condensor by a bright field condensor followed by focussing slightly up and down, demonstrated that the inclusions are arranged along the dislocation lines (fig. 11b). This distribution is not arbitrary: For the different dislocation lines the inclusions are situated in the same (112) plane as schematized in figure 11c. This means that the defects were formed simultaneously at the various dislocation outcrops on the growing (112) facets during the crystallization process. Probably this was caused by a short period of decrease in supersaturation (or even dissolution), which led to the formation of a "hollow core" [25] (or etch pit) that was overgrown afterwards. In contrast to the general case of decorated dislocations, in the present situation the inclusions were not formed by precipitation of impurities from a supersaturated solid solution. In that case the defects would be distributed at arbitrary positions along the dislocation lines.

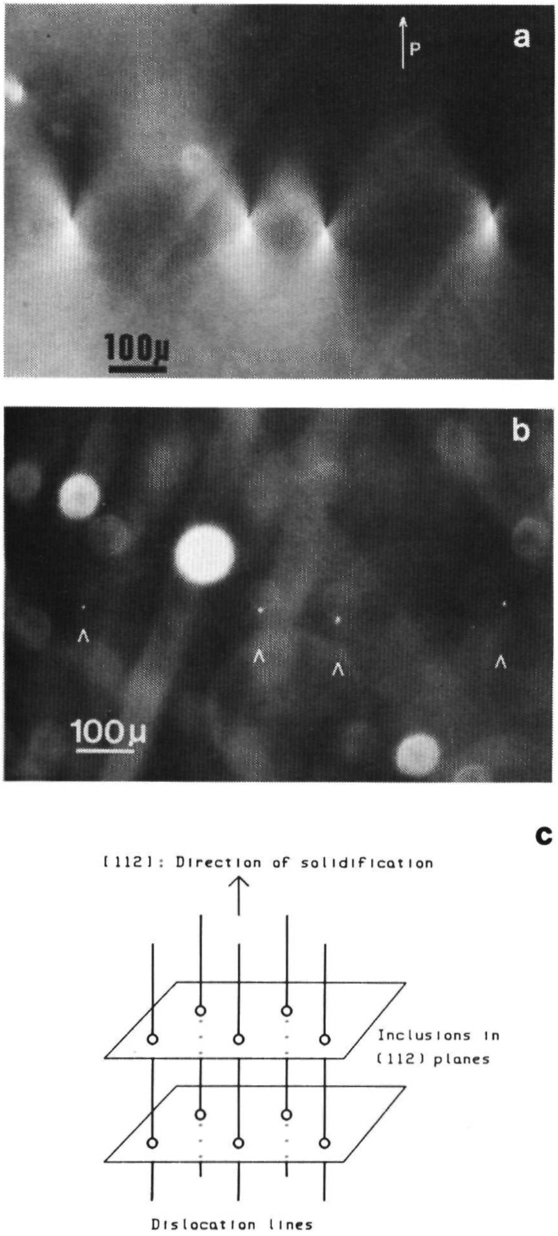
P
a
100µ
b
100µ
c
[112]: Direction of solidification
Inclusions in
(112) planes
Dislocation lines

Fig. 11 Relationship between micro-inclusions and dislocations in BGO: (a) Birefringence image of a group of dislocations viewed from top; (b) Dark field micrograph of the same volume as (a) revealing micro-inclusions located at the dislocation lines; (c) For different dislocations the micro-inclusions are positioned in the same {112} growth plane.

7. Conclusions

Dislocations in crystals like bismuth germanate may be characterized by several optical techniques. Indirect information on the lineair defects can be obtained by surface topography of etch pit patterns or by dark field microscopy of micro-inclusions that are positioned along the fault lines. Direct images of unit and larger dislocations are aquired by polarization microscopy, which displays the birefringence field, $\epsilon_1 - \epsilon_2$, and by phase sensitive microscopy which maps the field of densities, $\epsilon_1 + \epsilon_2$. By these direct techniques only edge components can be imaged in BGO. Screw components are thus invisible. For dislocations viewed end-on in the cubic crystals the birefingence method is more powerful than the "phase technique", because: i) The image size is 10 to 20 times larger, so less effort is required for observation and for measurement of Burgers vector orientation; ii) It permits the determination of of the sign of the Burgers vector's edge component. For non-cubic crystals, where the large intrinsic optical anisotropy overwhelms the weak birefringence associated with dislocations, phase sensitive microscopy might be more helpful.

Acknowledgements

The authors are indebted to Prof. P. Bennema, Dr. J.P. van der Eerden, Dr. M. Seal and Prof. R.T. van de Walle for their interest in the present work. Further they wish to acknowledge Drs. M. Raaymakers, J.J.H. Thörig, W.H. van der Linden and C. Brouwer for the growth of the BGO crystals. The authors are especially grateful to E.C. Antheunis for the cutting and careful polishing of the specimen crystals, which proved to be essential for this study.

This investigation was partly supported by the Foundation for Technical Sciences (STW).

APPENDIX A

Imaging of density fields around dislocations viewed end-on.

A.1. Phase sensitive microscopy

When a beam of light passes a phase object, the transmitted beam is characterized by a spatial variation in phase shift, $\Delta\Phi(r)$ [27]. This distribution of phase differences can only be imaged after conversion into intensity differences:

$$\Delta I(r) = I_o . f(\Delta\Phi(r)) \qquad (A.1)$$

where I_o is the incident beam intensity. Several optical methods are available to perform this task: phase contrast microscopy, $f(\Delta\Phi(r)) \approx \Delta\Phi(r)$ [27]; the Schlieren method, $f(\Delta\Phi(r)) \approx \delta\Delta\Phi(r)/\delta x$ or $\approx \delta\Delta\Phi(r)/\delta y$ [28]; and the parallel beam method, $f(\Delta\Phi(r)) \approx \delta^2\Delta\Phi(r)/\delta x^2 + \delta^2\Delta\Phi(r)/\delta y^2$ [29]. For all the three methods f fulfills the following requirements: i) f is independent of the polarization of the incident light;ii) $f[\Delta\Phi_1(r) + \Delta\Phi_2(r)] = f(\Delta\Phi_1(r)) + f(\Delta\Phi_2(r))$.

A.2. Spatial imaging of differences in optical density

Consider a slice of material with its plane-parallel surfaces parallel to x,y and the optical properties of which do not vary upon translation along z. The optical behaviour of a light beam passing through the slice perpendicular to its surfaces is determined by the two-dimensional indicatrix. This refractive index ellips is formed by the intersection of the three-dimensional indicatrix by the x,y plane [30]. The two main axes of the two-dimensional indicatrix are $\mathbf{r_1}$ and $\mathbf{r_2}$ ($\mathbf{r_1},\mathbf{r_2} \perp z$).

If a polarized beam // z with amplitude components $\sqrt{I_o}\cos\Theta(r)$ and $\sqrt{I_o}\sin\Theta(r)$, parallel to $\mathbf{r_1}$ and $\mathbf{r_2}$ respectively, traverses the plate then the image formed by phase sensitive microscopy is given by:

$$\Delta I(r) = I_o\cos^2\Theta(r) . f(\Delta\Phi_1(r)) + I_o\sin^2\Theta(r) . f(\Delta\Phi_2(r)) \qquad (A.2)$$

In this relation I_o is the incident beam intensity, $\Theta(r)$ is the angle between its polarization direction and $\mathbf{r_1}$. $\Delta\Phi_1(r)$ and $\Delta\Phi_2(r)$ are the phase shifts for the amplitude components parallel to the major and the minor axis. The orthogonal amplitude components parallel to $\mathbf{r_1}$ and $\mathbf{r_2}$ do not interfere with each other.

For unpolarized light:

$$\langle\Delta I(r)\rangle_o = {}^1/_2\,\pi \,.\int_0^{2\pi} \Delta I(r,\Theta)\,d\Theta$$

$$= {}^1/_2\, I_o \,.\, [f(\Delta\Phi_1(r)) + f(\Delta\Phi_2(r))] \,. \qquad (A.3)$$

The phase shifts $\Delta\Phi_1(r)$ and $\Delta\Phi_2(r)$ are determined by the slice thickness, d, the wavelength of the light, λ, and the refractive indices for the amplitude components parallel to the main axes, $n_1(r)$ and $n_2(r)$ according to:

$$\Delta\Phi_{1,2}(r) = d/\lambda \;.\Delta n_{1,2}(r) \tag{A.4}$$

From this and the additive property of $\int$, it follows that

$$<\Delta I(r)> = I_o d/2\lambda \;.\; \int[\Delta n_1(r) + \Delta n_2(r)] \tag{A.5}$$

A.3. Optical imaging of mass density fields in "two-dimensional" isotropic media

For isotropic media the optical birefringence tensor and the strain tensor are related to each other according [31]:

$$\frac{2}{n^3}\begin{pmatrix}\Delta n_1\\ \Delta n_2\\ \Delta n_3\\ \Delta n_4\\ \Delta n_5\\ \Delta n_6\end{pmatrix} = \begin{pmatrix} p_{11} & p_{12} & p_{12} & 0 & 0 & 0\\ p_{12} & p_{11} & p_{12} & 0 & 0 & 0\\ p_{12} & p_{12} & p_{11} & 0 & 0 & 0\\ 0 & 0 & 0 & (p_{11}-p_{12})/2 & 0 & 0\\ 0 & 0 & 0 & 0 & (p_{11}-p_{12})/2 & 0\\ 0 & 0 & 0 & 0 & 0 & (p_{11}-p_{12})/2 \end{pmatrix} \begin{pmatrix}\epsilon_1\\ \epsilon_2\\ \epsilon_3\\ \epsilon_4\\ \epsilon_5\\ \epsilon_6\end{pmatrix} \tag{A.6}$$

In this expression, n is the -scalar- refractive index of un-strained material; Δn_i are the changes in the six coefficients of the refractive index ellipsoid upon introduction of strain.
Further ϵ_i is the second order strain tensor and p_{ij} the stress optical coefficients.

In the present two-dimensional case of dislocations viewed end-on $\epsilon_3 = 0$, so that

$$[\Delta n_1(r) + \Delta n_2(r)] = n^3/2 \;.\; (p_{11}+p_{12}).(\epsilon_1(r) + \epsilon_2(r)) \tag{A.7}$$

This means that the change in optical density is proportional to the relative change in volume [31] and thus also in mass density. Substitution of A.7 in A.5 gives:

$$\Delta I(r) = I_o dn^3/4\lambda \;.\; (p_{11}+p_{12}) \;.\; \int[\epsilon_1(r) + \epsilon_2(r)], \tag{A.8}$$

or the image contrast for phase microscopy using unpolarized light is determined by the distribution of density.

A.4. Imaging of density fields around dislocations viewed end-on

The strain field around a screw dislocation is given by:

$$\begin{pmatrix} 0 & 0 & \epsilon_5(r) \\ 0 & 0 & \epsilon_4(r) \\ \epsilon_5(r) & \epsilon_4(r) & 0 \end{pmatrix} \qquad (A.9)$$

Since $\epsilon_1(r) + \epsilon_2(r) = 0$, this category of dislocations cannot be imaged end-on by phase sensitive microscopy.

For edge dislocations the elastic strain field is described by:

$$\begin{pmatrix} \epsilon_1(r) & \epsilon_6(r) & 0 \\ \epsilon_6(r) & \epsilon_2(r) & 0 \\ 0 & 0 & 0 \end{pmatrix} \qquad (A.10)$$

Using [4]:

$$\epsilon_1(r) = -Ay/r^4 \ . \ (x^2(3-2v) + y^2(1-2v)$$

and $$\epsilon_2(r) = -Ay/r^4 \ . \ (x^2(1+2v) + y^2(1-2v) \qquad (A.11)$$

gives, expressed in polar coordinates

$$\epsilon_1(r,\beta) + \epsilon_2(r,\beta) = -2A(1-2v)\sin\beta/r \qquad (A.12)$$

In this relation $r = x^2 + y^2$, β is the angle between x and r and $A = b/4\pi(1-v)$, where b is the Burgers vector and v is Poisson's ratio. A polar plot of this field of densities is given in figure 12. For phase sensitive microscopy the image contrast is proportional to $f[\epsilon_1(r) + \epsilon_2(r)]$.

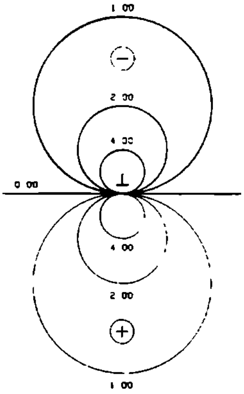

Fig. 12 Scalar field of strain (field of densities) around a dislocation viewed end-on.

A.5. Sizes of dislocation images: Comparison between stress birefringence and phase sensitive microscopy

The image size of an edge dislocation viewed end-on by polarization microscopy is given by [4,7]:

$$r_{bir} = 2\pi Ad/\lambda \ . \ 2(p_{11}-p_{12})/n^3 \ . \ P^{-1/2} \tag{A.13}$$

In this equation P is the detection limit of the polarization microscope used and is defined as the ratio of the beam intensity, after transmission through crossed polarizers in the absence of a specimen crystal, to the incident beam intensity.

From experience with the application of various phase sensitive techniques to undulate crystal surfaces [14] it is known that the mimimal detectable inclination or variation in inclination amounts to about 0.1 °. This corresponds with a gradient in phase shift $(d\Delta\Phi/dr)_{min}$ of 5.10^4 rad/m. The phase shift resulting from an edge dislocation viewed end on equals

$$\Delta\Phi(r) = 2\pi d/\lambda \ . \ 2(p_{11}+p_{12})/n^3 \ . \ [\epsilon_1(r) + \epsilon_2(r)] \tag{A.14}$$

Using equation (A.12), $\sin\beta = 1$ and differentiation gives

$$d\Delta\Phi(r)/dr = 4\pi A(1-2v)d/\lambda r^2 \ . \ 2(p_{11}+p_{12})/n^3 \tag{A.15}$$

From this it follows that the image width is

$$r^2_{ph} = 4\pi Ad(1-2v)/\lambda . 2(p_{11}+p_{12})/n^3 . (d\Delta\Phi(r)/dr)^{-1}_{min} \tag{A.16}$$

Devision of (A.13) and (A.16) results in

$$r^2_{ph}/r_{bir} = 2(1-2v)\sqrt{P} . (p_{11}+p_{12})/(p_{11}-p_{12}) . (d\Delta\Phi(r)/dr)^{-1}_{min} \tag{A.17}$$

Since the opto-elastic constants of BGO are not known, it is assumed that $p_{11}+p_{12}$ is in the same order of magnitude as $p_{11}-p_{12}$, or $p_{11}+p_{12} \approx p_{11}-p_{12}$. Using $v = 0.25$, $P = 10^{-4}$ and a birefringence lobe size of 100 μm gives $r_{bir} = 4.4$ μm. So the image size obtained by phase sensitive mocroscopy is about 1/20 th of the one obtained by the photo-elastic method. Probably the actual width is even less, due to effects resulting from beam divergence [7]. The large difference in image size explains the fact that in contrast to the photo-elastic technique, no observations of individual dislocations by phase microscopy have been reported in literature.

REFERENCES

[1] B.K. Tanner, X-ray Diffraction Topography, I.S. Science of the Solid State, Vol.10 (Pergamon, 1976).

[2] P.B. Hirsch, A. Howie, R.B. Ncholson, D.W. Pashley, and M.W. Whelan, Electron Microscopy of Thin Crystals (Butterworths, London, 1965).

[3] K. Sangwal, Etching of Crystals: Theory, Experiment and Application, Defects in Solids, Vol. 15 (North Holland, Amsterdam, 1987).

[4] R. Bullough, Phys. Rev. 110 (1958) 620.

[5] V.I. Nikitenko and L.M. Dedukh, Phys. Stat. Sol. (a) 3 (1970) 383.

[6] K. Löschke and P. Paufler, Phil. Mag. A 46 (1982) 699.

[7] W.J.P. van Enckevort and M. Seal, Phil. Mag. A 57 (1988) 939.

[8] K. Moriya and T. Ogawa, Phil. Mag. A 41 (1980) 191.

[9] W.J.P. van Enckevort and M. Seal, Phil. Mag. A 55 (1987) 631.

[10] A. Durif and M. Averbuch-Pouchot, Comp. Rend. Acad. Sc. Paris Série II 295 (1985) 555.

[11] B.K. Tanner and D.J. Fathers, Phil. Mag. A 29 (1974) 1081.

[12] P. Paufler and K. Löschke, Phil. Mag. A 47 (1983) 79.

[13] S. Takasu, Crystal Growth and Characterization, Eds. R. Ueda and J.B. Mullin (North Holland, Amsterdam, 1975) p. 317.

[14] See for instance: W.J.P. van Enckevort, Prog. Crystal Growth and Charact. 9 (1984) pp. 1-50.

[15] K. Löschke and A. Tempel, Kristall und Technik 15 (1980) 55.

[16] International Tables for Crystallography (Reidel, Dordrecht, 1983) Vol. A.

[17] F. Smet and W.J.P. van Enckevort, J. Crystal Growth 88(1988)169.

[18] H. Klapper in: Characterization of Crystal Growth Defects by X-ray Methods, Eds. B.K. Tanner and D.K. Bowen (Plenum Press, New York, 1980) p. 133.

[19] D.A. Jenkins and J.J. Hren, Phil. Mag. 33 (1976) 173.

[20] D.J. Fathers and B.K. Tanner, Phil. Mag. 28 (1973) 749.

[21] P. Hartman in: Crystal Growth, An Introduction, Ed. P. Hartman (North Holland, Amsterdam, 1973) pp 358-402.

[22] A.M. Kosevich in: Dislocations in Solids, Ed. F.R.N. Nabarro (North Holland, Amsterdam, 1980) Vol I, p. 66.

[23] C. Belouet and W.T. Stacy, J. Crystal Growth 44 (1978) 315.

[24] B. Dam, P. Bennema and W.J.P van Enckevort, J. Crystal Growth 74 (1986) 118.

[25] B. van der Hoek, P. Bennema and J.P van der Eerden, J. Crystal Growth 56 (1982) 621.

[26] A. Horowitz and G. Kramer, J. Crystal Growth 78 (1986) 121.

[27] M. Born and E. Wolf, Principles of Optics, 6th ed. (Pergamon Press, Oxford, 1987).

[28] W.J.P van Enckevort and M. Matuchova, Cryst. Res. Technol. 22 (1987) 167.

[29] J.M. Cowley, Diffraction Physics (North Holland, New York, 1975) p. 60.
[30] W.J.P. van Enckevort, J. Appl. Cryst. 20 (1987) 11.
[31] S. Bhagavantam, Crystal Symmetry and Physical Properties (Academic Press, London, 1966).

Journal of Crystal Growth 89 (1988) 471–477
North Holland, Amsterdam

DISLOCATION ETCHING OF ROUGH CRYSTAL FACES

W J P VAN ENCKEVORT * and F SMET

Department of Solid State Chemistry, Department of High Energy Physics, Faculty of Science Catholic University, Toernooiveld, 6525 ED Nijmegen, The Netherlands

Received 6 November 1987, manuscript received in final form 20 January 1988

A model for the preferential dissolution near the outcrops of dislocations at rough (K, S or F faces above the roughening temperature) crystal faces has been developed In contrast to F faces below the roughening transition, no lateral flow of steps from the etched dislocation centre occurs and therefore only small etch pits either not or only barely visible by optical microscopy are expected to be formed This was confirmed by etching of K, S and F faces of $Bi_4(GeO_4)_3$, KH_2PO_4 and potash alum crystals

After etching or dissolution of crystal surfaces, pits are often formed as a result of preferential etching near dislocation outcrops This well-known phenomenon has been used in many cases to investigate the density and distribution of dislocations in crystalline materials [1,2]

To obtain well-formed dislocation etch pits, clearly visible by optical microscopy, three requirements have to be fulfilled

(i) A preferential vertical etching near the dislocation line, generally due to the dislocation stress field, has to take place This aspect has been discussed in several papers [3,4]

(ii) A correlation between adjacent crystal surface regions [5] must be present, i e the crystal has to show a tendency to flatten via a flow of surface steps This allows for a lateral expansion (by step flow) of the etched region near the dislocation line leading to the formation of a macroscopic etch pit

(iii) The undersaturation should exceed a critical value, depending on dislocation stress and step free energy, before the lateral expansion mentioned in (ii) takes place [6,7] This is due to overcoming of a – step edge – energy barrier during the opening-up of the "hollow core" [3] along the dislocation line

In virtually all models describing the formation of dislocation etch pits, condition (ii) has been assumed implicitly However, the second condition is only fulfilled if the etched surface is more or less parallel to an F face [8] below the roughening temperature [9] Then etch pits are formed by lateral backward movement of growth steps emitted from a stressed dislocation outcrop Condition (ii) is not fulfilled for the class of rough faces, being K, S [8] or F faces above the roughening temperature [9] The present letter describes a mechanism of dislocation etch pit formation for this category of crystal surfaces

In the case of a rough crystal surface, no correlation between adjacent surface areas exists [5] There are no nucleation barriers (the edge free energy is zero [9,10]) and there is no tendency to flatten For such a surface in equilibrium with a saturated solution and with m different types of surface positions, the rate of release of dissolution units, n_0^-, is given by (fig 1a)

$$n_0^- = \frac{kT}{h}\sum_{i=1}^{m} N_{Si}^{s}\exp\left(-\frac{\Delta G_{s\ell i}^{*}}{kT}\right) = \frac{kT}{h}\sum_{i=1}^{m} N_{Si}^{s}\exp\left(\frac{\Delta S_{s\ell i}^{*}}{k}\right)\exp\left(-\frac{\Delta H_{s\ell i}^{*}}{kT}\right) \quad (1)$$

Here, N_{Si}^{s} is the density of solid surface positions of type i and $\Delta G_{s\ell i}^{*}$ ($=\Delta H_{s\ell i}^{*} - T\Delta S_{s\ell i}^{*}$) is the free

---

[*] Present address Drukker International B V, Beversestraat 20, 5431 SH Cuijk, The Netherlands.

0022-0248/88/$03 50 © Elsevier Science Publishers B V
(North-Holland Physics Publishing Division)

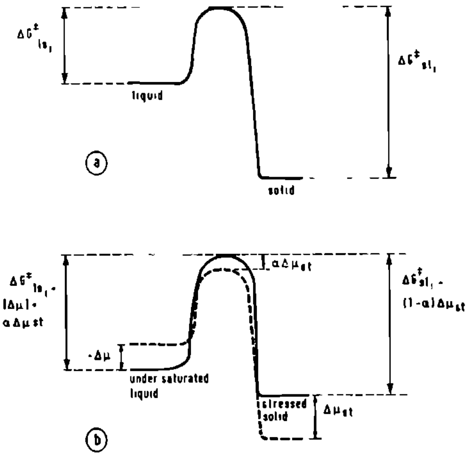

Fig 1 Free energy diagrams of (a) an unstressed rough crystal face in equilibrium with the fluid phase, (b) the dissolution of a stressed, rough crystal face

energy of activation [11] for release of a surface atom at position of type i. The rate of addition of dissolution units to the crystal surface, n_0^+, equals (fig. 1a):

$$n_0^+ = \frac{kT}{h} C_0 \sum_{i=1}^{m} N_{Si}^{f} \exp\left(-\frac{\Delta G^*_{\ell si}}{kT}\right)$$
$$= \frac{kT}{h} C_0 \sum_{i=1}^{m} N_{Si}^{f} \exp\left(\frac{\Delta S^*_{\ell si}}{k}\right) \exp\left(-\frac{\Delta H^*_{\ell si}}{kT}\right), \tag{2}$$

where $\Delta G_{\ell si}$ $(= \Delta H^*_{\ell si} - T\Delta S^*_{\ell si})$ is the free energy of activation [11] of addition of one unit to a fluid surface position type i (which upon a fluid–solid transition transforms into a solid site type i). N_{Si}^{f} is the number of fluid surface positions of type i and C_0 to the equilibrium concentration of units in the liquid phase. Since we deal with equilibrium, n_0^- equals n_0^+.

In fig. 1 the diagrams of free energy versus reaction coordinate are drawn for standard conditions, where the liquid phase concentration, C, and the surface concentrations N_{Si}^{s} and N_{Si}^{f} are unity, so that the concentration terms in G ($RT \ln C$ and $RT \ln N_{Si}$) are ruled out. If one considers a system with one type of surface site ($N_S^s = N_S^f = 1$), if follows from the equilibrium condition $n_0^- = n_0^+$ that $C_0 \exp(-\Delta G^*_{\ell s}/kT) = \exp(-\Delta G^*_{s\ell}/kT)$ Since for solutions $C_0 < 1$, this means that not only for growth, but also for equilibrium (and dissolution), $\Delta G^*_{\ell s}/kT < \Delta G^*_{s\ell}/kT$, as shown in fig. 1. Also for the multisite case, generally $\Delta G^*_{\ell si}/kT < \Delta G^*_{s\ell i}/kT$. However, for loosely bonded surface sites in systems with high C_0, $\Delta G^*_{\ell si}/kT$ might be larger than $\Delta G^*_{s\ell i}/kT$; in this case N_{Si}^{s} will be very low.

For a (by a dislocation stress field) stressed crystal in contact with an undersaturated solution the rates of release, $n^-_{s,u}(r)$, and addition, $n^+_{s,u}(r)$, are changed:

$$n^-_{s,u}(r) = \frac{kT}{h}\left[\sum_{i=1}^{m} N_{Si}^{s} \exp\left(-\frac{\Delta G^*_{s\ell i}}{kT}\right)\right]$$
$$\times \exp\left(\frac{(1-\alpha)\,\Delta\mu_{st}(r)}{kT}\right), \tag{3}$$

$$n^+_{s,u}(r) = \frac{kT}{h} C_0 \left[\sum_{i=1}^{m} N_{Si}^{f} \exp\left(-\frac{\Delta G^*_{\ell si}}{kT}\right)\right]$$
$$\times \exp\left(\frac{\Delta\mu - \alpha\,\Delta\mu_{st}(r)}{kT}\right). \tag{4}$$

In deriving these equations it was assumed that (see also fig. 1b):

(i) The driving force for dissolution of each unit is given by $\Delta\mu = \mu_f - \mu_s$ (μ_f = thermodynamic potential in solution; μ_s = thermodynamic potential of solid), which is negative. The undersaturation of the liquid (vapour) does not affect the activated state ($\Delta G^*_{s\ell i}$ remains unchanged).

(ii) The stress field of the dislocation introduces an increase in thermodynamic potential, $\Delta\mu_{st}(r)$, of each solid unit, which is position dependent and positive. Since it is probable that stresses in the solid state also affect the potential of the activated state, it is assumed that the free energy of activation is increased by $\alpha\Delta\mu_{st}(r)$, where $0 < \alpha < 1$.

(iii) All types of surface states have the same strain free energy per solid unit, $\Delta\mu_{st}(r)$. A similar assumption was also made for a Monte Carlo simulation study of the dissolution of a stressed {100} Kossel crystal surface [12].

The introduction of a stress field gives no essential change in the entropy terms of the activated state, since the vibration, rotation and translation properties are not influenced Therefore $\Delta\mu_{\mathrm{st}}(r)$ can be formulated in terms of an energy density function [12,4]

$$\Delta\mu_{\mathrm{st}}(r) = \Omega\, U(r), \tag{5}$$

where $U(r)$ is the strain energy density of the cylindrical stress field around a dislocation at a distance r from its core and Ω is the volume of one dissolution unit From this it follows that the rates of release and addition are ($n_0^- = n_0^+$):

$$n^-_{\mathrm{s\,u}}(r) = n_0^+ \exp\left(\frac{(1-\alpha)\Omega U(r)}{kT}\right), \tag{6}$$

$$n^+_{\mathrm{s\,u}}(r) = n_0^+ \exp\left(\frac{\Delta\mu - \alpha\Omega U(r)}{kT}\right) \tag{7}$$

The net dissolution rate of a – rough – crystal face, $R_{\mathrm{etch}}(r)$, is given by·

$$\begin{aligned} R_{\mathrm{etch}}(r) &= d\left[n^-_{\mathrm{s\,u}}(r) - n^+_{\mathrm{s\,u}}(r)\right] \\ &= dn_0^+\left[\exp\left(\frac{(1-\alpha)\Omega U(r)}{kT}\right) \right. \\ &\quad \left. - \exp\left(\frac{\Delta\mu - \alpha\Omega U(r)}{kT}\right)\right], \end{aligned} \tag{8}$$

where d is the height of one solid dissolution unit

The strain energy density around a dislocation line is given by [4,7]

$$U(r) = \mu b^2 K/8\pi^2 r^2, \tag{9}$$

where μ is the shear modulus of the crystal, b the Burgers vector length of the dislocation and K a dimensionless constant that depends on the type of dislocation In eq (9) the dislocation core is not taken into account, since this crystal volume has a radius (b to $10b$ [4]) far below the resolution limit of optical microscopy Further, the core region does not influence dissolution processes elsewhere at the crystal surface, since for rough faces no correlation exists between adjacent surface regions.

Since the strain energy density, and thus the etch rate $R_{\mathrm{etch}}(r)$, decreases for increasing r, it is to be expected that a cylinder-symmetrical etch pit will be formed at the dislocation outcrop From the dissolution rate the profile ($h(r,t) = -tR_{\mathrm{etch}}(r)$) and the inclination ($\mathrm{d}(h(r,t)/\mathrm{d}r$) of this pit (after a time, t, of dissolution) is derived to be equal to

$$\begin{aligned} h(r,t) &= -tdn_0^+\left[\exp\left(\frac{(1-\alpha)C}{r^2}\right) \right. \\ &\quad \left. - \exp\left(\frac{\Delta\mu}{kT}\right)\exp\left(\frac{-\alpha C}{r^2}\right)\right], \end{aligned} \tag{10}$$

$$\begin{aligned} \frac{\mathrm{d}h(r,t)}{\mathrm{d}r} &= 2tdn_0^+\left[\frac{(1-\alpha)C}{r^3}\exp\left(\frac{(1-\alpha)C}{r^2}\right) \right. \\ &\quad \left. + \frac{\alpha C}{r^3}\exp\left(\frac{\Delta\mu}{kT}\right)\exp\left(\frac{-\alpha C}{r^2}\right)\right], \end{aligned} \tag{11}$$

with $C = \Omega\mu b^2 K/8\pi^2 kT$

For the situation that the energy of the activated state is not altered by the presence of a stress field, i e , $\alpha = 0$, the expressions for the pit shape and inclination are simplified to

$$h(r,t) = -tdn_0^+\left[\exp\left(\frac{C}{r^2}\right) - \exp\left(\frac{\Delta\mu}{kT}\right)\right], \tag{12}$$

$$\frac{\mathrm{d}h(r,t)}{\mathrm{d}r} = 2tdn_0^+ \frac{C}{r^3}\exp\left(\frac{C}{r^2}\right) \tag{13}$$

The value of the pre-exponential term, dn_0^+, is obtained from the thickness of the layer etched from a non-stressed surface area, far away from the dislocation outcrop, $h(r \to \infty, t)$ From eq (10) and putting $r \to \infty$, it follows

$$dn_0^+ = -\frac{h(r \to \infty, t)}{t\left[1 - \exp(\Delta\mu/kT)\right]} \tag{14}$$

The etch pit profile expressed in terms of supersaturation and $h(r \to \infty, t)$ is given by

$$\begin{aligned} &\frac{h(r,t) - h(r \to \infty, t)}{h(r \to \infty, t)}\left[1 - \exp\left(\frac{\Delta\mu}{kT}\right)\right] \\ &\quad = \exp\left(\frac{\Omega\mu b^2 K}{8\pi^2 r^2 kT}\right) - 1, \end{aligned} \tag{15}$$

and is shown in fig 2 Somewhat farther away from the dislocation line the gradient is very low, near the centre the inclination suddenly increases, which gives the pit a trumpetlike shape

For small objects of several micrometers in size, the lowest inclination that can be detected by

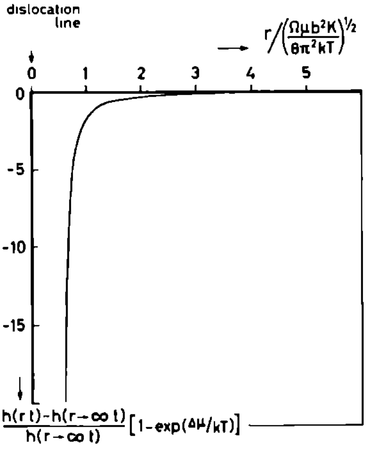

Fig. 2. Profile of dislocation etch pit formed after dissolution of a rough crystal surface expressed in dimensionless coordinates.

optical microscopy is about 1°. Based on this limit the radii at which the slope of the pit sides equals 1° were calculated for three different crystals. The calculations, the results of which are given in table 1, were done by using eqs. (13) and (14), taking $\alpha = 0$ and $K = 1$, and assuming that 0.1 mm ($= -h(r \to \infty, t)$) has been dissolved. It is obvious that for rough crystal faces dislocation outcrops are not, or for slightly undersaturated solutions just, detectable as etch pits by optical microscopy.

The etch pit sizes in table 1 were calculated on the basis of the assumption that $\alpha = 0$. However, since it is not evident that the energy of the activated state is not influenced by $\Delta\mu_{st}(r)$, the case $\alpha \neq 0$ should also be considered. From eqs. (11) and (13) it follows

$$\left(\frac{\mathrm{d}h(r,t)}{\mathrm{d}r}\right)_{\alpha\neq0} = \exp\left(\frac{-\alpha C}{r^2}\right)\left[(1-\alpha)\left(\frac{\mathrm{d}h(r,t)}{\mathrm{d}r}\right)_{\alpha=0} + \frac{2tdn_0^+C}{r^3}\alpha\exp\left(\frac{\Delta\mu}{kT}\right)\right] \tag{16}$$

For the distances ($r \approx 10^{-6}$ m) and crystals ($Bi_4(GeO_4)_3$, KH_2PO_4 and potash alum) considered here, $C/r^2 \approx 10^{-6}$, so $0 < \alpha C/r^2 < 10^{-6}$. This implies that $\exp(-\alpha C/r^2)$ approaches one and (from (13))

$$\left(\frac{\mathrm{d}h(r,t)}{\mathrm{d}r}\right)_{\alpha=0} = \frac{2tdn_0^+C}{r^3} \tag{17}$$

Now eq. (16) is reduced to

$$\left(\frac{\mathrm{d}h(r,t)}{\mathrm{d}r}\right)_{\alpha\neq0} = \left(\frac{\mathrm{d}h(r,t)}{\mathrm{d}r}\right)_{\alpha=0}\left\{1-\alpha\left[1-\exp\left(\frac{\Delta\mu}{kT}\right)\right]\right\} \tag{18}$$

Considering the fact that $\Delta\mu/kT$ is always negative and $0 \le \alpha \le 1$, it follows that $0 \le \alpha\ [1-\exp(\Delta\mu/kT)] \le 1$ and thus

$$\left(\frac{\mathrm{d}h(r,t)}{\mathrm{d}r}\right)_{\alpha\neq0} \le \left(\frac{\mathrm{d}h(r,t)}{\mathrm{d}r}\right)_{\alpha=0} \tag{19}$$

From this unequality it can be concluded that if

Table 1
Radii for which the slope of dislocation etch pits equals 1°, calculated for the rough faces of three different crystals

Compound	Property					
	$\lvert b\rvert \times 10^{-10}$ (M)	$\mu \times 10^{10}$ (N/M^2)	$\Omega \times 10^{-30}$ (M^3)	Radius where $\mathrm{d}h(r)/\mathrm{d}r = 1°$		
				$\Delta\mu/kT = -\infty$ $\times 10^{-6}$ (M)	$\Delta\mu/kT = -0.1$ $\times 10^{-6}$ (M)	$\Delta\mu/kT = -0.01$ $\times 10^{-6}$ (M)
$Bi_4(GeO_4)_3$	≈ 10 [13]	≈ 3 [14]	289 [13]	0.7	1.5	3.1
KH_2PO_4	≈ 7 [15]	1.5 [15]	96 [16]	0.3	0.6	1.4
Potash alum	≈ 15 [17]	0.58 [17]	900 [17]	0.7	1.6	3.5

Dissolved layer thickness of unstressed surface ($h(r \to \infty, t)$) is 10^{-4} M. K is assumed to be 1 (pure screw), $T = 300$ K.

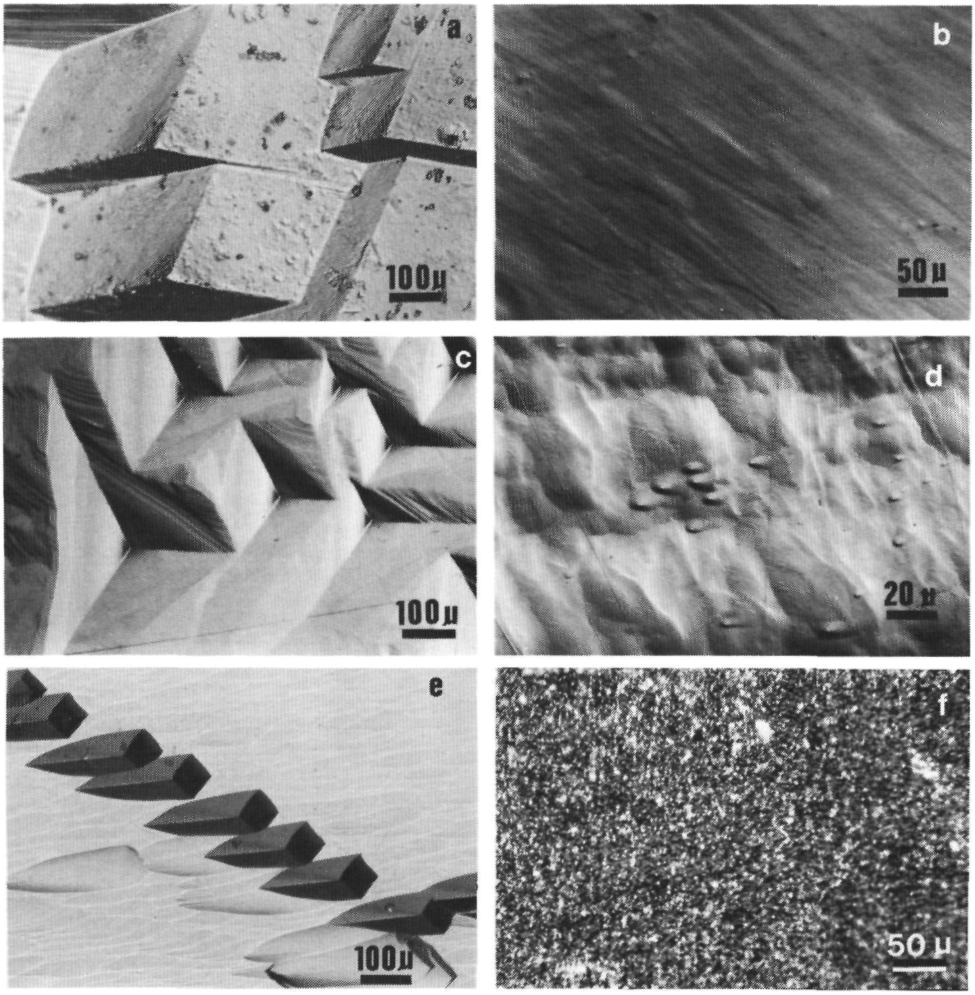

Fig. 3. Difference in dislocation etching of F and K (S) faces: (a) {101} and (b) {001} KH_2PO_4 etched in water; (c) {111} and (d) non-crystallographic oriented potash alum face etched in water; (e) {112} and (f) {001} bismuth germanate etched in 10% HCl/90% H_2O.

$\alpha \neq 0$ the inclination of the etch pit walls is reduced, so that their visibility is even less than as given in table 1.

From eq. (13) it follows that $\mathrm{d}h(r, t)/\mathrm{d}t$ is a monotonously decreasing function of r for all $\Delta\mu$. Therefore (small sized) dislocation pits are always formed during dissolution, regardless of the undersaturation. This is not in conflict with the model by Cabrera, Levine and Plaskett [4,6], which predicts that pits are only formed for $\Delta\mu$ less than a critical undersaturation $(\Delta\mu)_{\mathrm{crit}}$ This undersaturation is equal to

$$(\Delta\mu)_{\mathrm{crit}} = 2\pi^2\gamma^2\Omega/kTK\mu b^2 \tag{20}$$

where γ is the edge free energy of steps Since for rough faces $\gamma = 0$ [9], the critical undersaturation becomes zero and pits are formed for all undersaturation values

Fig 3 shows some results of etching experiments on KH_2PO_4, potash alum and bismuth germanate, which demonstrate the difference in dislocation etch pit formation between F and rough faces

Slight dissolution of {101} or {100} KH_2PO_4 and {111} potash alum in water results in the formation of well-developed dislocation pits [17,18] (figs 3a and 3c) These faces are F faces as shown by PBC analysis [19,20] On the other hand, etching of the K (S) type face {001} KH_2PO_4 [21] or several non-crystallographic faces (and thus S or K faces) of potash alum gave no or barely detectable etch pit patterns (figs 3b and 3d)

A similar result was obtained for bismuth germanate ($Bi_4Ge_3O_{12}$) crystals Etching of {112} faces in a ≈ 10% aqueous HCl solution (30 min) produced well formed dislocation etch pits [22] (fig 3e) On the {100} faces, however, only a grainy pattern with no discernable etch pits was created (fig 3f) From sphere growth experiments and morphological analysis of Bridgman grown crystals [23], it was shown that BGO crystals growing from the melt are bounded by {112} and $\{\bar{1}\bar{1}\bar{2}\}$ faces The growth of these faces proceeds via a step flow mechanism [23] Therefore it is beyond doubt that $\{112\}/\{\bar{1}\bar{1}\bar{2}\}$ BGO are F faces The BGO sphere growth experiments did not reveal {100} faces [23], so these behave like S or K faces at $T = 1340$ K The fact that upon chemical etching no pits were formed on the cubic faces shows that these faces remain rough at room temperature

From the theoretical considerations and experimental results described above, it is obvious that upon etching well-developed dislocation pits are only produced on F faces On K, S or F faces above the roughening temperature, only pits not or barely visible by optical microscopy are formed Therefore, in developing a dislocation etchant for a given crystal, it is essential to take care that the surface to be etched is parallel to an F face

In some situations larger sized dislocation etch pits, observable by an optical microscope might be formed on rough crystal faces, for example (i) In cases of surface reconstruction, where K/S faces get an F character [24] An example is {001} Si, from a crystallographic point of view a K face [8], where large sized pits are formed after gas-phase etching in HCl [25] and HI [24] (ii) In cases when the elastic stress field of the dislocation is not the only cause of preferential etching This might occur when a dislocation is heavily decorated or when the electrical properties of semiconductor materials are locally changed near the dislocation line

On the other hand, if at high undersaturations an F face etches thus fast that kinetical roughening [26] occurs, then it behaves like a rough face and no visible pits are expected to be formed

Acknowledgements

The authors are indebted to Prof Dr P Bennema and Prof Dr R T van de Walle for their interest in the present work Further they wish to acknowledge the financial support by the Foundation for Technical Sciences (STW)

References

[1] R B Heimann, Auflosung von Kristallen, Technische Mineralogie, Vol 8 (Springer Berlin 1975)

[2] K Sangwal Etching of Crystals Theory, Experiment and Application Defects in Solids Vol 15 (North Holland, Amsterdam, 1987)

[3] F C Frank, Acta Cryst 4 (1951) 497

[4] B van der Hoek J P van der Eerden and P Bennema, J Crystal Growth 56 (1982) 621

[5] W J Shugard J D Weeks and G H Gilmer Phys Rev Letters 41 (1978) 1399

[6] N Cabrera, M M Levine and J S Plaskett, Phys Rev 96 (1954) 1153

[7] P Bennema and W J P van Enckevort, Ann Chim Franç 4 (1979) 451

[8] P Hartman, in Crystal Growth An Introduction, Ed P Hartman (North-Holland, Amsterdam, 1973) pp 358–402

[9] H van Beijeren and I Nolden, to be published, see also J P van der Eerden, P Bennema and T A Cherepanova, Progr Crystal Growth Characterization 1 (1978) 219

[10] P Bennema, J Crystal Growth 69 (1984) 182

[11] K J Laidler, Chemical Kinetics (McGraw-Hill, New York, 1965)

[12] Liu Guang Zhao J P van der Eerden and P Bennema, J Crystal Growth 58 (1982) 152

[13] A Durif and M Averbuch-Pouchot, Compt Rend (Paris) (Sér II) 295 (1982) 555

[14] Derived from the anisotropic elastic constants c_{ij}, reported in Landolt–Börnstein, Neue Serie III/2 (Springer, Berlin, 1969)

[15] H Klapper, Yu M Fishman and V G Lutsau, Phys Status Solidi (a) 21 (1975) 115

[16] Derived from cell parameters and $Z = 4$, in A R Ubbelohde and I Woodward, Proc Roy Soc (London) A188 (1947) 358

[17] B van der Hoek, W J P van Enckevort and W H van der Linden, J Crystal Growth 61 (1983) 181

[18] W J P van Enckevort, R Janssen-van Rosmalen and W H van der Linden, J Crystal Growth 49 (1980) 502

[19] P Hartman, Acta Cryst 9 (1956) 721

[20] P Hartman, in Growth of Crystals, Vol 7, Ed N N Sheftal (Consultants Bureau, New York, 1969) p 53

[21] B Dam and W J P van Enckevort, J Crystal Growth 51 (1981) 607

[22] W J P van Enckevort and F Smet, work in progress

[23] F Smet and W J P van Enckevort, J Crystal Growth 88 (1988) 169

[24] L J Giling and W J P van Enckevort, Surface Sci 161 (1985) 567

[25] R Greevink, Gas-Phase Etching of {001} Si with HCl, Internal Report, Department of Solid State Chemistry, University of Nijmegen, 1976 (in Dutch)

[26] M Elwenspoek, Appl Phys A41 (1986) 123

CHAPTER 5

CRYSTALLOGRAPHIC STRUCTURE AND CRYSTAL HABIT:

THE MORPHOLOGICAL THEORY APPLIED TO BGO

CRYSTAL MORPHOLOGY OF BGO ($Bi_4Ge_3O_{12}$)

F. Smet, P. Bennema, J.P. van der Eerden and W.J.P. van Enckevort

Department of Solid State Chemistry, Department of High Energy
Physics, Faculty of Science, University of Nijmegen,
Toernooiveld, 6525ED Nijmegen, The Netherlands.

Abstract:

The Periodic Bond Chain theory was applied to the crystal structure of Bismuth Germanate. Seven F-slices were found and their Morphological Importance determined. Good agreement was obtained with the results of sphere growth experiments of BGO and with literature data of hydrothermally- and flux grown eulytine-type crystals. The most predominant F-faces appear to be {112} and $\{\bar{1}\bar{1}\bar{2}\}$*, at some distance followed by {220},{310},{400} and {123}. For the corresponding 2-dimensional connected nets the Ising critical temperatures were calculated. Careful analysis of bond energies, taking the liquid phase composition and experimental data on the roughening temperatures of the crystal faces into account, leads to a value for the solid-liquid interaction in terms of wetting.*

1. Introduction

The properties of crystals, which are grown below the roughening temperature of the faces, can depend strongly on their habit. During growth of large single $Bi_4Ge_3O_{12}$ crystals by the Bridgman method this habit determines the morphology of the solid-liquid interface, which in its turn is of major importance for the crystal quality [1]. A prominent theoretic tool for the prediction of the habit is the PBC theory of Hartman and Perdok [2], which relates the atomic crystal structure to the occurrence and development of the crystallographic faces on crystal growth forms. Using the concept of uninterrupted periodic chains of strong bonds, i.e. PBC's, the faces with an F-character are identified and their relative morphological importance on crystal growth forms is determined by measure of their slice energy.

An important extension of the theory, that takes into account the basic geometry of the slices, is the application of statistical mechanical Ising models which result in a critical order-disorder transition [3].

In this paper the theory is applied to the crystal $Bi_4Ge_3O_{12}$ (BGO), growing from the melt. Special attention is devoted to the role of the motherphase in view of the complicated liquid behaviour within the system Bi_2O_3-GeO_2. Alternative growth units and varying bondstrengths are discussed.

The predicted M.I.is compared with morphological data on BGO and other eulytine-type crystals. In addition a series of growth experiments was carried out to verify the morphological calculations for the melt growth case.

2. Theory

Each crystal can be regarded as a unique combination of bond strength distribution and space group symmetry. The PBC analysis is a systematic investigation of the crystal bond structure searching for the strongest 2-dimensional bond networks parallel to planes, and the weakest boundaries separating them. These planes usually have the lowest growth rate and will determine the habit .

A short outline of the method is given below, for a more complete description see refs. [2,4].

The basis of the PBC theory is the concept of Periodic Bond Chains, uninterrupted chains of strong bonds between the growth units having the periodicity of the lattice. If at least two PBC's in the structure are interconnected, then there will exist a whole interconnected frame, a so-called 'connected net', parallel to them. The corresponding crystallographic plane will then posses an F-character,i.e. it will grow layerwise via a 2-dimensional nucleation or spiral growth mechanism. This in contrast to S-faces, which have only one PBC parallel to them, and K-faces, which have none. They are thought to grow without a nucleation step as rough faces. The bare basic connected net is expanded so that a connected net with a maximal energy content is obtained. The boundaries of the connected net are determined by the criterion that it must be possible to divide the whole crystal structure into equal parallel connected nets. For each {hkl} the whole crystal may thus be divided into slices which represent the lowest possible surface energy configuration in that direction.

The relative morphological importance (M.I.) of the slices found this way is usually determined from their slice energy, E_{slice} , i.e. the energy released when a slice is formed from its growth units. The attachment energy E_{att} is related to E_{slice} by $E_{cr} = E_{slice} + E_{att}$, where E_{cr} is the total crystallization energy.

Growth theories justify the relation R proportional to E_{att} [5], implying that the higher E_{att} , the lower the M.I. . This criterion was succesfully applied in the case of apatite and many others [6,7,8,4]. Other criteria to determine the M.I. which are used are:

i. *E1 + E2* in case of spiral growth and *E1 * E2* for two-dimensional growth, where E_1 and E_2 are the two minimal edge energies of the F-slice ; and

ii. Θ^C , the critical Ising temperature which is discussed below. The M.I. runs parallel with these quantities.

The actual presence of an F-face on the growth form still depends on whether its roughening temperature is above the temperature of growth. At the roughening temperature, the edge free energy approaches zero, and the nucleation barrier vanishes because the edges or steps are no longer rare as a statistical fluctuation.

Statistical mechanical theory provides a method by which from the geometry and bond energies of an F-slice, a critical temperature Θ^C can be derived, which is a good approximation for the roughening temperature Θ^R [4] of the corresponding face. This is until now the most sophisticated criterion for the M.I. of a slice.

Within this statistical mechanical model, the crystal-liquid *interface is interpreted as a two-dimensional Ising lattice*, a rectangular array of cells which are either solid or liquid [9]. The interaction energies between cells take the form

$$\Phi_i/kT = [\ \Phi^{fs} - {}^1/_2(\ \Phi^{ff} + \Phi^{ss}\ )\ ]\ /\ kT \tag{1}$$

where Φ^{ss}, Φ^{fs}, and Φ^{ff} denote respectively solid-solid, solid-liquid, and liquid-liquid bond energies between the growth units, in reference to complete separation. The dimensionless roughening temperature Θ^R and the equivalent α^R are expressed as:

$$\Theta^R_{hkl} = kT^R \Big/ {}^1/_2\Phi_j \tag{2}$$

where Φ_j is the strongest bond in the crystal, and

$$\alpha^R_{hkl} = \sum_{slice} \Phi_i \Big/ kT^R \tag{3}$$

for each hkl. In this notation E_{slice} equals $\Sigma_{slice}\,\Phi_i$. The calculation of Θ^C requires values for Φ^{ss}, Φ^{fs} and Φ^{ff} for each bond in eq.(1). A Φ^{ss} must be considered as the atomisation energy per bond, and can be determined from thermochemical data. The Φ^{ff} and the Φ^{fs} are hardly experimentally accessible and for them the proportionality hypothesis is often introduced:

$$\Phi_i^{ss} : \Phi_i^{fs} : \Phi_i^{ff} = \Phi_j^{ss} : \Phi_j^{fs} : \Phi_j^{ff} \tag{4}$$

This leads to a set of Θ^C_{hkl} which as a measure for the M.I. gives very satisfactory results [11,4].

In the case of solution growth in addition the 'equivalent wetting' condition can be put, which makes it possible to use the enthalpy of dissolution in order to calculate a relative value for T^c [11].

In the case of melt growth, the complete wetting condition $\Phi^{fs} = \Phi^{ff}$ gives $\Phi_1 = (\Phi^{ff} - \Phi^{ss})/2$, half the crystallisation energy per bond, and leads to the classical Jackson factor $\alpha_J = -\hat{\xi}\Delta H_{cr}/kT$. With the crystallisation energy an absolute value for T^c can be obtained. This last condition is however a severe restriction and cannot be expected to give accurate results. In addition, recent studies [12] indicate that in most cases the complete wetting condition must be abandoned, because in general $\Phi^{sf} < \Phi^{ff}$.

In the present investigation an attempt is made to determine the specific wetting conditions in the case of meltgrowth of BGO. Essential elements for reaching this purpose were: i) Careful examination of both the solid and liquid bonds in order to obtain reliable Φ^{ss} , Φ^{fs} , and Φ^{ff} ; ii) Θ^R , approximated by Θ^C , from calculations in sect. 5.4 ; iii) T^R from observations.

3. Crystallographic structure and spacegroup of BGO

$Bi_4Ge_3O_{12}$ (BGO) is isomorphous with $Bi_4Si_3O_{12}$, eulytine, which was firstly described by Menzer [13]. Eulytine has the complicated symmetry of spacegroup $I\bar{4}3d$. The atomic positions for BGO were refined by Durif et al. [14]. The cubic unit cell has an edge dimension $a_o = 10.497$ Å and contains four formula units.

Ge^{4+} with site symmetry $\bar{4}$ has an almost regular tetrahedral coordination of O^{2-} ions at distance 1.740 Å. Bi^{3+} , site symmetry 3, is coordinated by three O^{2-} ions at 2.160 Å and three O^{2-} ions at 2.605 Å , in a very deformed octahedron. One tetrahedron shares points with eigth octahedra. One octahedron shares edges with three other octahedra and shares points with six tetrahedra.

An interesting aspect of BGO is the presence of 'hole's in this structure. These are empty sites, pointsymmetry $\bar{4}$, which are enclosed tetrahedrically by O^{2-} ions at 2.47 Å.

No cleavage planes have been observed for BGO.

4. Bond analysis

An accurate bond description is an indispensable part of the PBC analysis. In order to obtain realistic values for Φ^{ss} , Φ^{fs} and Φ^{ff} , both solid and liquid phases were considered.

4.1 Bonds in the solid

BGO kcal/*N bonds*		BSO kcal/*N bonds*	
Ge-O	87.8	Si-O	109.9
Bi_1-O	72.7	Bi_1-O	72.5
Bi_2-O	60.2	Bi_2-O	59.5

Table 1 Bond energies calculated according to Sanderson [19].

In the (monomorphous) structure of BGO three different first nearest neighbour bonds are present:

i) Ge-O bonds with distance 1.740 Å
ii) Bi-O bonds with distance 2.160 Å (denoted by Bi_1-O)
iii) Bi-O bonds with distance 2.605 Å (denoted by Bi_2-O)

One formula unit contains twelve bonds of each type.

On inspection, a basic motif of the three bonds can be found in the structure, a star shaped arrangement around each O-atom (fig.2). The star is almost flat, the O-atom in the centre is 6° out of plane, seen from the points of the star. The bond structure can be described in an alternative way with these stars, taking polyhedra with the O-atom in the centre instead of the metal atoms. The polyhedron around O is an almost flat oblique triangle. The triangles share the Bi-Bi edge with one other triangle, the Ge-corner with three other triangles and the Bi-corners each with four triangles.

Also, with these stars, it is possible to apply a star-triangle transformation [15] on the bond structure, as is done in section 5.4 to simplify the slices. The transformation is exact [16].

According to the classical Pauling electronegativity scale, the ionicity of both Ge-O and Bi-O type bonds amounts to ≈50% [17].

The standard enthalpy of formation ΔH°_f is not available from literature. Therefore the atomisation energy E_{at}. of BGO, which is necessary for calculations of Φ^{oo} must be estimated. Using Born-Haber cycli, the E_{at} for GeO_2 was calculated to be 336 kcal/mol, for Bi_2O_3 this is 415 kcal/mol. Assuming the enthalpy of formation from the elements to be twice the enthalpy of formation from the oxides, the E_{at} of BGO is approximately 2500 kcal/mol. The Madelung energy of BGO was calculated as 19360 kcal/mol. A calculation using effective charges, which were derived in a crystal field analysis by Morrison et al. [18] yields 14000 kcal/mol. In view of these values it must be concluded that a pure ionic description of the structure is not adequate.

A more promising approach is the one by R. Sanderson [19]. It incorporates a consistent set of experimental bond energy data with the available results of quantum-mechanical descriptions of chemical bonds into a general scheme for the calculation of bond energies.

This method seems particulary suited for our purpose since it relates the experimental data to a first nearest neighbour description of the bondstructure.

The bond energies which were calculated this way for BGO are listed in table 1. The resulting E_{at} , 2655 kcal/mol , is close to the value estimated above, so these may be regarded with confidence.

4.2 Bonds in the liquid

Within the frame of the Hartman Perdok theory it is assumed that only bonds which are formed during the crystallization process can contribute to the solid-liquid interfacial energy. Therefore we will now focus our attention on the liquid phase in order to determine the growth units.

The liquid phase in the system Bi_2O_3-GeO_2 shows resemblance to silicate-melts where a variety of structure fragments is known to occur. Both GeO_2 and Bi_2O_3 are glass formers, and glass formation does occur in the range 100-50 mol% GeO_2 [20]. Riebling [21] has investigated the structure of the glasses in this system and concludes that at 60 mol% GeO_2 the three dimensional Ge-O-Ge network must be almost entirely depolymerised. At the BGO composition there should exist only isolated GeO_4 tetrahedra and he suggests a eulytine-like structure. A strictly eulytine-like liquid structure is however unlikely since there would be no reason for glass formation [22]. Therefore there must be some network formation in the liquid. Zhereb et al. [23] demonstrated the occurrence of temperature zones with different structure in the Bi_2O_3 -rich region. In their model the liquid can polymerize into sheets of $[Bi_2O_2]_n$ and chains of coupled GeO_4 tetrahedra. From our own observations [24] we found that these regions also exist near the BGO composition, and that the precise location may be dependent on oxygen pressure and impurity content. In addition, Bi_2O_3 rich melts are known to exhibit non-newtonian behaviour [25,26]. This implies a structural change of the liquid under viscous flow and points to a certain degree of polymerization due to Bi_2O_3.

The picture thus emerges that the liquid from which the crystal grows is partly polymerized and contains relative unstable clusters of both Ge-O and Bi-O type. For crystallization to occur both Ge-O and Bi-O liquid bonds need to be broken. The strength of these liquid bonds can not be very different in view of their equal ionicity and comparable strength of the corresponding solid bonds. We conclude that neither clusters built from Ge-O surrounded by Bi-O bonds, nor clusters built from Bi-O surrounded by Ge-O bonds, can be considered as growth units. In this respect there is a distinct difference between the present melt growth, and growth from low temperature solutions, where the bonds within complexes may be regarded as solid bonds which are not relevant for the PBC analysis. The appropriate choice for the growth units must then be the so-called complete dissociation model [10], i.e. all bonds contribute to the crystallization energy.

Although there exist no exact equivalents of the three solid bonds in the melt, it also does not contain any other bond types, like bonds with other atoms. In addition, as mentioned above, the bond character of the Bi-O and Ge-O bonds is similar. Therefore the use of the proportionality hypothesis in the calculation of the Φ^{fs} and Φ^{ff} seems justified here (see eq. (4)), implying

$$\Phi^{ss}{}_{Ge-O} : \Phi^{ss}{}_{Bi1-O} : \Phi^{ss}{}_{Bi2-O} = \Phi_{Ge-O} : \Phi_{Bi1-O} : \Phi_{Bi2-O} \qquad (5)$$

In practice the Φ's are a few percent of the Φ^{ss}'s.

5. PBC analysis

On preliminary inspection, the three-dimensional bond structure does not reveal any especially strong or weak directions. The strongest bonds, Ge-O , occur only in isolated GeO_4 tetrahedra and thus cannot form continuous chains. The next logical possibility would be chains of strongly connected GeO_4 tetrahedra. This is however effectively prevented by the presence of empty sites, which are always located in line between the tetrahedra. The only strong and compact constructions appear to be chains of Bi-atoms, each interconnected by two identical O-bridges, having a diamond-like appearance. These chains form helixes in the <100> and <111> directions.

The starting point of a more systematic approach is usually a search for PBC's in the directions of the shortest lattice translations [2]. We have adopted a somewhat different method, aimed directly at the detection of connected nets, using a dedicated computer program. This interactive computerprogram was capable of displaying 3-dimensional views or projections in all directions of the crystal structure, together with manoeuvrable slice borderings, thus enabling visual fitting of a particular slice content. The selected slices could be abstracted and displayed separately in several representations for further inspection. This allowed relative fast scans of various slice possibilities.

5.1 Procedure and criteria for the determination of the F-slices

Slices will have an average thickness d_{nhnknl} which corresponds to the periodicity of the surface energy cut parallel to {hkl}.

In general, the Morphological Importance of a slice is expected to be proportional to its thickness, in accordance with the classical Bravais-Friedel-Donnay-Harker law (BFDH,[27]). Therefore slices were investigated in order of decreasing thickness. The

No.	{HKL}	d, Å	Polar	Character
1	112	4.2854	P	F
2	220	3.7113		F
3	310	3.3194		F
4	321	2.8054	P	F
5	400	2.6243		F
6	420	2.3472		S
7	332	2.2380	P	S
8	431	2.0586	P	S
9	510	2.0586		S
10	521	1.9165	P	S
11	530	1.8002		S
12	532	1.7028	P	K
13	611	1.7028	P	K
14	541	1.6197	P	K
15	631	1.5477	P	K
16	444	1.5151	P	K

Table 2 Crystal forms in order of decreasing thickness of their slices (according to the BFDH law) ; polarity of the slices, and the morphological character of the faces.

d_{hkl} (according to BFDH) can be calculated from the space group with its extinction conditions [28] and are listed in table 2.

The structure was searched for the strongest connected nets fitting these slice dimensions. In principle each alternative slice must be considered and judged on the basis of its edge energy, i.e. the energy required for step creation on the corresponding crystal face. This criterion was translated into two crystallographic criteria which must be satisfied by the potential slices [4]:

i . The whole crystal graph must be partitioned unambiguously into independent basic connected nets . Basic connected nets are independent if they have no points in common.

ii. The stack of basic connected nets must be invariant under those symmetry operations which leave the direction of the reciprocal vector H^{*}_{hkl} perpendicular to the plane invariant.

The criteria imply that for a slice hkl containing symmetry elements according ii there will exist two alternatives shifted $^{1}/_{2}$ d_{hkl} with respect to each other [6]. This considerably reduces the number of alternatives to be investigated.

5.2 Projections in the most important directions

Since the atoms were chosen as the growth units, no increase in symmetry occurs for the crystal graph and the space group with its extinctions fully determines the periodicity in surface energy.

In fig. 1a and 1b projections of the structure in the most important directions <100> and <111> are given. In the projections the investigated slices are indicated, together with the unit cell edges. In most cases only two alternatives are possible for a slice (sect. 5.1) which are denoted $(hkl)_1$ and $(hkl)_2$.

In fig. 1b the 'helix' PBC's parallel to <111> are outlined. They are situated around 3_1 and 3_2 screw axes. The $(112)_1$ slice is seen to contain complete helixes, in pairs with opposite screw. The 'helix' PBC in the <100> direction is indicated in fig. 1a. As can be seen it cannot be fitted even in the thickest slice (220) parallel to <100>.

A total of eight connected nets were found leading to five crystal faces with F-character. For the slices of {420} to {444} in table 2 no connected nets could be detected. The corresponding crystal faces possess K or S character as indicated. Slices with $d_{nhnknl} < d_{444}$ were not investigated as they were considered too thin to contain a connected net.

5.3 Polar slices

Slices which do not contain symmetry elements that change the reciprocal vector H^*_{hkl} into $-H^*_{hkl}$ have a polar character. This means that although these slices have only one slice energy and one critical Ising temperature, the two sides of the slices exhibit a different surface structure to the liquid phase. The nucleation and growth mechanisms are bound to show differences for the two sides and may give rise to two distinguishable crystal faces. The slices with this property are marked 'P' in table 2.

An example of such slices are the slices of {112}. In fig. 1b it can be seen that near the right hand boundary of $(112)_1$ there are on the average more Ge-atoms, and on the left hand boundary there are on the average more Bi-atoms.

In the investigation of Bridgman grown BGO crystals two forms, {112} and $\{\bar{1}\bar{1}\bar{2}\}$, showing a large difference in growth rate and etching behaviour, were indeed found [1].

There is no information which side of the slice, i.e. which absolute crystallographic direction, must be assigned to the slower growing {112} face.

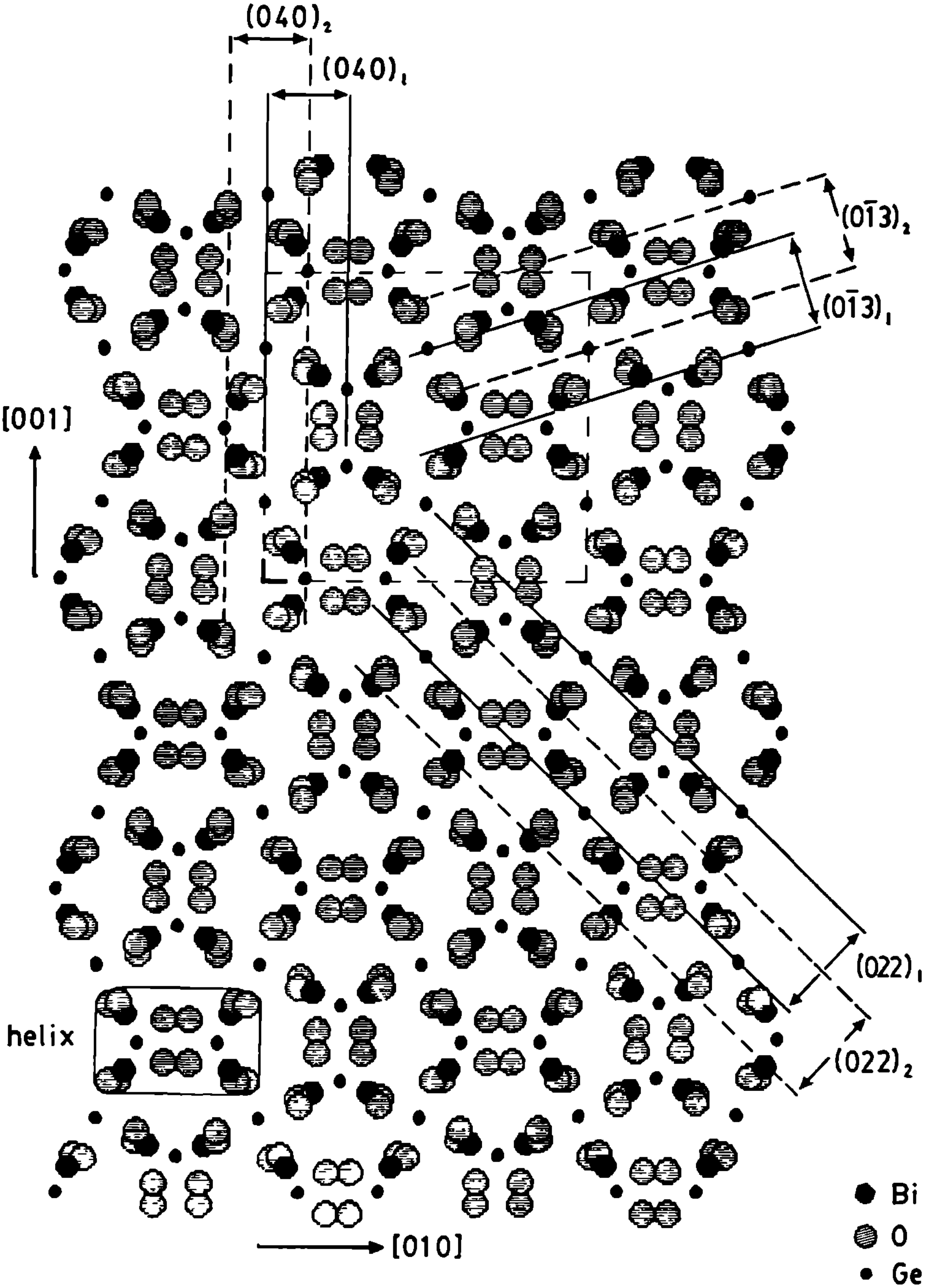
(040)₂
(040)₁
(0$\bar{1}$3)₂
(0$\bar{1}$3)₁
[001]
(022)₁
(022)₂
helix
[010]
● Bi
◍ O
• Ge

Fig. 1a Projection of the BGO structure along [$\bar{1}$00]. Unit cell edges are indicated by thin dashed lines. The pairs of slices have the relevant symmetry elements, the four fold inversion axes and the two fold screw axes, situated at the slice borders or in the middle of the slices. See section 5.2.

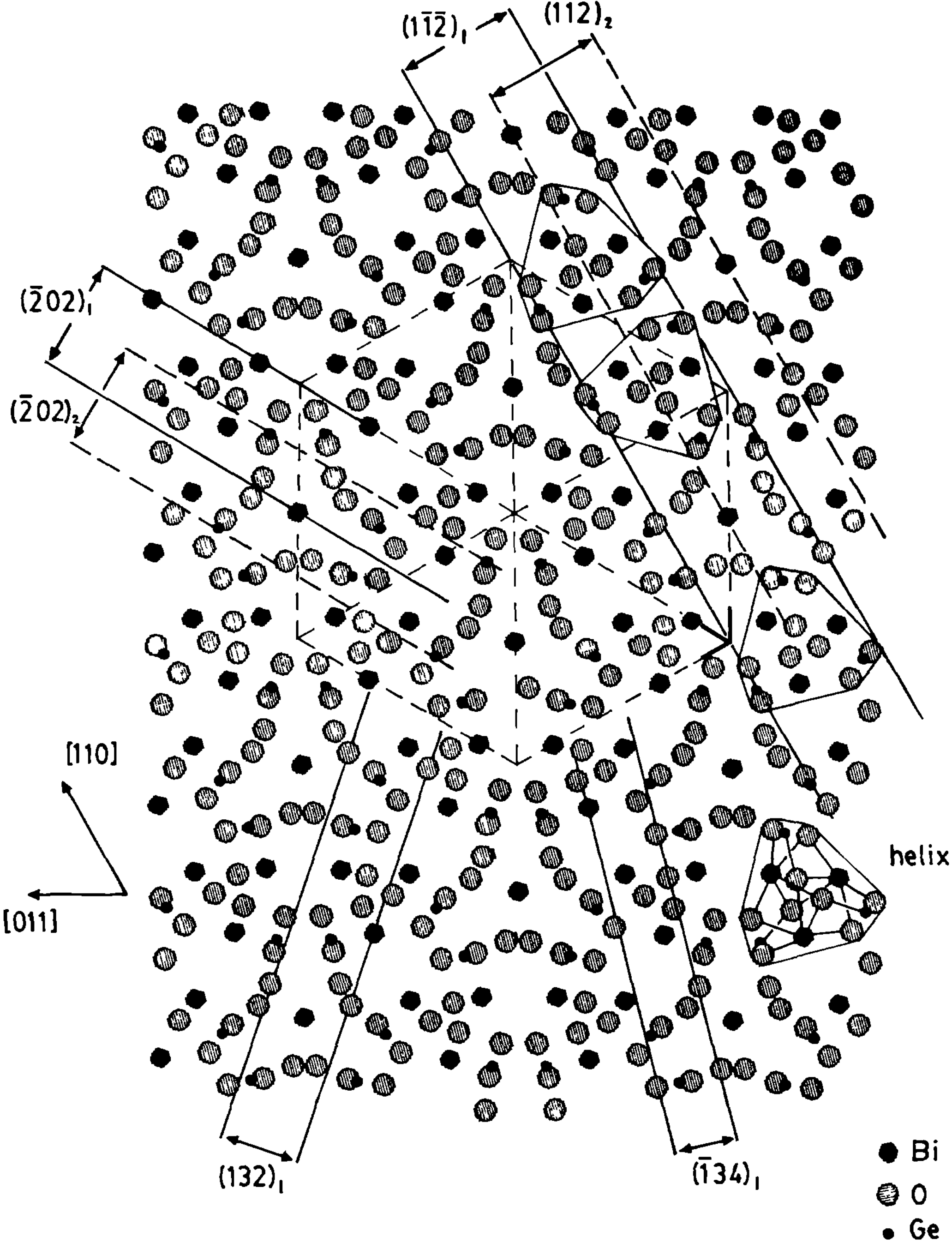
$(1\bar{1}\bar{2})_1$
$(1\bar{1}\bar{2})_2$
$(\bar{2}02)_1$
$(\bar{2}02)_2$
[110]
[011]
helix
$(132)_1$
$(\bar{1}34)_1$
Bi
O
Ge

Fig. 1b Projection along the $[\bar{1}1\bar{1}]$ direction. Note the polarity of the $(1\bar{1}\bar{2})1$ slice, indicating that the $(1\bar{1}\bar{2})$ crystal face will have more Ge-atoms and less Bi-atoms near its surface than the opposite $(\bar{1}12)$ face. See section 5.2 .

5.4 Calculation of the slice energy and the critical Ising temperature of the F-slices

The slice energy E_{slice} is defined as the energy content of a slice in reference to complete separation of the growth units, i.e. $\Sigma_{slice} \Phi^{ss}_i$. It was calculated by summing the bonds within a slice per stoichiometric unit and using the bond energies Φ_{Ge-O} ,Φ_{Bi1-O} and Φ_{Bi2-O} which were derived in section 4.1 . The slice energies of the eight F-slice are given in energy/mol in table 3.

The bond structure of BGO makes it possible to simplify the F slices by means of a statistical mechanical formalism [15,16]. This so-called star-triangle formalism replaces the set of three bonds between the O-atom and the Bi- and Ge-atoms by another set with equal partition function between the Ge- and Bi-atoms (fig 2). This yields an O-free bond structure from which the Ising nets can be obtained without ambiguity. The O-atoms belonging to stars which are cut by a slice boundary are statistically divided between the slices by this procedure.

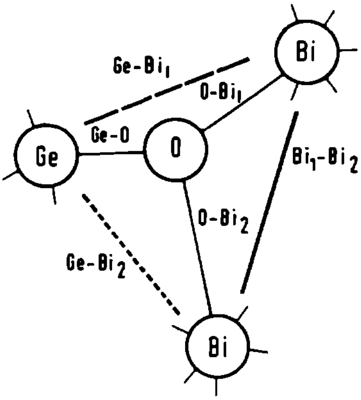

Fig. 2 Basic motif in the bond structure. Bonds before (Ge-O, Bi_1-O , Bi_2-O) and after (Ge-Bi_1 , Ge-Bi_2 , Bi_1-Bi_2) the star-triangle transformation are indicated. See section 4.1 .

By introducing additional bonds with zero strength and bonds with infinite strength at appropriate locations, the simplified F slices are subsequently transformed into rectangular Ising nets. In fig. 3a the simplified F slices are given, in fig. 3b the corresponding Ising nets. From these rectangular nets Ising temperatures can be calculated.

In the calculation of the Θ^c_{hkl} only relative values for the strength of the bonds that constitute the net are needed. It is sufficient to use the Φ^{ss} values of sec. 4.1 and the proportionality hypothesis eq. (2) in eq. (1) to obtain the interaction energies $\Phi_{Ge-O} : \Phi_{Bi1-O} : \Phi_{Bi2-O}$ of the original bondset. However the

3a

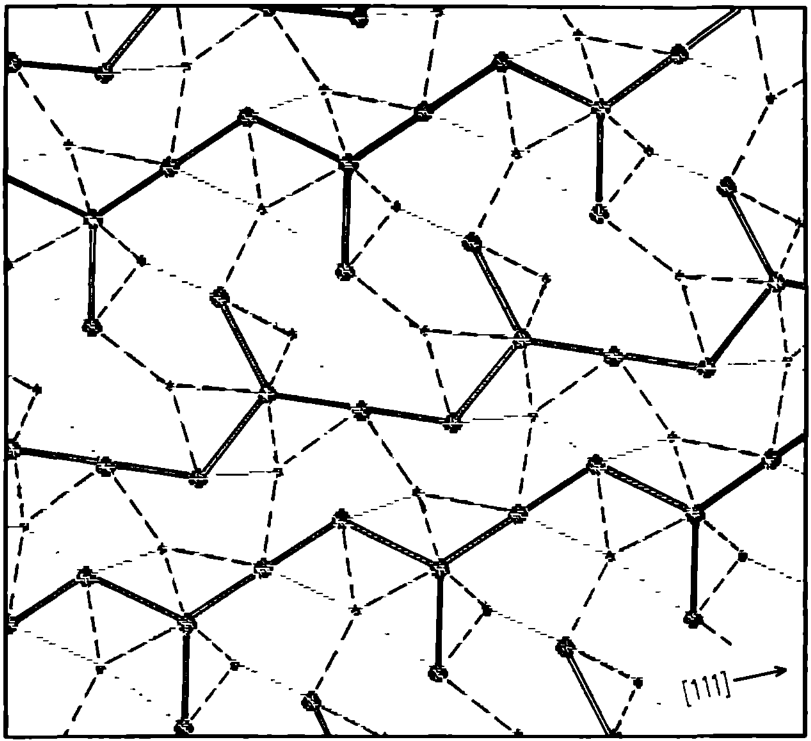

(112)₁

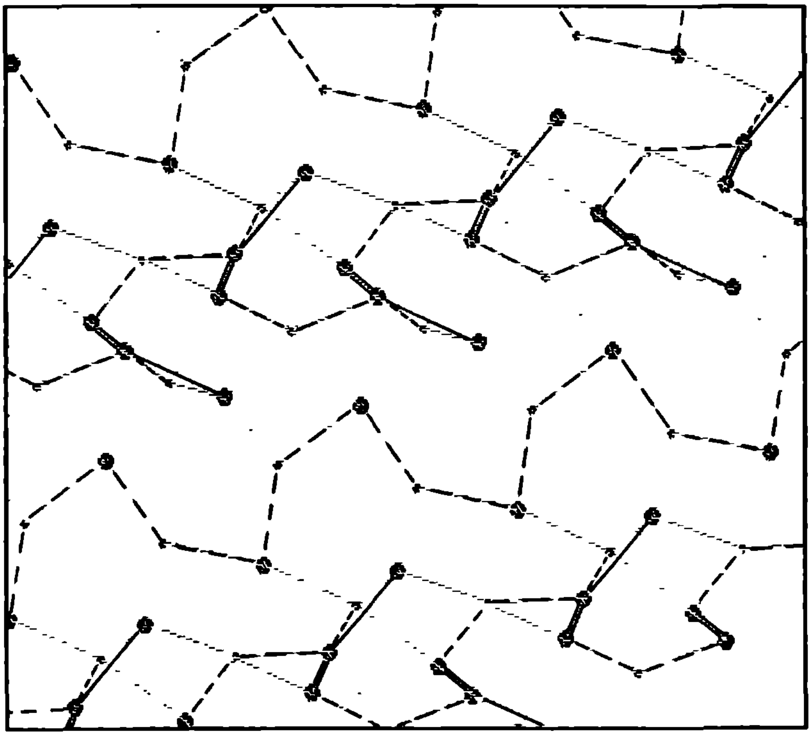

(112)₂

3a

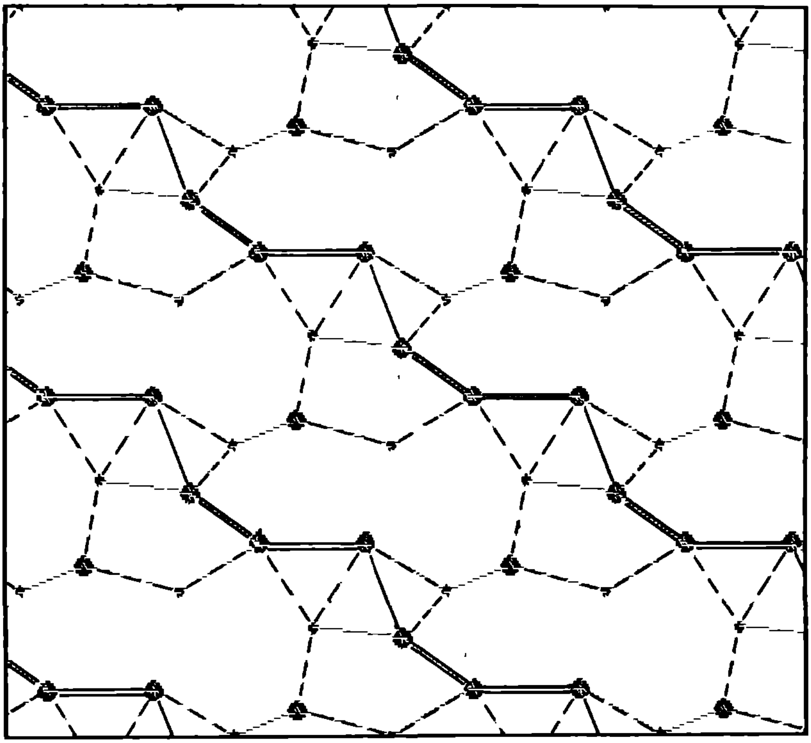

(220)₁

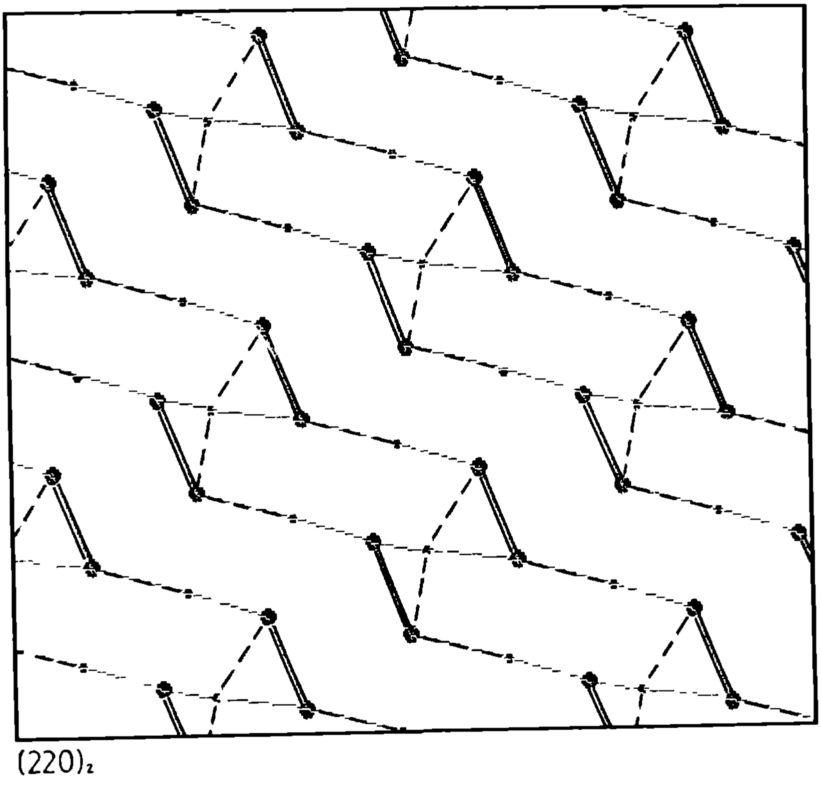

(220)₂

3a

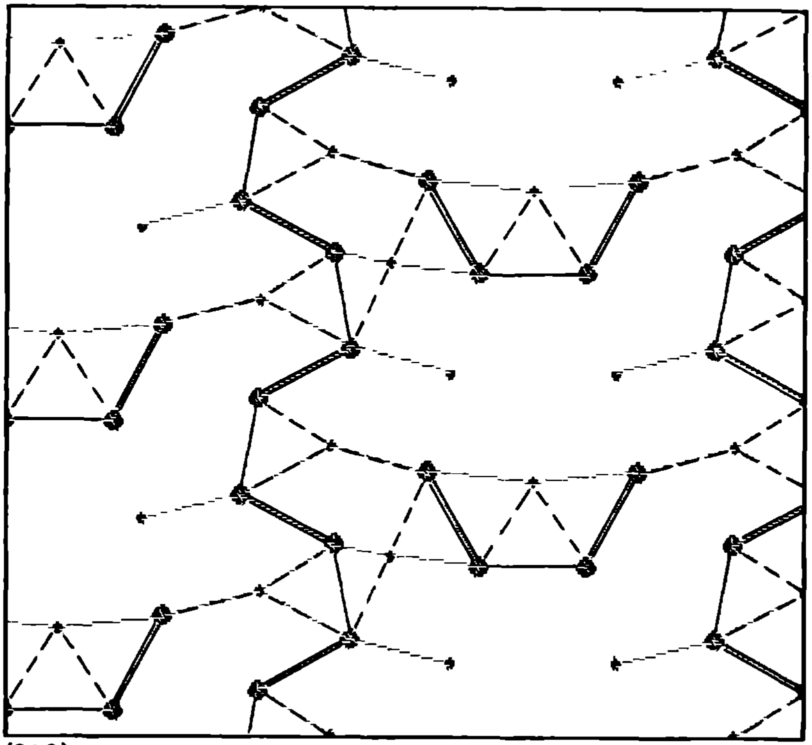

(310)₁

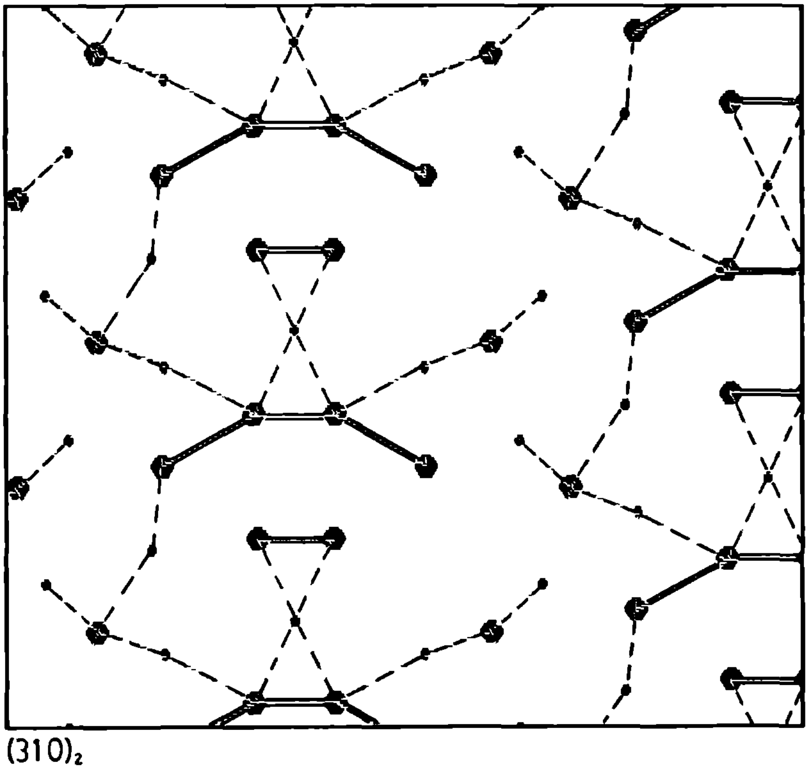

(310)₂

3a

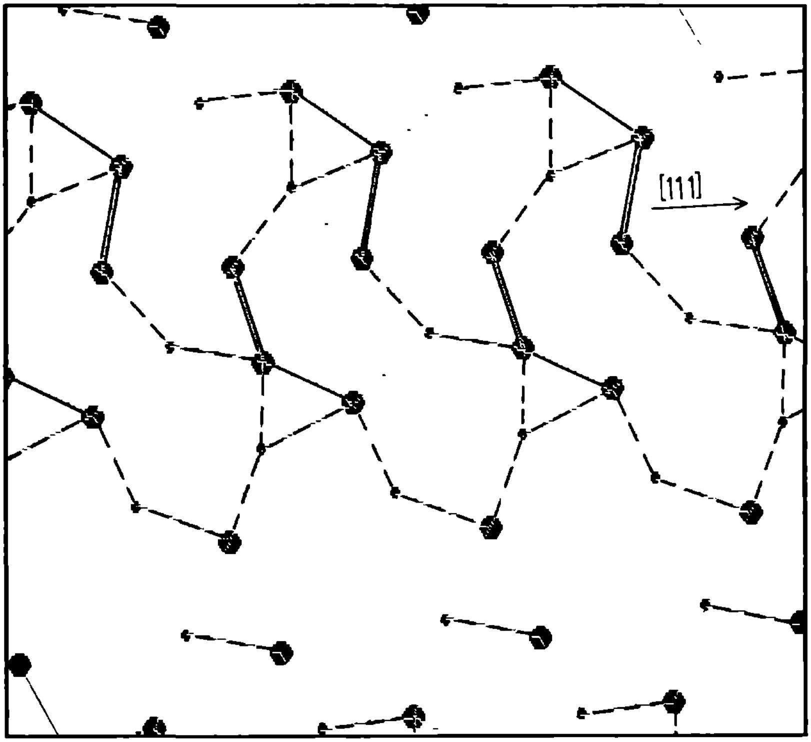

$(321)_1$

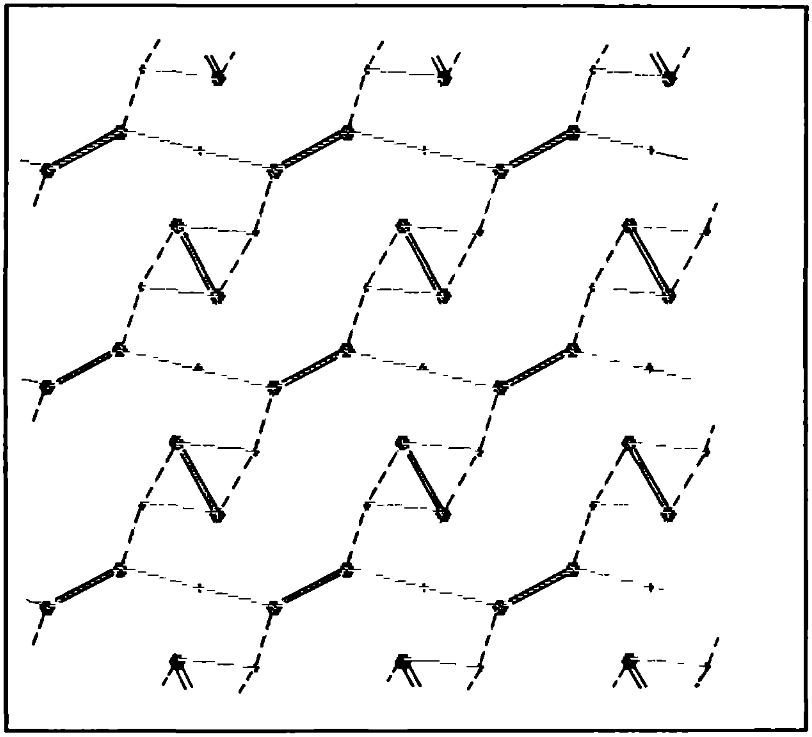

$(400)_1$

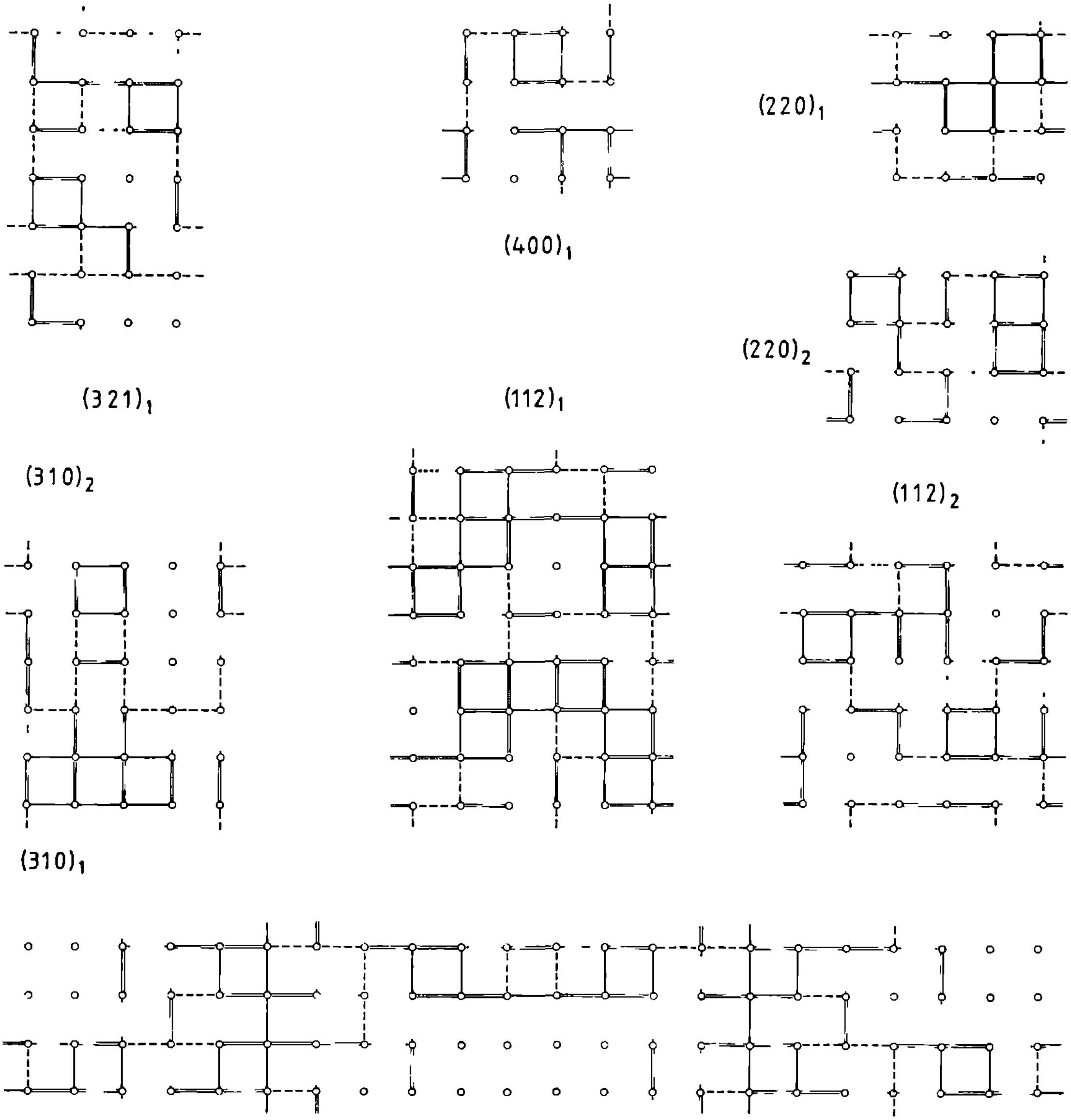

Fig. 3b Rectangular Ising nets belonging to the connected nets in figure 3a. Double lines represent infinitely strong bonds; other lines: see figure 3a.

Fig. 3a Projection of the simplified connected nets of the slices $(112)_1$, $(112)_2$, $(220)_1$, $(220)_2$, $(310)_1$, $(310)_2$, $(400)_1$ and $(321)_1$. Bond types: heavy lines represent Bi_1-Bi_2 (double lines are double bonds), dashed lines Ge-Bi_1, dotted lines Ge-Bi_2 (See also fig. 2).

$\Phi_{Ge-B11} : \Phi_{Ge-B12} : \Phi_{B11-B12}$ which result from the star-triangle transformation are rather dependent on the absolute values (i.e. Φ_{Ge-O}/RT , Φ_{B11-O}/RT , Φ_{B12-O}/RT) of the original bondset. Therefore the Θ^C_{hkl} were calculated (according to ref 3) over a wide range of these Φ_1/RT amply covering the variations due to the star-triangle transformation. This is illustrated in fig. 4 where the Θ^C_{hkl} are as usual expressed in terms of the strongest bond in the nets, (Φ_{Ge-B11} / RT $)^C_{hkl}$ .On the abcis the range of absolute values of the original bondset is given, in terms of Φ_{Ge-O} /RT. It is interesting that the Θ^C vary differently with this variation in bond proportions. The nearby lying {123} and {004} are seen to change order. The dashed line gives the variation of Φ_{Ge-B11} /RT with Φ_{Ge-O} /RT. At the intersections the exact Θ^C_{hkl} are found.

In the calculations of Θ^C only the values for the solid bonds Φ^{ss} were used. No assumptions had to be made about the solid-liquid interactions Φ^{sf} , i.e. the wetting conditions. These are discussed further in section 7. This does not mean that the Θ^C are totally independent of the motherphase. From the considerations in section 4.2 it is clear that the nature of the motherphase is decisive for

Slice (hkl)$_n$	ξ = E_{sl}/E_{cr}	$\frac{1-\xi}{\sqrt{h^2+k^2+l^2}}$	$\Sigma\Phi^{ss}_1$ = E_{slice} kcal/mol	Θ^c = $\left(\frac{RT}{\Phi_{Ge-B11}}\right)^c$	T^R range $T^c_{112}>T_m>T^c_{220}$ T^R	°K T^R
112_1	0.6100	0.159	1616	3.0	1329	1609
112_2	0.4681	0.217	1240	1.62	907	1098
310_1	0.4821	0.164	1277	1.91	1008	1220
310_2	0.3524	0.205	933	1.11	697	843
220_1	0.4547	0.193	1205	2.17	1097	1328
220_2	0.3903	0.216	1034	1.47	851	1029
400_1	0.3903	0.152	1034	1.44	837	1013
321_1	0.3780	0.166	1001	1.43	835	1011
420	N.C. a)					
444	N.C.					
511	N.C.					

a) not connected

Table 3 F-slices with their slice energy Eslice , critical Ising temperature Θ^c = (RT/ Φ^{Ge-B11} $)^c$, crystallographic factor ξ = Eslice / Ecrystal , attachment energy per surface unit, and temperature range for the roughening temperature T^R which was calculated in section 7.

the choice of the growth units and the validity of the proportionality hypothesis.

6. Predicted morphology of BGO and comparison with morphological literature data

In table 3 are given the F slices with their slice energy and critical Ising temperature, the crystallographic factor § = E_{slice} / $E_{crystal}$ (Jackson anisotropy factor) and the attachment energy per surface unit (1-§) / $\sqrt{{}^2h+{}^2k+l^2}$ which is a measure for the surface energy.

For the faces {112},{310} and {110} , pairs of connected nets occur. It can be seen that using E_{slice} and θ^c_{hkl} as criteria for the relative strength, the $(hkl)_1$ are the strongest of pairs. As usual we will assume in the following that these slices will be dominant.

Table 4 gives the Morphological Importance according to the criteria E_{slice} , θ^c , and the BFDH law, as well as a summation of the M.I. extracted from literature data of eulytine type crystals.

The predictions which follow from the different criteria are almost the same. The $(112)_1$ slice is clearly much stronger then all the other slices; this makes {112} the dominating crystal form. The second in morphological order predicted by θ^c, is {220}, followed by {130}. For these faces the E_{slice} criterion gives the reverse order

Crystal form	**Predicted M.I.**			**Morphological literature data**			
{hkl}	E_{slice}	θ^c	BFDH law	mineral. [29] BSO	hydroth. [30,31] BSO	BGO	sphere exp. [24] BGO
{112}	1	1	1	1		1,2	1
{110}	3	2	2	-	1	1,2	
{310}	2	3	3	4		3	
{100}	4	4	5	2		4	
{321}	5	5	4				
{111}	N.C		14	3			
{511}	N.C		low	5			

Table 4 The order in Morphological Importance predicted by the criteria Eslice ,θ^c and the BFDH law, together with the observed order according to morphological data.

although the distinction is not large here. {400} and {123} with order 4 resp. 5 have almost equal slice energy and Θ^c , so their sequence is not strict.

In order to compare the results of the theory, morphological data from various sources will now be presented. The only naturally occurring crystal with eulytine structure is $Bi_4Si_3O_{12}$ (BSO). The M.I. , obtained from a compilation of mineralogical literature by Goldschmidt (ref. 29) is given in column 5 of table 4. Russian workers (ref. 30,31) recently reported on hydrothermally grown BGO and BSO ; these data are in column 6 and 7. The last column refers to the results of sphere growth experiments on BGO, which we reported earlier [1].

In these experiments a single crystal sphere was immersed in the stoichiometric melt at a few degrees supercooling. After withdrawal from the melt, the slightly grown spheres should exhibit all F faces which are not roughened at this temperature. For these well defined growth circumstances the calculations were carried out. It was found that at 1328 °K only {112} and {112} faces developed. The other F faces were definitely roughened.

As can be seen from the table the predictions agree well with the data on BGO , and fairly well with the BSO data.

It is interesting that in the mineralogical data the {110} is rare, while for the hydrothermally grown BSO this is apparently the dominating growth form. Since the atomic coordinates of BSO differ only slightly from the BGO coordinates, it is expected that the present analysis is also applicable to BSO, provided that the growth units are the same. However, the Si-O bond in BSO is calculated 1.3 times stronger than the Ge-O bond in BGO. It seems well possible that in the hydrothermal solution the Si is present as SiO_4 complexes, which then become growth units. In fig. 1b it can be seen that in the strongest slice $(112)_1$ most of the Ge-atoms are situated near the slice boundaries. This means that in case of SiO_4 growth units, this slice will turn out much weaker. In the $(220)_1$ slice, which is second in morphological order (for BGO), this is not the case. This suggests that in hydrothermal growth of BSO the {220} indeed will have the highest M.I.

7. Wetting

In sect. 5.3 the Φ^{fs}_i were interrelated qualitatively by the proportionality hypothesis $\Phi^{ss}_i : \Phi^{fs}_i : \Phi^{ff}_i = \Phi^{ss}_j : \Phi^{fs}_j : \Phi^{ff}_j$. They can be specified further by relating them quantitatively to the Φ^{ff}_i . A classical assumption is the complete wetting condition, introduced implicitely by Jackson [32]. In this model the liquid-liquid bonds in the bulk are thought to extend fully up to the (sharp) solid-liquid interface, thereby wetting it completely, i.e. $\Phi^{fs}_i = \Phi^{ff}_i$. Inserting this condition in eq. (2) gives $\Phi_i/kT =$

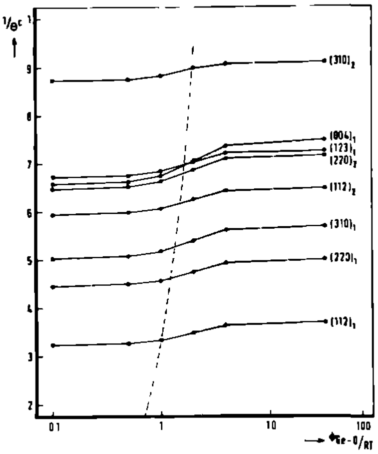

Fig. 4 Critical Ising temperatures Θ^c of the connected nets, for varying bond proportions which follow from the star-triangle transformation, in dependence of Φ^{Ge-O}/RT (see section 5.4).

$^1/_2(\Phi^{ff}_1 - \Phi^{ss}_1)$ /kT . The numerator is equivalent with the energy of crystallization, a measurable quantity. The Φ_1/kT are now fully determined and from the critical Ising temperatures Θ^c_{hkl} belonging to the crystal faces which were calculated in sect. 5.3 the T^c_{hkl} and thus the roughening temperatures T^R_{hkl} are obtained .

In the present case, the growth of BGO from its stoichiometric melt at 1328 °K, the energy of crystallization amounts to 44.6 kcal/mol [33], which gives T^R_{112} = 370 °K for the most persistent face.

From the sphere growth experiments however it is clear that at the melt temperature this crystal face is not roughened up. This means that the calculated T^R are much too low. The discrepancy is a familiar one though. In several cases, where the roughening temperature (calculated with complete wetting) could be compared with experimental data it is found that although the morphological order of the faces is essentially correct, the T^R are low by a factor of at least 3 [34,35].

Groot et al. have tackled this problem on a fundamental level [12,36]. In their work on liquid theory, involving computer simulations of a hard sphere liquid against a hard wall, typically a diminished density is found along the wall compared with the bulk of the liquid. This strongly suggests that in a general case one has to assume incomplete wetting.

Within the Ising model this means that $|\Phi^{sf}| < |\Phi^{ff}|$. In our case it is possible by assuming $\Phi^{sf}_1 = x . \Phi^{ff}_1$ ($0<x<1$) to fit the degree of wetting to the results of the sphere growth experiments. In fig. 4 it can be seen , since the {220} faces are roughened and the {112} are not, that the melt temperature must lie between Θ^c of {220} and Θ^c of {112} on the vertical axis. Thus, using :

$$(\Phi_{Ge-Bi1}/RT_{220})^c < (\Phi_{Ge-Bi1}/RT_{melt})^c < (\Phi_{Ge-Bi1}/RT_{112})^c \qquad (6)$$

a range can be calculated for the T^R of each of the F slices. These are collected in table 3. The fitting parameter x is found to vary 0.976 < x < 0.971 , and can be interpreted as the degree of wetting.

8. Conclusions

The PBC theory of Hartman and Perdok, extended with the two dimensional Ising interface model was applied to BGO, growing from the melt.

Five F-faces were found and their M.I. was calculated, using the critical Ising temperature as a criterion.

The predicted growth form comprises the following faces, in order of their M.I. : {112},{110},{310},{100} and {123}. This prediction is in good agreement with the morphological literature data on BGO and other eulytine type crystals.

Combining the morphological calculations with the results of accurate sphere growth experiments, the solid-liquid interaction could be estimated.

For growth from the pure melt a value $\Phi^{fs}/\Phi^{ff} = 0.973$ is found, which is consistent with recent developments in liquid theory.

For the absolute roughening temperatures of the faces, occurring on the growth form, temperature ranges were calculated.

Acknowledgements

The authors are indebted to Prof. Dr. R.T. van de Walle for his interest in the present work. One of us (F.S.) whishes to acknowledge the financial support by the Foundation for Technical Sciences (STW).

REFERENCES

[1] F. Smet and W.J.P. van Enckevort, J. Crystal Growth 88 (1988) 169.

[2] P. Hartman in: Crystal Growth, An Introduction (North Holland, Amsterdam, 1973) p. 367.

[3] J.J.M. Rijpkema, H.J.F. Knops, P. Bennema and J.P. van der Eerden, J. Crystal Growth 61 (1983) 295.

[4] P. Bennema and J.P. van der Eerden in: Morphology of Crystals, Ed. I. Sunagawa, Vol A (Reidel, Dordrecht, 1988).

[5] P. Hartman and P. Bennema, J. Crystal Growth 49 (1980) 145.

[6] R.A. Terpstra and P. Bennema, J. Crystal Growth 82 (1987) 416.

[7] P. Hartman, J. Crystal Growth 49 (1980) 157.

[8] R.A. Terpstra, P. Bennema, P. Hartman, C.F. Woensdregt, W.G. Perdok and M.L. Senechal, J. Crystal Growth 78 (1986) 468.

[9] see for instance: J.P. van der Eerden, P.Bennema and T.A.Cherepanova, Prog. Crystal Growth Characterization 1 (1978) 219.

[10] P. Bennema, E.A. Giess and J.E. Weidenborner, J. Crystal Growth 62 (1983) 41.

[11] L.A.M.J. Jetten, H.J. Human, P. Bennema and J.P van der Eerden, J. Crystal Growth 68 (1984) 503.

[12] R.D. Groot, Thesis, University of Nijmegen, Nijmegen (1988).

[13] G. Menzer, Zeit. Krist. 78 (1931) 136.

[14] A. Durif et M.T. Averbuch-Pouchot, Compt. Rend. (Paris) 295 (1982) 555.

[15] J.P. van der Eerden and P. Bennema, J. Crystal Growth 61 (1983) 45.

[16] R. Houtappel, Physica 16 (1950) 425.

[17] L. Pauling, The Nature of the Chemical Bond (Cornell, New York, 1960) p. 99.

[18] C.A. Morrison and R.P. Leavitt, J. Chem. Phys. 74 (1981) 25.

[19] R. Sanderson, Chemical Bonds and Bond Energy (Academic Press, New York, 1971).

[20] K. Nassau and D.L. Chadwick, J. Am. Cer. Soc. 66 (1983) 332.

[21] E.F. Riebling, J. Mater. Sc. 9 (1974) 759.

[22] K. Nassau and D.L. Chadwick, J. Am. Cer. Soc. 65 (1982) 199.

[23] V.P. Zhereb, Y.F. Kargin and V.M. Skorikov, Izv. Akad. Nauk SSSR, Neorg. Mater. 14 (1978) 1580.

[24] W.J.P. van Enckevort and F. Smet, J. Crystal Growth 82 (1987) 678.

[25] J.C. Brice, J.M. Robertson and H. van der Heide, J. Crystal Growth 30 (1975) 375.

[26] J.M. Robertson and J.C. Brice, J. Crystal Growth 31 (1975) 374.

[27] J.D.H. Donnay and D. Harker, Amer. Miner. 22 (1937) 446.

[28] International Tables for X-ray Crystallography, Eds. N.F.M. Henry and K. Londsdale (Kynoch, Birmingham, 1976).

[29] V. Goldschmidt, Atlas der Kristallformen, Bd 3 (Carl Winters Universitätsbuchhandlung, Heidelberg, 1916).

[30] A.F. Firsov et al., Inorg. Mater. 21 (1985) 378.

[31] V.S. Surnina and B.N. Litvin, Izv. Akad. Nauk SSSR, Neorg. Mater. 6 (1970) 1695.

[32 K.A. Jackson in: Liquid Metals and Solidification (American Society for Metals, Cleveland 1958).

[33] E. Lorenz, Recent Progress in Development for High Resolution Calorimetry (Max Planck Institute Report MPI-PAE/Exp. EL 129, 1984).

[34] Tsutumo Sawada, J. Crystal Growth 60 (1982) 350.

[35] P. Bennema in: Industrial Crystallization 84, Eds. S.J. Jančić and E.J. de Jong (Elsevier, Amsterdam, 1984) p.340.

[36] R.D. Groot, M. Elwenspoek and P. Bennema, J. Crystal Growth 79 (1988) 817.

SAMENVATTING

Dit proefschrift beschrijft een onderzoek naar de kristalgroei van Bismuth Germanaat ($Bi_4Ge_3O_{12}$, BGO). In hoofdzaak is aandacht geschonken aan het groeiproces uit de smelt bij 1055 °C. Centraal stonden de groei en eigenschappen van grote eenkristallen met het oog op hun toepassing als scintillatie medium. Voor deze toepassing zijn zeer perfecte, optisch transparante kristallen vereist.

Het voornaamste doel van het onderzoek was het verkrijgen van een dieper inzicht in de fundamentele kristalgroeiprocessen bij BGO. Deze kennis is onontbeerlijk voor de bepaling en optimalisatie van de belangrijke groeiparameters in de Bridgman en de Czochralski groeimethoden.

Hiertoe werden gerichte studies uitgevoerd op het gebied van het fundamentele groeigedrag van BGO, de specifieke groeiomstandigheden in Bridgman ovens en de karakterisatie van grote BGO kristallen. Een aantal belangrijke resultaten worden in de hierna volgende hoofdstukken besproken.

De bestudering van de groei bij hoge temperatuur in een zeer corrosieve smelt was mogelijk door de ontwikkeling van een speciale waarnemingsmethode, de hoge temperatuur in-situ microscopie. Hoofdstuk 2 beschrijft de direkte observatie van nucleatie en groeigedrag van BGO met behulp van deze elegante methode. Ook worden hier de resultaten besproken van een systematisch onderzoek naar groeiverschijnselen in het hele fasediagram GeO_2-Bi_2O_3.

In hoofdstuk 3 wordt de groei van grote BGO kristallen besproken. Met behulp van een aantal morfologische experimenten (waaronder bolproeven) en gebruikmaking van U.V. topografie, laserscattering en de Schlierenmethode als karakterisatiemethoden kon onder meer worden vastgesteld dat in Bridgman groeicondities het vloeistof-vast grensvlak gevormd wordt door $\{112\}$ en $\{\bar{1}\bar{1}\bar{2}\}$ kristallografische facetten. Aangetoond werd dat er een verschil in optische dichtheid en in impuritiesegregatie bestaat tussen langs $\{112\}$ en $\{\bar{1}\bar{1}\bar{2}\}$ gegroeide kristalsectoren. In dit hoofdstuk worden ook de resultaten besproken van een vergelijkende karakterisatie studie aan met de Bridgman methode en met de Czochralski methode gegroeide kristallen.

Hoofdstuk 4 omvat een gedetailleerde studie van de meest gevoelige microscopische technieken, en hun toepasbaarheid voor de karakterisatie van BGO. Met spanningsdubbelbrekingmicroscopie kon de Burgers vektor van de dislocaties in Bridgman gegroeide kristallen worden geidentificeerd als 1.[110]. Met donkerveld-microscopie werden aan dislokaties gerelateerde, tijdens de groei gevormde, micro-inclusies gevonden. In een aanvullende studie is de microscopische detecteerbaarheid van dislokatie-etsputten op verruwde kristalvlakken geanalyseerd.

Hoofdstuk 5 is gewijd aan de kristalmorfologie van BGO. De PBC theorie van Hartman en Perdok, en het Rijpkema-formalisme werden toegepast op de kristalstructuur van BGO. Uitgaande van een zorgvuldige analyse van de bindingen in het kristal en in de smelt, is de morfologische belangrijkheid (M.I.) van de kristallografische vlakken, en hun kritische Ising temperatuur berekend. De resultaten werden vergeleken met de experimenteel bepaalde kristalmorfologie van BGO. Hieruit kon de absolute verruwingstemperatuur van de voornaamste kristalvlakken voorspeld worden.

De schrijver van dit proefschrift werd geboren op 1 augustus 1950 te Vlissingen. Zijn middelbare schoolopleiding volgde hij aan het Jansenius Lyceum te Hulst, alwaar in 1967 het eindexamen HBS-B werd afgelegd. De militaire dienstplicht werd vervuld van 1972 tot 1974. In 1974 werd de studie scheikundige technologie opgevat aan de Technische Hogeschool Eindhoven. In 1983 werd het ingenieursdiploma behaald bij de vakgroep fysische chemie met als onderwerp: "Diffusie en fasenrelaties in de systemen Mo-Si-C en W-Si-C bij 1200 °C".

Van 1984 tot 1988 was hij als wetenschappelijk medewerker in dienst van de Stichting voor de Technische Wetenschappen en werkzaam op de afdeling experimentele hoge energie fysica en de afdeling vaste stof chemie van de Katholieke Universiteit Nijmegen. In deze periode vond het in dit proefschrift beschreven onderzoek plaats.

STELLINGEN

I

De door Kitamura et al. geopperde suggestie dat de congruente samenstelling van gallium-gadolinium-granaat tijdens Czochralski groei afhangt van de groeisnelheid berust op een onjuiste toepassing van het BPS model.

- K. Kitamura, Y. Miyazawa, Y. Mori, S. Kimura and M. Higuchi, J. Crystal Growth 64 (1983) p.214.
- J.A. Burton, R.C. Prim and W.P. Slichter, J. Chem. Phys. 21 (1953) 1987.

II

De bij sommige kristalgroeiers ingeburgerde uitdrukking 'kristallen trekken' voor het doen groeien van grote eenkristallen volgens de Bridgman methode, duidt op de aanwezigheid van ongeduld bij de groeiers.

III

In het basisonderwijs wordt het belang van de gelijktijdig met de kennisoverdracht plaatsvindende persoonlijkheidsontwikkeling van het kind onvoldoende onderkend.

- W.J. Bladergroen, in: Lichamelijke en geestelijke ontwikkeling van het kind, (Wetenschappelijke Uitgeverij B.V., Amsterdam, 1976), hoofdstuk 4.

IV

Natuurwetenschappelijk gezien is de aard van het gedachtenwisselingsproces tussen mensen nog grotendeels onbegrepen.

V

De door de overheid gehanteerde veiligheidsnormen op het gebied van de volksgezondheid staan in geen verhouding tot het risico dat de gemiddelde burger iedere dag weer in het verkeer wenst te nemen.

- *Statistisch zakboek 1988 (Staatsuitgeverij,'s Gravenhage, 1988), pag. 255.*
- *Brabants Dagblad, juli 1988.*

VI

De omzetting van de laatste tropische regenwouden in nationale parken van beperkte omvang, en daarmee het verlies van een belangrijk deel van 's werelds biologische erfenis, is slechts met machtsmiddelen te voorkomen.

VII

Voor het verkrijgen van een realistisch beeld bij discussies over millieuproblematiek verdient het aanbeveling om de toenemende bevolkingsdichtheid als belangrijkste oorzaak te vermelden.

VIII

De karakterisatie van een perfect kristal is zowel onmogelijk als overbodig.

IX

Inzicht is de boeggolf van kennis.

Frank Smet, 24 juli 1989